

DEVELOPMENT OF THE WIRELINE-LOG DATABASE AND DETERMINATION OF
POROSITY USING WIRELINE LOGS

Jeffrey A. Kane and James W. Jennings, Jr.

Bureau of Economic Geology
Scott W. Tinker, Director
John A. and Katherine G. Jackson School of Geosciences
The University of Texas at Austin
Austin, Texas 78713-8924

ABSTRACT.....	167
INTRODUCTION	167
OVERVIEW OF WIRELINE-LOG DATABASE.....	168
DATABASE ASSEMBLY PROCEDURES.....	170
QUALITY CONTROL.....	170
POROSITY-LOG NORMALIZATION.....	172
MOVING AVERAGE COMPUTATION.....	175
CORE CALIBRATION.....	175
CONCLUSIONS.....	177
REFERENCE.....	178

Figures

1. Map showing 316 wells with Sidewall neutron logs (SNP) used to calculate porosity for Fullerton Clear Fork field.....	179
2. Map showing 437 wells with compensated neutron logs (NPHI) used to calculate porosity for Fullerton Clear Fork field.....	180
3. Map showing all 733 wells used in porosity calculation for Fullerton Clear Fork field	181
4. An example of the Gaussian weighting function using various scale factors.....	182
5. Examples of average SNP porosity areally averaged with different scale factors	183
6. Plot of layer averaged core porosity (y-axis) as a function of layer averaged normalized compensated neutron porosity (x-axis) showing the calibration line for dolomites.....	184
7. Plot of layer averaged core porosity (y-axis) as a function of layer averaged normalized sidewall neutron porosity (x-axis) showing the calibration line for dolomites	185
8. Plot of core porosity (y-axis) as a function of normalized compensated neutron porosity (x-axis) showing the calibration line for limestone	186
9. Plot of core porosity (y-axis) as a function of normalized sidewall neutron porosity (x-axis) showing the calibration line for limestone	187

Development of the Wireline-Log Database and Determination of Porosity Using Wireline Logs

Jeffrey A. Kane and James W. Jennings, Jr.

ABSTRACT

This paper reviews development of the wireline-log database used in the Fullerton Clear Fork field reservoir characterization project. A review of the field's logging history is followed by a discussion that covers the assembling and quality checking of the log data and normalization of neutron-porosity logs, along with their subsequent calibration to core porosity. This study deviated slightly from the norm in that assembly of the database and quality control of data were concurrent with interpretation of the data. Because of the nature of the reservoir, traditional log normalization methods were not adequate. A method of normalization is described herein that is a modification of traditional methods, which overcomes these problems.

INTRODUCTION

This report describes procedures used to assemble, quality check, and interpret wireline logs from Fullerton Clear Fork field, which is located in northwestern Andrews County, Texas. The field is dominantly dolomite with an average core porosity of slightly more than 6 percent and a maximum core porosity of about 33 percent. Discovered in the 1940's, the field has logs that span 6 decades of technology.

Assembling and quality checking the log data were complicated as new and redigitized log data were received throughout the study period. The constant influx of data throughout the project required specialized updating processes to keep the database current. With such a large field, data normalization became an issue. Several common normalization methods were tried

but found to be inadequate. The final normalization method employed is different from traditional methods in that the mean and standard deviation of the data at each well are estimated from other wells nearby using a weighted moving average. The logs being normalized are then shifted to these new local values. Finally, the normalized data are calibrated to available core-porosity information. Only porosity was calculated in this study. Because of the long life of the field, modern log data used were not representative of original field-water saturations. Correlations of porosity to water saturation were therefore used to estimate original saturation conditions. These correlations are discussed elsewhere (Jones and Lucia, this report).

OVERVIEW OF WIRELINE-LOG DATABASE

Fullerton Clear Fork field contains log suites that span logging history. Because the field was discovered in the mid-1940's, earliest log suites are the electric logs common to that period. And because the field has had several periods of development throughout its history, log suites range from these original electric logs to modern suites available today. This long time span created numerous difficulties for log quality control and analysis.

Log suites in Fullerton Clear Fork field can be divided into four general groupings. The first grouping is composed of those logs associated with initial field development in the mid- to late 1940's and includes early electric logs. The second grouping differs from the first group by the addition of a gamma-ray neutron log to the early electric log suite and is characteristic of the 1950's. The third grouping consists essentially of a sidewall neutron log and a modern resistivity log, either a dual laterolog or a dual induction. This log suite was common throughout the 1960's and was the first suite to contain a log calibrated in porosity units. During the 1970's the use of the compensated neutron log was introduced, commonly without resistivity logs. Use of this suite has continued through the present.

The oldest electric logs (or e-logs) commonly comprised three tools, a long lateral of varying spacing length; a short normal, again of varying spacing; and a limestone lateral curve. The long laterals had spacings of 13, 18, and 24 ft generally; however, some other lengths occasionally used. The short normal typically had 10-inch spacing; however, 12-, 16-, and 18-inch spacings were also used. Limestone laterals were essentially all 32-inch laterals, along with a few 34-inch laterals. For the most part, these log suites were not used for evaluation in the field, except in some specialized circumstances, in which attempts to evaluate original-oil-saturation profiles were made.

The second group, which includes those wells that contain some form of gamma-ray neutron log, comprises wells that were logged through the 1950's to early 1960's. Unfortunately, these logs vary considerably in tool design, measurement type, and overall quality. Numerous problems properly defining the logging environment and a lack of core information for calibrating these data to porosity precluded using this group of wells in field analysis.

The third group of wells, as stated earlier, comprises sidewall neutron logs (SNP), typically run with a dual laterolog. This is the oldest suite of logs with calibrated porosity curves and core sufficient to provide a calibration to core-measured porosities. This set of data comprises 320 wells, 316 of which have data acceptable for normalization. Locations of these 316 well are displayed in figure 1. The actual process of porosity normalization will be discussed in a subsequent section.

The fourth group is essentially all modern-day logs. The dominant porosity log in this group is the compensated neutron log (CNL). The dataset is made up of 471 wells, 437 of which were of sufficient quality to use for normalization (figure 2).

Twenty wells are common to groups three and four. Because of this overlap the total number of wells used for the quantitative part of the full field study is 733, not 753. Locations of these wells are shown in figure 3. As can be seen from this figure, well coverage is good over most of the field; however, the west edge and some of the south part lacks coverage sufficient for detailed characterization.

DATABASE ASSEMBLY PROCEDURES

The software chosen to build and maintain the log database was Geolog, which is marketed by Paradigm Geophysical Software. This software has two advantages for a project this size. It can handle large numbers of wells in its database, and, more important, it can process large numbers of wells in batches relatively quickly. The ability to run a batch efficiently greatly facilitated keeping the log database current. It also has a robust programming language, allowing user-defined extensions of almost any complexity.

QUALITY CONTROL

The initial database included approximately 1,150 wells. Because of concerns over quality of the original database, the operator, ExxonMobil began a complete redigitization of all logs in the field soon after the reservoir characterization project began. Ultimately 1,206 wells were redigitized. The digitization contractor, IHS Energy, provided all initial quality control (QC) with respect to the actual digitization project. Data were then sent to ExxonMobil, and ExxonMobil forwarded the data to the Bureau of Economic Geology (BEG) for inclusion in the characterization project. During the initial phase of the project, detailed quality control was performed on approximately 275 wells after these data were received from ExxonMobil. The wells included examples from all log-suite types. This level of quality control allowed team

members to provide feedback to the digitizing company and ExxonMobil to resolve some issues early on that may have caused significant problems later. During the remainder of the project, all well data received were reviewed prior to loading for completeness of digitization, and detailed QC was performed randomly.

For quality control of digitized log data to be properly maintained, copies of original paper logs are critical. Visual verification of the quality of digitization, verification of proper log-header transcription, and review of paper logs for well-bore-environment specifics affecting proper log analysis can be done only with access to copies of original paper logs. A well-bore environment issue can serve as an example. After review of numerous gamma-ray neutron logs, it was noted that at least half were run during well-deepening events, meaning that logs had both open-hole and cased-hole components. These logs needed to be broken into open-hole and cased-hole sections and normalized independently. This situation would not have been recognized, however, without copies of the paper logs available for review. Further investigation showed that a lack of core data associated with these wells and a broad spectrum of gamma-ray neutron tool types that were run in this group made normalization of these data unfeasible for this project.

Well logs for a given well in an update could have several files associated with it, and each of these files would contain log data at different levels of correction. Not all log types were included in the correction process nor in all levels of the correction process, so the loading of all files was necessary to capture all the data. Because of differences in data quality by file, the data had to be loaded in a specific order to ensure that the most recent, most completely edited curve was primary. For a few wells this process could be done interactively, but the large number of wells in this project made interactive loading unrealistic, requiring that an automated or semiautomated process be developed instead. Each file was ordered on the basis of level of

correction and date received. Once this ordering was done, all data were copied into a file from oldest, unedited data, to oldest edited data, to most recent unedited data, and finally to most recent edited data. At the conclusion of this process, a single file existed that contained all log data for a given well in a single table. The process culminated in 17,200 logs in the final update. Each time new data were acquired, the entire database was completely rebuilt to guarantee a complete dataset.

Each time the database was rebuilt, available log curves were reviewed. The digitization provider was often inconsistent in the naming conventions used, so curve mnemonics referring to the same data type varied throughout the digitization process. A total of 525 different log mnemonics were found in this review at the end of the project. Rectifying the differences was beyond the scope of this project and was performed only on an as-needed basis.

POROSITY-LOG NORMALIZATION

The first step in determining basic petrophysical parameters in this study was normalization of usable data. For this study, because a primary goal was accurate assessment of porosity, the normalization process focused exclusively on porosity logs, specifically compensated neutron logs (CNL) and sidewall neutron logs (SNP). Two different normalization methods were employed. A traditional normalization method was used in the early stages in a small area of the field selected for detailed study, modeling, and simulation. In later, full-field studies, this method of normalization was not adequate without modification.

Traditional normalization methods fall into two general categories. The first category of normalization methods requires stratigraphic intervals of constant properties over the area to be considered. For instance, in normalizing a porosity log, a low-porosity interval, such as an anhydrite, and a high porosity interval, such as shale, would be determined in each well, and

values of each log (CNL, SNP) for these intervals would be averaged for the area of interest. Each well log would then be shifted so that its average value across those intervals would be the same as the global average for that log in the respective stratigraphic interval. Fullerton field has no such intervals that can be used, however, making this approach inappropriate.

The second category of normalization methods commonly employed requires assumption that a distribution of some statistical parameter(s), i.e., minimum and maximum values, or the average and standard deviation of the porosity, is constant over some thick interval. The assumption of constant average and standard deviation of porosity was used in the initial study area. The approach was reasonable given the small (approximately two square mile) size of the initial study area. When this approach was applied to the full-field normalization of the neutron-porosity logs, it was found that these parameters are not constant across the entire field (approximately 45 square miles), so a variation of this method was employed.

The method in cases with areally varying statistics follows the work of Jennings and others (2002). First CNL or SNP porosity values were vertically averaged separately over genetic intervals. In Fullerton, stratigraphic cycles were the genetic intervals used. Using a number of intervals, a vertical average CNL or SNP porosity value is determined for all cycles under consideration by well. The vertical standard deviations of these cycle averages were also computed by well. In the Fullerton study, 19 such cycles were used, including cycles for the Lower Clear Fork to upper Wichita interval.

This computation by genetic intervals minimizes random errors such as measurement noise while preserving geologically relevant information. This phase of the process does not correct for systematic errors such as those generated by incorrect calibration of the logging tool. Such systematic errors are uniform over a single log at a single well location. As such, the error

will be reflected in the mean and standard deviation computed for a given well. Combining the means and standard deviations over a number of wells as would be done in computing a moving average, suppresses the systematic error associated with a single well.

Areally averaging the vertically averaged porosities and standard deviations of the averaged porosities over a subset area will provide a way of estimating a slowly laterally varying average and standard deviation of the CNL or SNP porosity. This use of a moving average can be thought of as a low-pass filter removing high-frequency local variability to enhance larger scale trends. The values of mean and standard deviation predicted via this method are now taken to be correct values at the well. To correct the neutron-porosity log curve to this new value for mean and standard deviation, each data value (CNL or SNP) is adjusted with this equation

$$\Phi_{corr} = (\Phi_{orig} - \mu_{orig}) \frac{\sigma_{pred}}{\sigma_{orig}} + \mu_{pred}$$

where Φ_{corr} is the corrected or normalized CNL or SNP data value, σ_{pred} is the new or predicted standard deviation, σ_{orig} is the standard deviation calculated from the original log data, Φ_{orig} is the original CNL or SNP data value, μ_{pred} is the new or predicted mean, and μ_{orig} is the mean calculated from the original data.

CNL and SNP logs were handled separately because their lithology response in dolomite is substantially different. Typically, CNL and SNP logs are run according to the assumption that the matrix being logged is limestone. If the actual matrix is not limestone then the calculated porosity will be in error. For SNP logs, this porosity difference is about 2 porosity units too high in dolomite. CNL variations in dolomite are not constant; however, in the porosity range encountered in Fullerton reservoir rock the difference is about 6 porosity units too high for dolomite. Because of this difference in dolomite response, the two different tools were handled separately and combined into a single dataset after calibration to available core porosity.

MOVING-AVERAGE COMPUTATION

Many different weighting functions can be used to compute a moving average. For this study, a Gaussian weighting function was used:

$$w_i = e^{-\left(\left(\frac{x-x_i}{s}\right)^2 + \left(\frac{y-y_i}{s}\right)^2\right)}$$

where w_i is the weight computed at the location x_i, y_i , x and y are the x and y locations of the well and s is the scale factor.

This function decays toward zero as the distance increases from the point where estimation is occurring but never goes to zero. In other words, all data are always used, although the weight of each point decreases with increasing distance from the estimation point (figure 4). The fundamental parameter controlling the Gaussian weighting function is the scale factor, which influences the decay rate of the weighting value computed by the Gaussian function with respect to distance. An optimal scale factor would suppress local variation without unduly suppressing the larger scale variations. In Fullerton field this parameter is chosen by inspection. A number of maps were made with varying scale factors (figure 5). After inspection a scale factor of 3,000 ft was used because visually it suppressed local variations in porosity without over-smoothing.

CORE CALIBRATION

Once data are normalized, they must be corrected to represent porosity, commonly done by calibration to available whole-core data. All available core data were used in this calibration process. For each curve used, two different calibration lines were derived, one for dolomite and one for limestone. Plots showing calibration lines for both compensated neutron logs and sidewall neutron logs are provided in figures 6 through 9.

The method used to determine calibration lines differed slightly between limestone and dolomite. Because dolomite is most prevalent throughout the reservoir interval, the approach for generating dolomite calibration lines was consistent with the averaging scheme used to determine normalization estimators. That is, core data were averaged over the same stratigraphic cycles as those for normalized neutron-porosity logs. The goal was to eliminate, as much as possible, the difference in vertical resolution between the two measurements. In addition, vertical averaging reduces random noise associated with the measurements.

The limestone calibration had to be handled somewhat differently. Because limestones are not as pervasive as the dolomites in this reservoir, the aforementioned method would not work. The averaging used to generate dolomite porosity calibrations suppresses the limestone response of the logs because of the relative percentage of limestone being much less than that of dolomite in this reservoir. Limestone calibration was therefore computed by comparing neutron porosity data with core data in the limestone intervals. Which data points corresponded to limestone was determined by selective filtering of the photoelectric factor (PEF) curve. Because calcite has a PEF value of five and dolomite has a PEF value of three, if a limit of accepting only a PEF value greater than four is set, limestones would be the prevalent lithology used to create the calibration line in this case. Porosity calibration lines for the four different groups are

Compensated neutron – dolomite

$$\Phi_{\text{core}} = -0.0231 + 0.82296 \times \Phi_{\text{NPHInorm}}$$

Compensated neutron – limestone

$$\Phi_{\text{core}} = -0.0358 + 1.1709 \times \Phi_{\text{NPHInorm}}$$

Sidewall neutron – dolomite

$$\Phi_{\text{core}} = -0.0178 + 1.0781 \times \Phi_{\text{SNPnorm}}$$

Sidewall neutron – limestone

$$\Phi_{\text{core}} = -0.0238 + 1.248 \times \Phi_{\text{SNPnorm}}$$

where Φ_{core} is the core-calibrated log porosity, Φ_{NPHInorm} is the normalized compensated neutron porosity, and Φ_{SNPnorm} is the normalized sidewall neutron porosity.

CONCLUSIONS

Porosity evaluation in large fields requires detailed attention to data quality control, but the level of quality control needed in a digital database can be acquired only through access to the original paper logs used to generate the digital data. Transcription and digitization errors can occur and, in some cases, well-bore information present on the paper logs is never captured.

Owing to the timing of log digitization, methods had to be developed for updating the database as new and re-edited log data was received to guarantee the logs being used were the most current, most edited versions. In the case of Fullerton Clear Fork, the sheer volume of data necessitated automating many of the processes.

Proper normalization is necessary to allow correct calibration to core porosity fieldwide. Traditional porosity log normalization methods failed to provide acceptable results. A novel normalization method was therefore applied that overcomes shortcomings of the other methods tried. This method, which involves both vertical averaging of log data by genetic interval and areal moving averages to extract trends in the local mean and standard deviation of target log

data is general in nature and should have wide applicability. The dual averaging, vertically and areally, has the effect of minimizing the effects of both random errors such as measurement noise and systematic errors associated with logging tool miscalibration. The normalization method outlined has advantages over other normalization methods in that any reasonably thick interval can be used to normalize the log, even the reservoir interval itself.

REFERENCE

Jennings, J. W., Jr., Lucia, F. J., and Ruppel, S. C., 2002, 3D modeling of stratigraphically controlled petrophysical variability in South Wason Clear Fork Reservoir: Society of Petroleum Engineers SPE Paper No. 77592, 15 p.

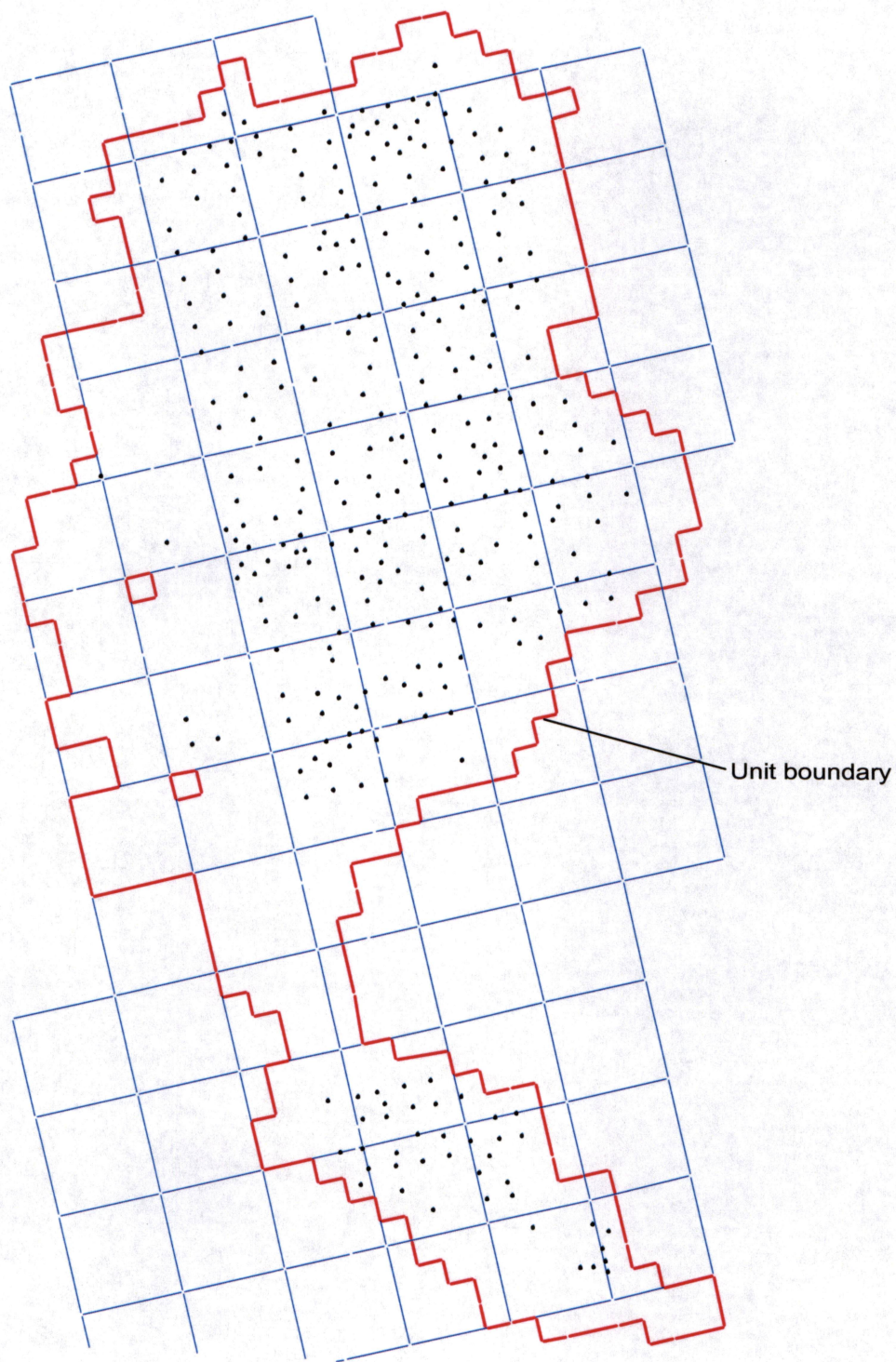


Figure 1. Map showing 316 wells with Sidewall neutron logs (SNP) used to calculate porosity for Fullerton Clear Fork field.

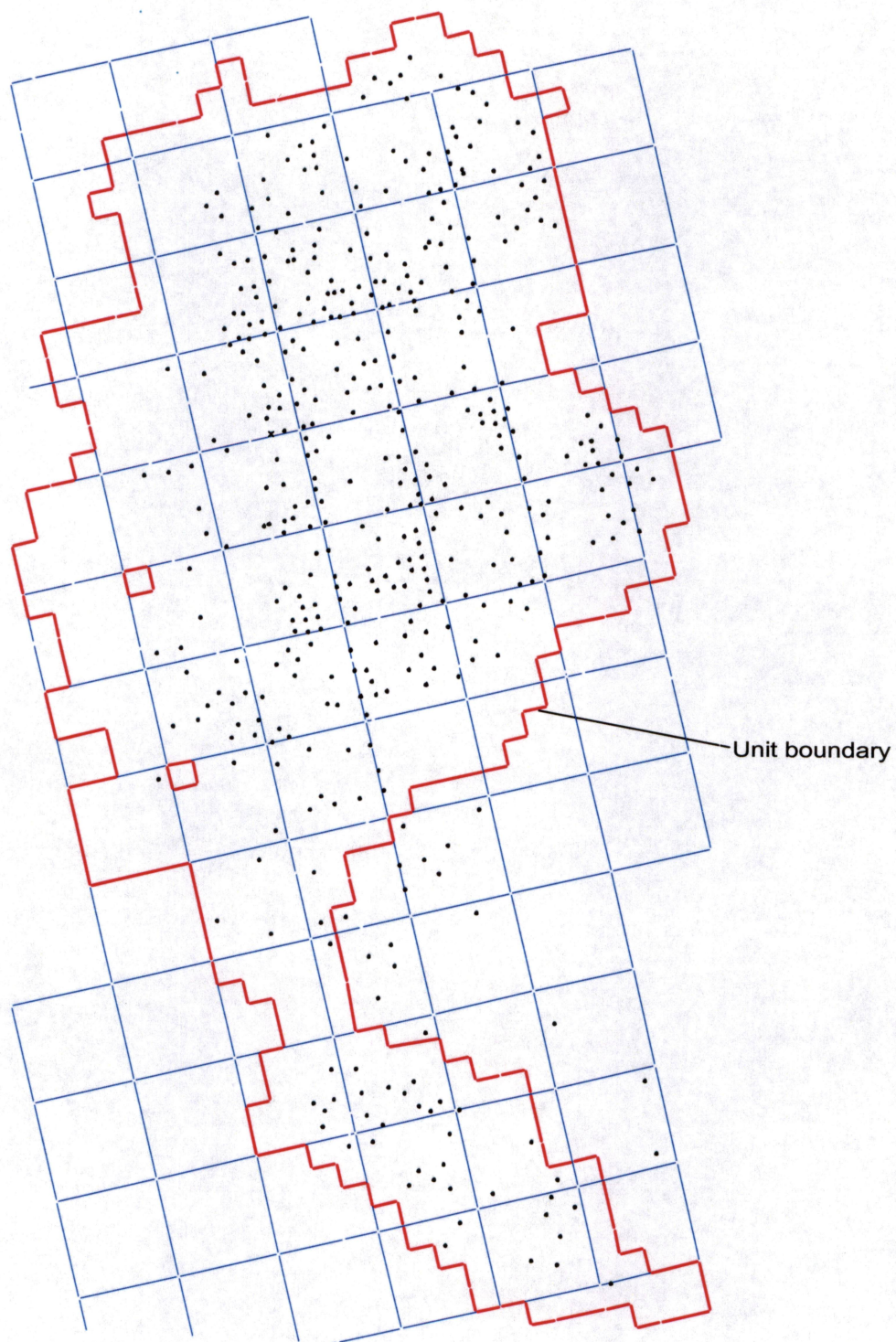


Figure 2. Map showing 437 wells with compensated neutron logs (NPHI) used to calculate porosity for Fullerton Clear Fork field.

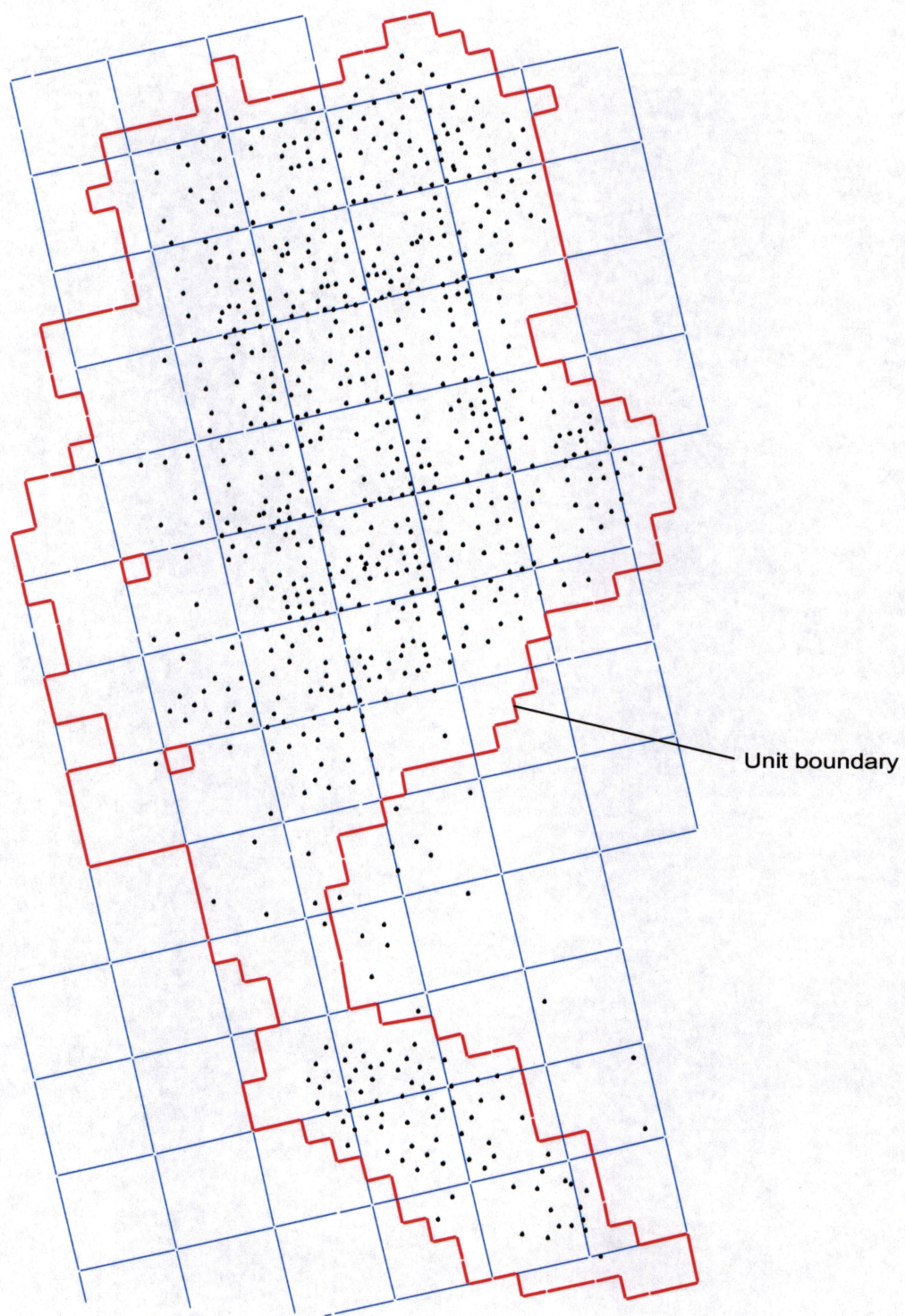


Figure 3. Map showing all 733 wells used in porosity calculation for Fullerton Clear Fork field.

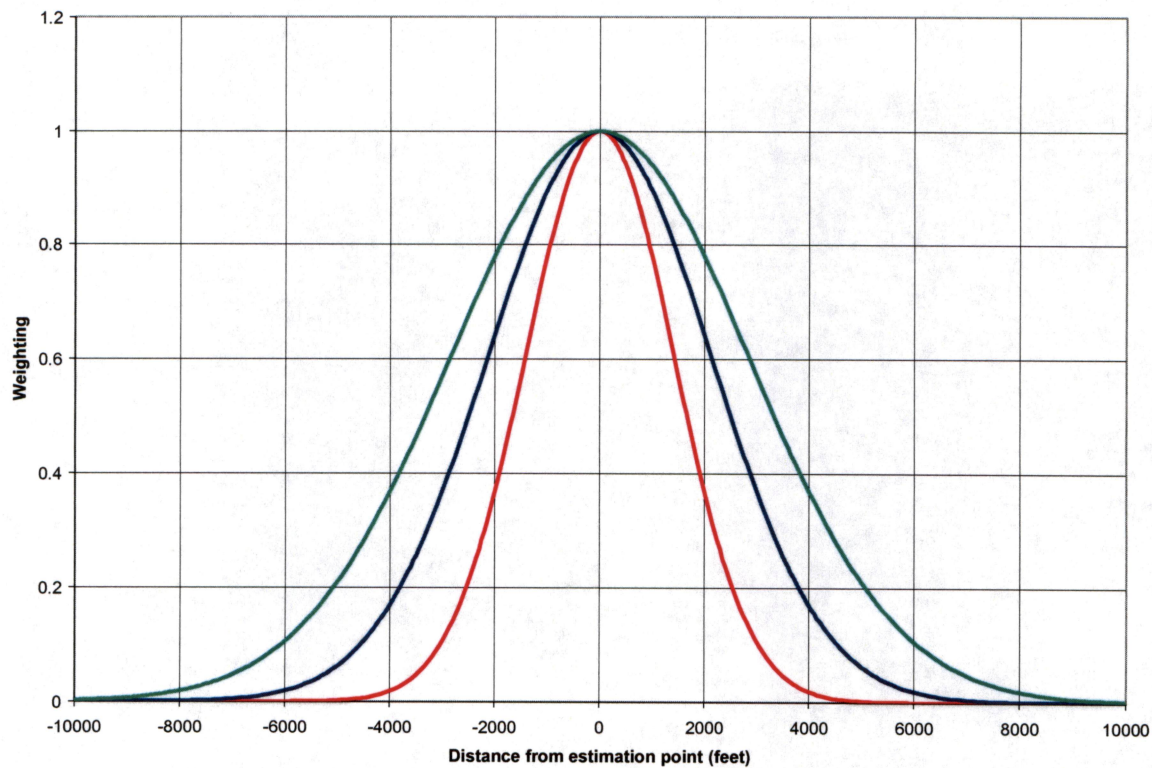


Figure 4. An example of the Gaussian weighting function using various scale factors. The red curve represents a scale factor of 2000 ft, blue 3000 ft and green 4000 ft. A scale factor of 3000 ft was used for porosity log normalization in the Fullerton field study.

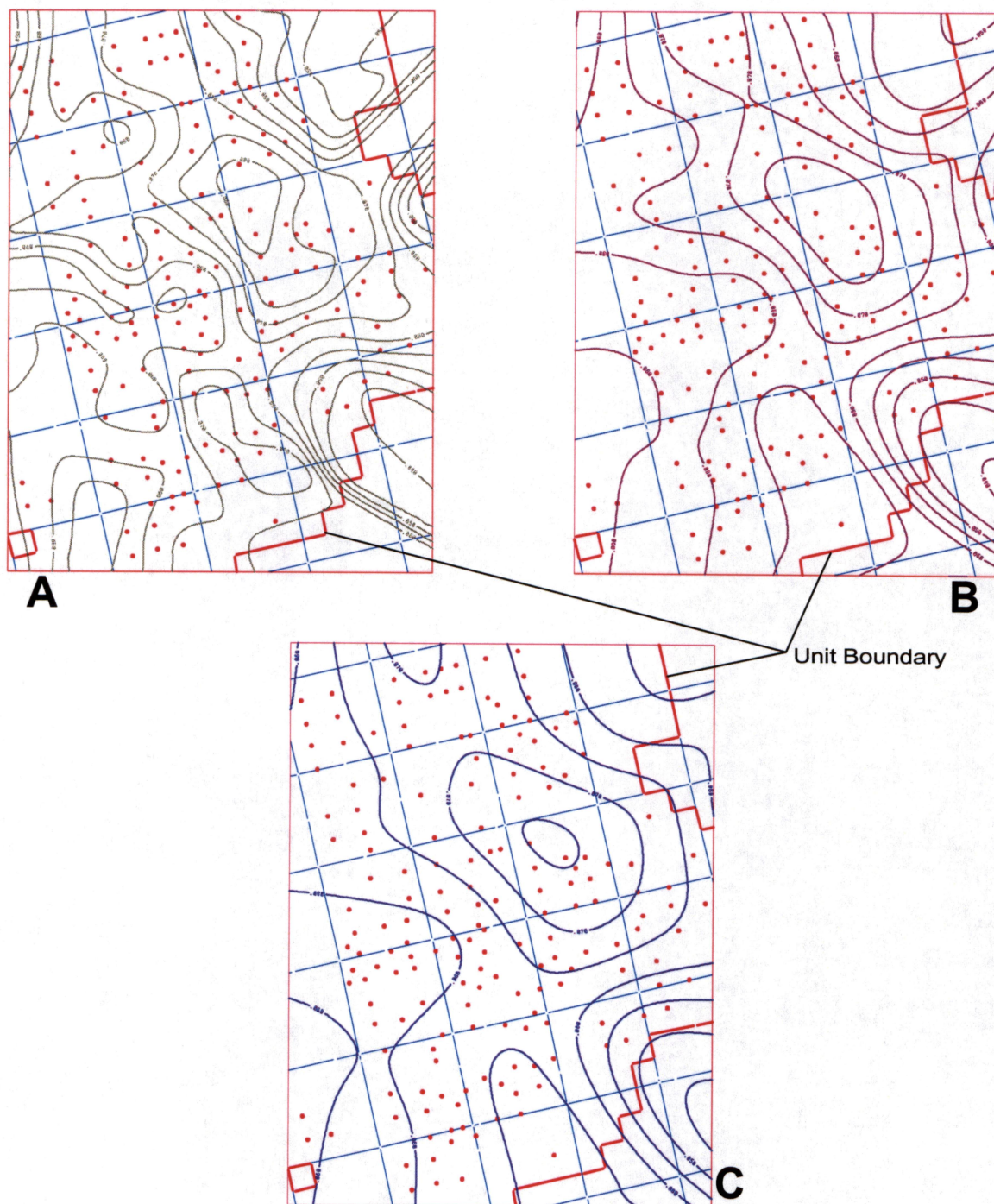


Figure 5. Examples of average SNP porosity areally averaged with different scale factors. Map A was generated using a 2000 foot scale factor, map B with a 3000 foot scale factor and map C, a 4000 foot scale factor. Red circles represent well control. Map A still contains “bull’s-eyes”, contours controlled by a single data point. Map C shows a lack of local variability, completely dominated by larger scale trends. Map B represents a reasonable compromise between local variability and larger scale trends. A scale factor of 3000 ft (map B) was used for porosity normalization in Fullerton Clear Fork field.

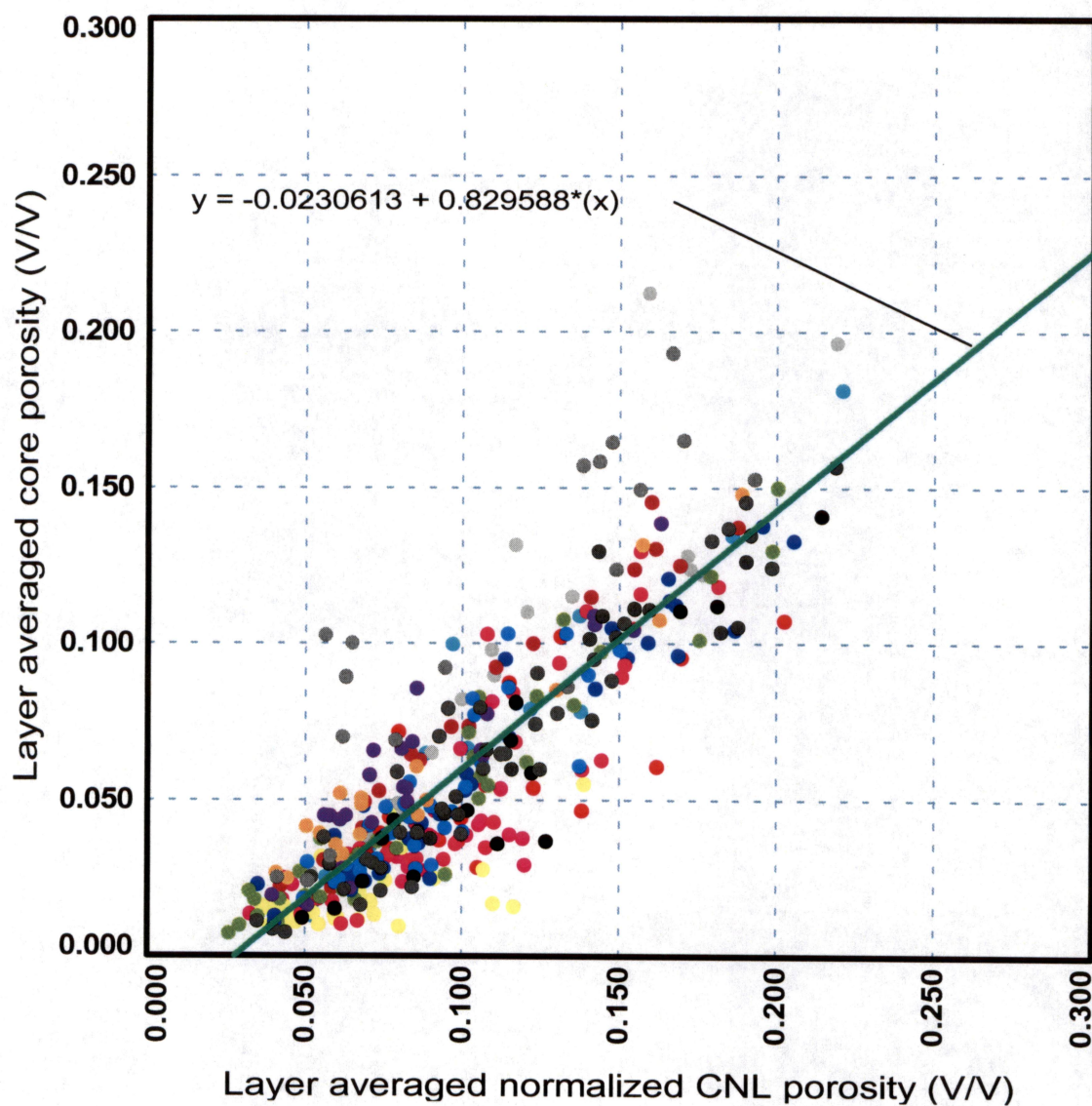


Figure 6. Plot of layer averaged core porosity (y-axis) as a function of layer averaged normalized compensated neutron porosity (x-axis) showing the calibration line for dolomites. Each point represents data that have been vertically averaged over a single cycle. Like colors represent data from the same well. Calibration is based on 21 wells.

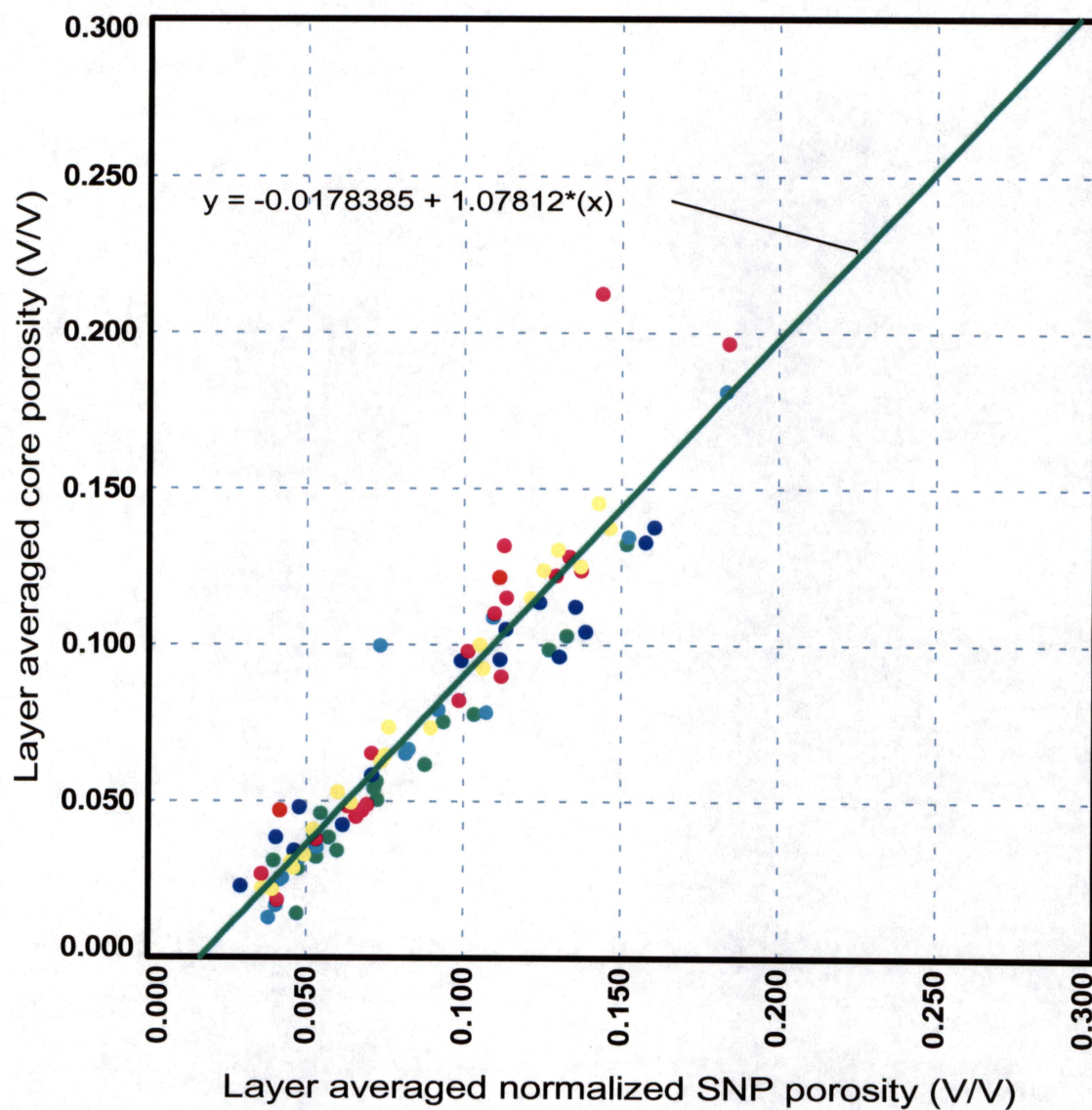


Figure 7. Plot of layer averaged core porosity (y-axis) as a function of layer averaged normalized sidewall neutron porosity (x-axis) showing the calibration line for dolomites. Each point represents data that have been vertically averaged over a single cycle. Like colors represent data from the same well. Calibration is based on six wells.

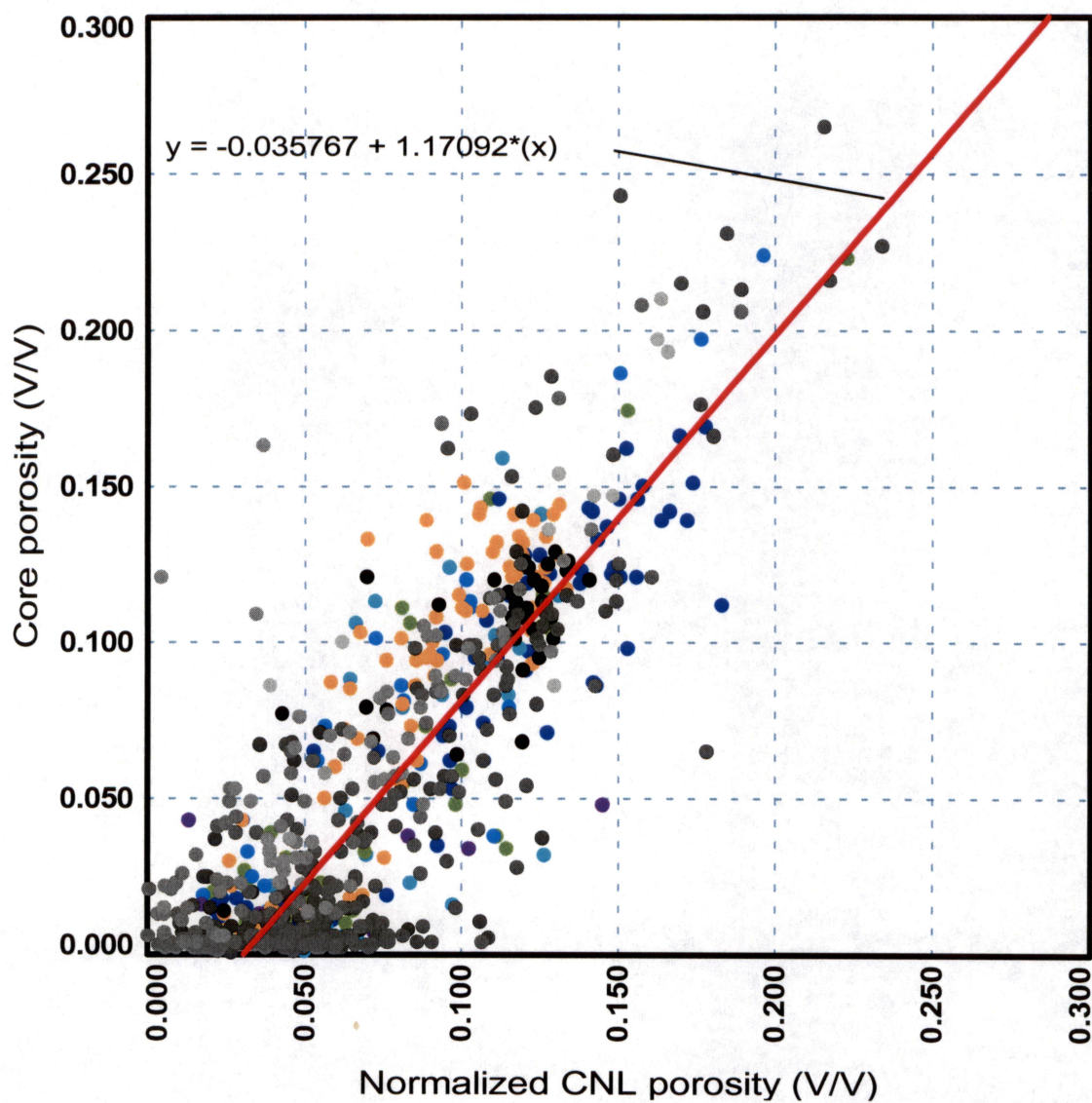


Figure 8. Plot of core porosity (y-axis) as a function of normalized compensated neutron porosity (x-axis) showing the calibration line for limestone. Each point represents an individual core sample. Only data where the photo-electric factor was greater than four was used in the generating the calibration. Like colors represent data from the same well. Calibration is based on 21 wells.

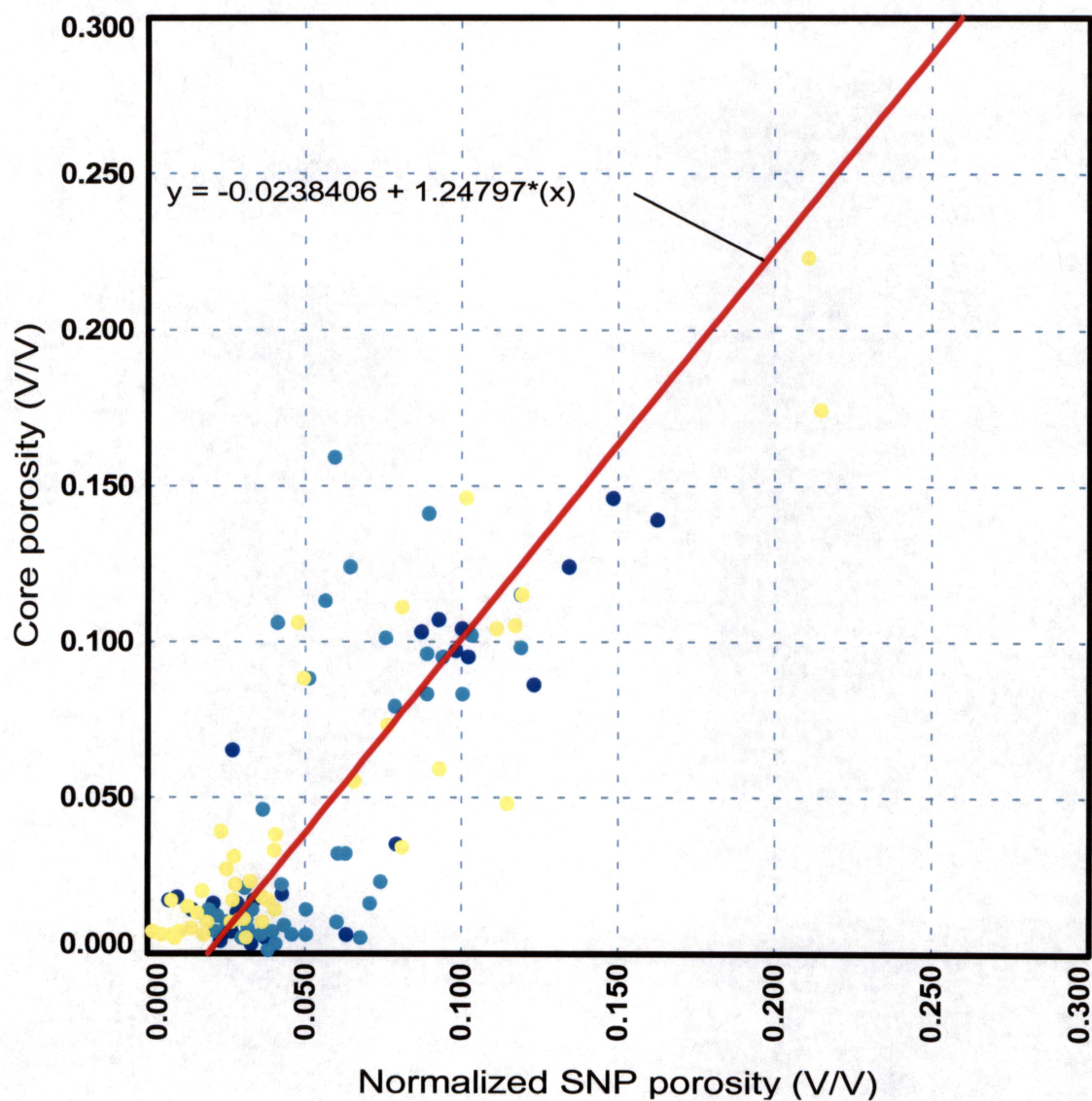


Figure 9. Plot of core porosity (y-axis) as a function of normalized sidewall neutron porosity (x-axis) showing the calibration line for limestone. Each point represents an individual core sample. Only data where the photo-electric factor was greater than four was used in the generating the calibration line. Like colors represent data from the same well. Calibration is based on five wells.

**CALCULATIONS OF PERMEABILITY AND INITIAL WATER SATURATIONS
FROM WIRELINE LOGS**

F. Jerry Lucia and Jeffrey A. Kane

**Bureau of Economic Geology
Scott W. Tinker, Director
John A. and Katherine G. Jackson School of Geosciences
The University of Texas at Austin
Austin, Texas 78713-8924**

ABSTRACT.....	193
PERMEABILITY CALCULATIONS FROM WIRELINE LOGS	194
ESTIMATION OF ORIGINAL WATER SATURATION.....	196
COMPARISON OF MODEL S_w WITH ARCHIE S_w	200
DISCUSSION	201
REFERENCES	202

Tables

1. Thomeer and core analysis values for class 2 samples	203
2. Thomeer and core analysis values for class 3 samples	203
3. List of electrical measurements from the Lower Clear Fork	204

Figures

1. Map showing location of calibration wells in the simulation area	205
2. Cross plots showing development of permeability transforms for dolostone in sequence L2.2	206
3. Comparison of core and calculated permeability in sequence L2.2	207
4. Porosity-permeability cross plot for moldic limestone in sequence L2.2.....	208
5. Comparison of core and calculated permeability in sequence L2.1	208
6. Comparison of core and calculated permeability in the Wichita peritidal facies	209
7. An example of fitting Thomeer parameters to a class 2 medium crystalline dolostone.....	210
8. Cross plots of Thomeer G factor and porosity for class 3 fabrics and class 2 fabrics showing little relationship between porosity and G factor	211
9. Cross plots of extrapolated entry pressures and porosity for class 3 fabrics and class 2 fabrics showing statistical relationships between entry pressure and porosity.....	212
10. Comparison of class 3 curves with curves calculated using the Thomeer model.....	213
11. Comparison of Thomeer class 3 capillary pressure model with generic class 3 model	214
12. Comparison of class 2 curves with curves calculated using the Thomeer model.....	215

13. Comparison of Thomeer class 2 capillary pressure model with generic class 2 model	216
14. Capillary pressure curves from moldic limestone	217
15. Comparison of capillary pressure curves from class 1 anhydritic dolostones with curves using the generic class 1 model	217
16. Example of model and Archie S_w from well FCU 5727.....	218

Calculations of Permeability and Initial Water Saturations from Wireline Logs

F. Jerry Lucia and Jeffrey A. Kane

ABSTRACT

Permeability is calculated from wireline logs using total porosity from wireline logs and apparent-rock-fabric number for stratigraphic relationships. Total porosity was used instead of interparticle porosity because the appropriate wireline logs needed to calculate interparticle porosity were not available. The use of total porosity required the use of an apparent-rock-fabric number, which was taken from stratigraphic relationships presented by Jones and others as part of this report. Permeability profiles were calculated using the global transform and compare reasonably well with core permeability values. The exception is in the lower section of the Wichita where karst fabrics are present suggesting a touching-vug pore system.

Initial water saturations were calculated using capillary pressure models. A generic model for class 1 fabrics was used and new models were developed for class 2 and 3 fabrics. The new models were developed using the Thomeer approach. Because most of the original wells had poor log suites and new wells were drilled after the advent of water flooding, calculation of initial water saturation from wireline logs was not feasible. However, calculations from capillary models appeared to match log calculations in intervals believed to be unflooded.

PERMEABILITY CALCULATIONS FROM WIRELINE LOGS

Permeability is calculated from wireline logs using the global porosity-permeability transform (eq. 1, 2). This equation was derived from a database of rock-fabric descriptions, interparticle porosity, permeability, and petrophysical-class values (Lucia, 1999; Lucia and others, 2001; Jennings and Lucia, 2003).

$$\text{LOG}(k) = ((a - b * \text{LOG}_{10}(\text{rfn})) + (c - d * \text{LOG}_{10}(\text{rfn})) * \text{LOG}_{10}(\text{ippor})) \quad (1)$$

or

$$\text{LOG}(k) = ((a - b * \text{LOG}_{10}(\text{arfn})) + (c - d * \text{LOG}_{10}(\text{arfn})) * \text{LOG}_{10}(\text{phi})) \quad (2)$$

where

rfn = rock-fabric number,

arfn = apparent rock-fabric number,

ippor = interparticle porosity,

phi = total porosity,

a = 9.7982,

b = 12.0838,

c = 8.6711, and

d = 8.2965.

Interparticle porosity and rock-fabric number are inserted into equation 1 to calculate permeability. However, as discussed by Jones and Lucia (this report), total porosity is used in the study because the abbreviated log suite available throughout the field does not allow for the calculation of interparticle porosity. Therefore, apparent rock-fabric number (ARFN) rather than rock-fabric number is used in equation 2, along with total porosity. The ARFN is provided by the relationship between rock-fabric petrophysical class and stratigraphy, as discussed by Jones and Lucia (this report), and total porosity is from porosity logs (Kane, this report).

The method was tested on six cored wells in the simulation area (fig. 1) with good to excellent results. Sequence L2.2 is composed of anhydritic dolostone with a small area of limestone. Whereas an ARFN of 1 was used throughout the full field, a more rigorous approach to assigning ARFN's was applied in the simulation area. In the dolostone area a statistical transform was developed that used multiple ARFN's. The porosity-permeability cross plot (fig. 2a) shows that most of the data fall within the class 1 field. However, the statistical line trends into the class 2 field. The statistical line could have been used to calculate permeability in the dolostone facies. However, an ARFN is required to use the global transform. Therefore, a relationship between porosity and ARFN was developed (fig. 2b), and ARFN's calculated from the porosity log were used in the global transform. This method could not be applied throughout the field and was replaced with an ARFN of 1. As shown in figure 3a the match between core and calculated permeability values is quite good using an ARFN of 1.

A small area of limestone is present in sequence L2.2, and the porosity and permeability data plot along the class 2-3 boundary, indicating an ARFN of 2.5 (fig. 4). The data plot along the class 2-3 boundary using total porosity because the porous limestone is dominated by moldic class 1 grainstone and class 2 grain-dominated packstone, and grain molds do not add significantly to permeability. The data would plot in the appropriate class field if moldic porosity were subtracted from total porosity. As shown in figure 3b the match between core and calculated permeability values is quite good using an ARNF of 2.5 except for 5 to 10 ft of high permeability toward the top. This interval contains a large crystalline dolostone, which is an anomalous fabric in this area.

The upper interval of sequence L2.1 is composed of peritidal facies characterized by an ARFN of 3. The lower interval is composed of subtidal dolostones and limestones that could not

be mapped separately. An ARFN of 2 was used to calculate permeability because the porous limestones are moldic grain-dominated fabrics that tend to plot in the class 2 field and, in general, the dolostones are class 2 medium crystalline grain-dominated dolopackstones and wackestones (see Jones and Lucia, this report). As illustrated in figure 5, there is a good match between core and calculated permeability.

The Wichita is dominated by peritidal facies characterized by an ARFN of 3, and the comparison illustrated in figure 6 shows a good correlation between core and calculated permeability in sequence L2, except for a few permeability spikes that are assumed to be sample bias. In sequence L1 the log calculations tend to underestimate permeability. A few core descriptions and one image log show collapse breccia in this interval (fig. 6b), suggesting the presence of fracturing due to karsting and collapse that may account for higher than predicted permeability in this area. As discussed by Wang (this volume), in conjunction with building the simulation model the matrix permeability estimates were increased about 20 times in order to match injection.

ESTIMATION OF ORIGINAL WATER SATURATION

Estimates of initial water saturation (S_w) were made using a capillary pressure model. There are several methods for doing this, the most popular being the Leverett J function, which relates saturation to reservoir height and the ratio of permeability and porosity (k/ϕ), where k/ϕ is a measure of pore size. The difficulty with this method is that a permeability value is required. Permeability is often obtained from a single porosity-permeability transform, which results in S_w being a function of porosity only and not pore size. However, it is well known that S_w is a function of pore size as well as reservoir height. Lucia (1995) showed that the combination of rock fabric and interparticle porosity is a measure of pore size and that S_w is a

function of rock-fabric petrophysical class, porosity, and reservoir height. The difficulty with this method is the requirement for a petrophysical-class value. In this study, initial water saturation was calculated using petrophysical class obtained from rock-fabric stratigraphy, as described by Jones and Lucia (this report), porosity from wireline logs, and reservoir height assuming a zero capillary pressure level at -4,100 ft. The presence of multiple oil-water contacts suggested in past field studies was not investigated. However, the evidence presented for multiple oil-water contacts is thought to be equivocal.

Initially we used the generic relationships derived by Lucia (1995):

$$\text{Class 1 } S_w = 0.02219 \times H^{-0.316} \times \phi^{-1.745} \quad (3)$$

$$\text{Class 2 } S_w = 0.1404 \times H^{-0.407} \times \phi^{-1.440} \quad (4)$$

$$\text{Class 3 } S_w = 0.6110 \times H^{-0.505} \times \phi^{-1.210} \quad (5)$$

where

S_w = water saturation in fraction,

H = reservoir height in feet, and

ϕ = porosity in fraction (assuming that little vuggy porosity is present).

During the progress of the field study new capillary pressure data were obtained. The samples were selected on the basis of rock-fabric descriptions and porosity. Comparing the generic models with the new capillary pressure data indicated that the class 2 and 3 generic models overestimate water saturation, suggesting the need for a new saturation model.

The new models were developed using the Thomeer (1960) method for characterizing capillary pressure curves. The Thomeer method estimates the irreducible water saturation, entry

pressure, and shape of the capillary pressure curve (the G factor) from a cross plot of percent bulk-volume of mercury occupied and entry pressure corrected for surface effects.

$$(BV_{occ}/BV_{inf}) = 2.71828^{(-G/(\text{LOG}(P_c/P_d)))}$$

where

BV_{occ} = fraction of bulk volume occupied by mercury in fraction,

BV_{inf} = fraction of bulk volume occupied by mercury extrapolated to infinite pressure,

G = Thomeer parameter related to shape of capillary pressure curve,

P_c = capillary pressure in psi, and

P_d = entry capillary pressure corrected for surface effects in psi.

Using a spreadsheet program developed by Ed Clerke of Aramco Petroleum Company, parameters were selected until a reasonable match was made between the data and the model (fig. 7). In several cases a bimodal fit was required and the fit to the lowest pressure data was used in the model. In all cases the BV_{inf} approximated the total porosity because injection pressures of greater than 50,000 psi were used in the measurements. Therefore, BV_{occ}/BV_{inf} is assumed to be S_w. The samples were grouped by petrophysical class, and porosity was correlated to the G factor and to the extrapolated entry pressure. The data are presented in tables 1 and 2. There is little correlation between porosity and G factor for class 2 and class 3 (fig. 8). The average value for class 2 was 0.2, and the average value for class 3 was 0.1, suggesting that there may be a relationship between rock fabric and G. Extrapolated entry pressure correlated quite well with porosity for both class 2 and class 3 rocks, although the correlation was different in each case (fig. 9).

The resulting saturation models for class 2 and 3 are given below:

$$S_{hg} = (BV_{occ}/BV_{inf}) = 2.71828^{(-G/(\text{LOG}(P_c/P_d)))},$$

assuming total porosity filled with mercury at infinite pressure.

or

$$S_w = 1 - [2^{-G/(\text{LOG}(P_c/P_d))}]$$

$$P_c = 1.191H \text{ (based on field data)}$$

Class 2

$$G = 0.2$$

$$P_d = 0.0768067 * \Phi^{-2.8394}$$

$$S_w(\text{Class 2}) = 1 - [2.71828^{-0.2/(\text{LOG}(P_c/(0.0768067 * \Phi^{-2.8394})))})]$$

or in terms of H,

$$S_w(\text{Class 2}) = 1 - [2.71828^{-0.2/(\text{LOG}(15.5064 * H / \Phi^{-2.8394})))}]$$

Class 3

$$G = 0.1$$

$$\text{Class 3 } P_d = 3.1117 * \Phi^{-1.9717}$$

$$S_w(\text{Class 3}) = 1 - [2.71828^{-0.1/(\text{LOG}(P_c/(3.1117 * \Phi^{-1.9717})))})]$$

or in terms of H,

$$S_w(\text{Class 3}) = 1 - [2.71828^{-0.1/(\text{LOG}(0.3827 * H / (\Phi^{-1.9717})))}]$$

The new capillary pressure models were compared with capillary pressure data and with the original generic models by visual inspection. The new class 3 model compares well with the original data but provides somewhat high S_w values at high capillary pressures (figs. 10a, 10b). This may be due to using only data from the lower curve of the dual-porosity curves to develop the S_w equations. The new model calculates significantly lower S_w values than the generic model (fig. 11a, 11b). The new class 2 model compares well with the original data in the low-porosity and high-porosity ranges (figs. 12a and 12c) but provides somewhat low S_w values in the mid-porosity range (fig. 12b). It calculates significantly lower S_w values than the generic model (fig 13a, 13b).

Class 1 oomoldic grainstone capillary pressure curves, illustrated in figure 14, are similar to class 3 curves (fig. 11). Oomoldic grainstones are found interbedded with class 2 dolostone, and an ARFN of 2 was used to estimate initial S_w . This results in underestimating initial S_w for the oomoldic grainstones interbedded with class 2 dolostones. In the limestone sector of the phase 1 area an ARFN of 2.5 was used to estimate permeability. However, only three capillary pressure models were used in this study, and the class 3 model was selected to estimate initial S_w in the limestone area.

Six capillary pressure curves from the anhydritic dolostone interval in sequence L2.2 were obtained and are illustrated in figure 15. The curves are comparable to the generic class 1 capillary pressure model. An ARFN of 1 was used to calculate initial S_w for the anhydritic dolostone, and no new model was needed.

COMPARISON OF MODEL S_w WITH ARCHIE S_w

An example comparison of water saturations calculated from capillary models and from Archie's equation is presented in figure 16. Two of the three principal inputs into the capillary pressure model are illustrated: porosity and petrophysical class. Archie water saturations were calculated using an m and n of 2, which is supported by laboratory measurements listed in table 3. Water resistivity was estimated at 0.04 ohmms. Waterflooding was initiated in 1961, and most of the field was under waterflood by 1973. As a result, capillary pressure S_w values are expected to be equal to or lower than Archie values.

Examination of figure 16 shows intervals of class 2 and 3 where model S_w and Archie S_w match closely. This suggests that the capillary pressure models give reasonable estimates of original water saturation. However, in many porous intervals Archie S_w is higher than model S_w . These intervals are considered to contain flood water. Because flood water is less saline and

more resistive than 0.04 ohmms, the Archie S_w is considered to underestimate S_w in the flooded intervals. The upper 20 ft shown in figure 16 illustrates the common observation that Archie S_w values are unreliable when porosity is less than 5 to 6 percent.

A calculation of original water saturation using the Archie equation could not be made because of the poor quality of the original wireline logs and the long history of waterflooding. An attempt was made to use the early resistivity logs and more modern porosity logs from adjacent wells to calculate Archie S_w . In addition, Archie S_w was calculated for wells having initial low water production that might not have been completely flooded at the time of logging. No robust conclusion could be drawn from these results because the effects of injection water could not be adequately accounted for.

DISCUSSION

The stratigraphic approach used to predict apparent rock-fabric number together with total porosity results in reasonable estimates of matrix permeability using the global transform equation. The estimates of matrix permeability are considered to be highly reliable in the simulation area. However, they are less reliable outside of the simulation area because no detailed calibration between apparent rock-fabric number and stratigraphy was made. Additional detailed studies should be done in areas of future simulation modeling.

These results are achieved despite the grouping of limestones and dolostones and grain-dominated and mud-dominated fabrics. The fabrics tend to group in the class 2 field because the presence of grain molds in the grainstone moves the plot-points into the class 2 field and the conversion of the limestone into a medium crystalline dolostone moves the mud-dominated dolostones into the class 2 field. The mud-dominated limestones are tight and are not an issue. The peritidal facies can be correlated and are typically class 3 fine crystalline dolostones. In

sequence L1, however, there appears to be a touching-vug pore system, and matrix porosity and the permeability values are understated.

The new capillary pressure models for calculating initial S_w in the class 2 and 3 fabrics fit the capillary pressure data better than the generic models. Limited comparisons with Archie S_w calculations suggest that the model saturations are reasonable. The zero capillary pressure level of -4,100 was used to minimize the transition zone effect at the base of the reservoir. We have no real data to support this but assume that the Wichita and Lower Clear Fork are one reservoir. We know of no conclusive evidence for multiple reservoirs.

REFERENCES

- Jennings, J. W., Jr., and Lucia, F. J., 2003, Predicting permeability from well logs in carbonates with a link to geology for interwell permeability mapping: Society of Petroleum Engineers Reservoir Evaluation & Engineering, v. 6, no. 4, p. 215–225.
- Lucia, F. J., 1995, Rock-fabric/petrophysical classification of carbonate pore space for reservoir characterization: American Association of Petroleum Geologists Bulletin, v. 79, no. 9, p. 1275–1300.
- Lucia, F. J., 1999, Carbonate reservoir characterization: New York, Springer-Verlag, 226 p.
- Lucia, F. J., Jennings, J. W., Jr., Rahnis, M. A., and Meyer, F. O., 2001, Permeability and rock fabric from wireline logs, Arab-D reservoir, Ghawar field, Saudi Arabia: GeoArabia, v. 6, no. 4, p. 619–646.
- Thomeer, J. H. M., 1960, Introduction of a pore geometrical factor defined by the capillary pressure curve: American Institute of Mining, Metallurgical, and Petroleum Engineers Transactions, v. 219, p. 354–358.

Table 1. Thomeer and core analysis values for class 2 samples (MxIMDDstn = Medium crystalline mud-dominated dolostone; GDDP = Grain-dominated dolopackstone).

Depth	Sample No.	Well FCU	G factor	Pd (psi)	Bvinf	Phi (%)	Perm (md)	Rock Fabric	Pet. Class
6822	10	6429	0.1	150	1.5	10.7	1.13	MxIMDDstn	2
6855	42	6429	0.1	100	2	14.4	5.6	GDDP	2
6907	94	6429	0.2	75	8	8.6	0.53	MxIMDDstn	2
6908	95	6429	0.5	50	10	10.1	8.3	MxIMDDstn	2
6991	98	5927	0.4	60	8	8.4	0.28	MxIMDDstn	2
6995	102	5927	0.2	25	12	12.8	9.76	MxIMDDstn	2
6813	1	6429	0.3	10	13	12.5	9.63	GDDP	2
6818	6	6429	0.25	80	9	11.6	2.38	GDDP	2
6914	101	6429	0.2	20	18	17.5	16.23	GDDP	2
6915	102a	6429	0.3	40	18	18.5	16.3	GDDP	2
6938	57	5927	0.2	100	8	8.0	0.58	MxIMDDstn	2

Table 2. Thomeer and core analysis values for class 3 samples (FxIMDDstn = Fine crystalline mud-dominated dolostone).

Depth	Sample No.	Well FCU	G factor	Pd (psi)	Bvinf	Phi (%)	Perm (md)	Rock Fabric	Pet. Class
7001	108	5927	0.12	150	17	17.9	0.99	FxIMDDstn	3
7002	109	5927	0.15	56	23	23.6	5.66	FxIMDDstn	3
7003	110	5927	0.12	140	14	14.2	0.6	FxIMDDstn	3
7004	111	5927	0.13	300	3	20.1	0.88	FxIMDDstn	3
7007	114	5927	0.13	150	5	26.2	15.9	FxIMDDstn	3
7009	116	5927	0.15	120	15	15.7	0.95	FxIMDDstn	3
7044	147	5927	0.13	80	18	18.6	3.79	FxIMDDstn	3
7045	148	5927	0.13	100	19	19.1	2.64	FxIMDDstn	3
7054	157	5927	0.2	175	10	10.5	0.232	FxIMDDstn	3
7056	159	5927	0.13	100	19	19.5	1.93	FxIMDDstn	3
7059	162	5927	0.13	100	15	15.9	0.45	FxIMDDstn	3
7089	192	5927	0.15	200	13	13.3	0.267	FxIMDDstn	3

Table 3. List of electrical measurements from the Lower Clear Fork (GDDP = Grain-dominated dolopackstone; Gstn = Grainstone; MDDP = Mud-dominated dolopackstone).

Well	Formation	Sp No.	Rock Fabric	Separate Vug (%)	Pet. Class	M	N
FCU 6429	LCF	1	GDDP	2	2	2.05	2.04
FCU 6429	LCF	6	GDDP	3	2	2.22	2.20
FCU 6429	LCF	8	GDDP	2	1	1.86	1.97
FCU 6429	LCF	2	GDDP	0	1	1.86	1.94
FCU 5927	LCF	2	Moldic Gstn	12	1	2.04	2.10
FCU 5927	LCF	3	Moldic Gstn	20	1	2.14	2.11
FCU 5927	LCF	3	Moldic Gstn	15	1	2.13	2.02
FCU 6429	LCF	32a	GDDP	0	1	1.85	1.91
FCU 5927	LCF	35	Moldic Gstn	7	1	2.05	1.95
FCU 6429	LCF	35a	GDDP	2	1	1.89	1.85
FCU 5927	LCF	57	MDDP	1	2	1.83	1.87
FCU 6429	LCF	100	GDDP	0	1	1.84	1.91
FCU 6429	LCF	101	GDDP	1	2	1.89	1.94
FCU 6429	LCF	102a	GDDP	0	2	1.88	1.89
Average						1.96	1.98

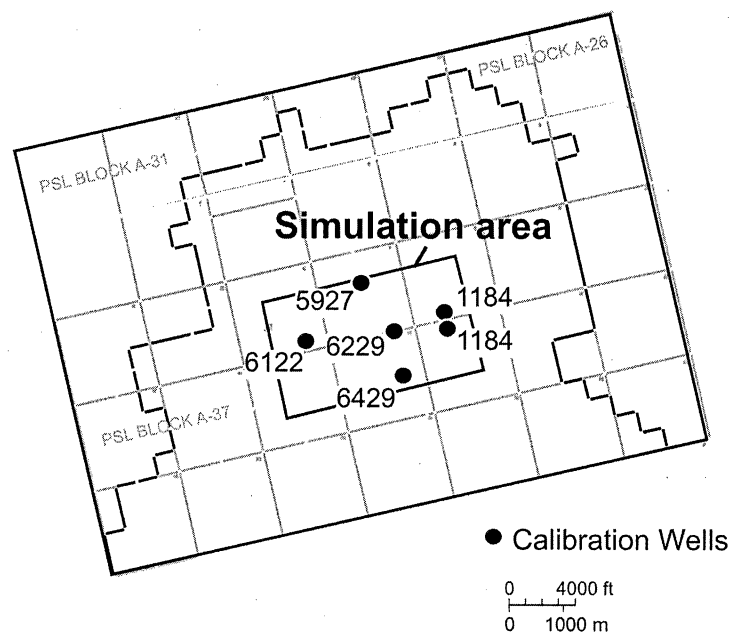


Figure 1. Map showing location of calibration wells in the simulation area.

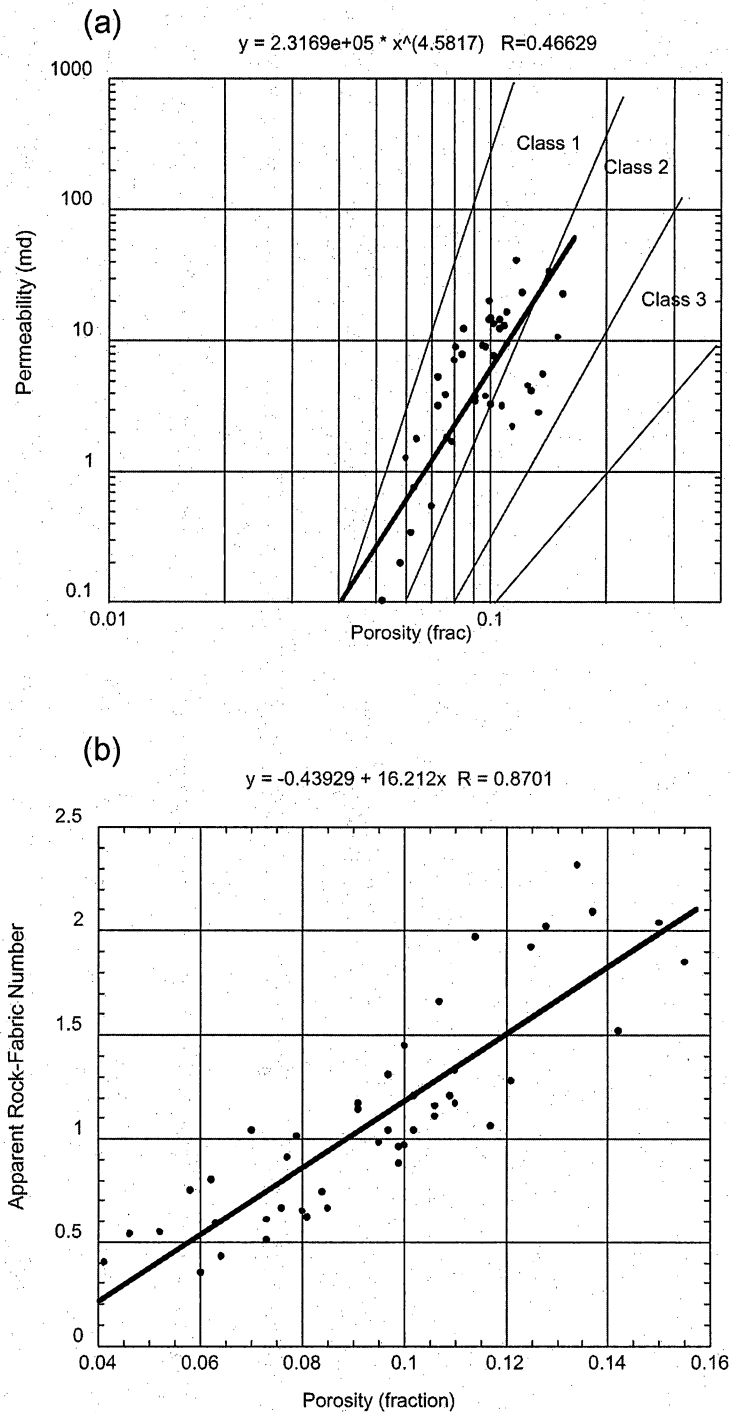
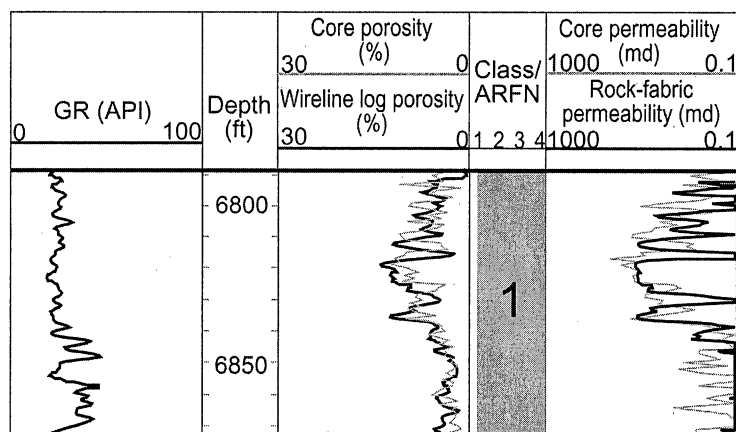


Figure 2. Cross plots showing development of permeability transforms for dolostone in sequence L2.2. (a) Porosity-permeability cross plot showing that most of the points fall in the class 1 field. A class 1 transform was used in the full field model. (b) Apparent rock-fabric number (ARFN) calculated from core data is plotted against porosity and the relationship used in uncored wells to calculate ARFN for use in the global transform equation.

(a)



(b)

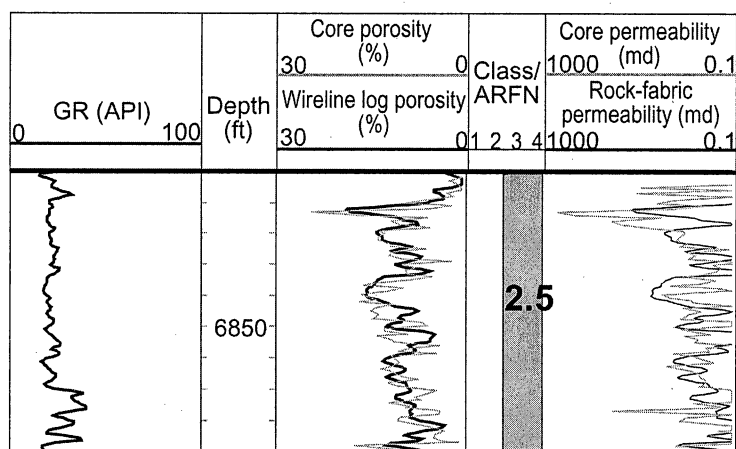


Figure 3. Comparison of core and calculated permeability in sequence L2.2. (a) Comparison in the dolostone intervals using a class 1 transform instead of the method outline line figure 2. (b) Comparison in the limestone area using the ARFN 2.5 transform. The high permeability in the upper 10 ft is a class 1 large crystalline dolostone.

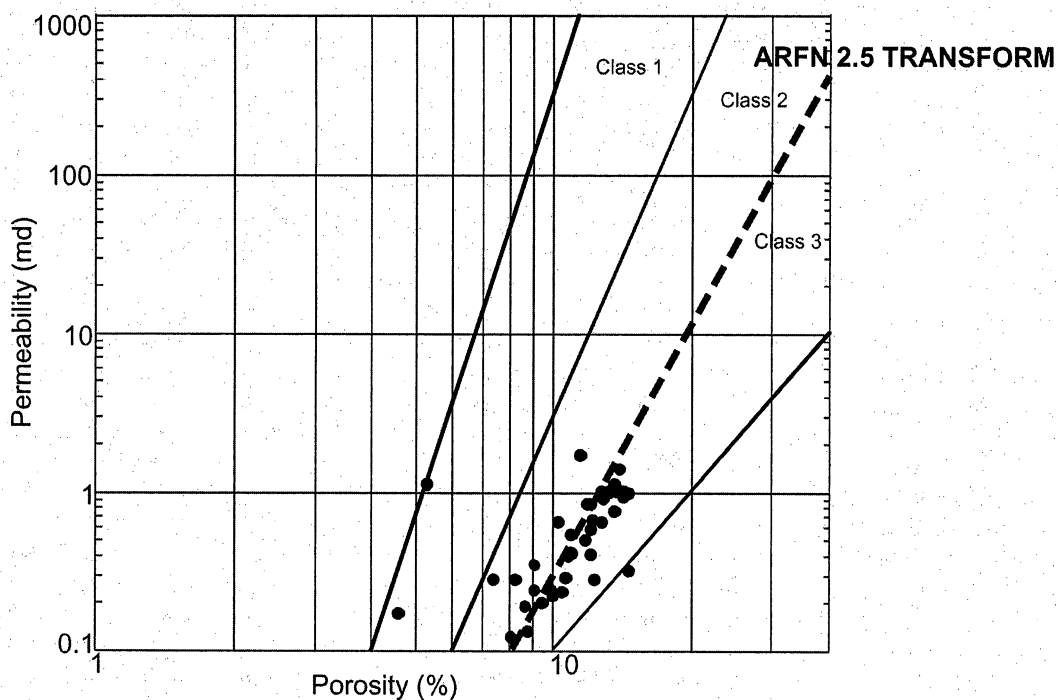


Figure 4. Porosity-permeability cross plot for moldic limestone in sequence L2.2. The data cluster along the class 2-3 boundary because moldic porosity adds little to permeability.

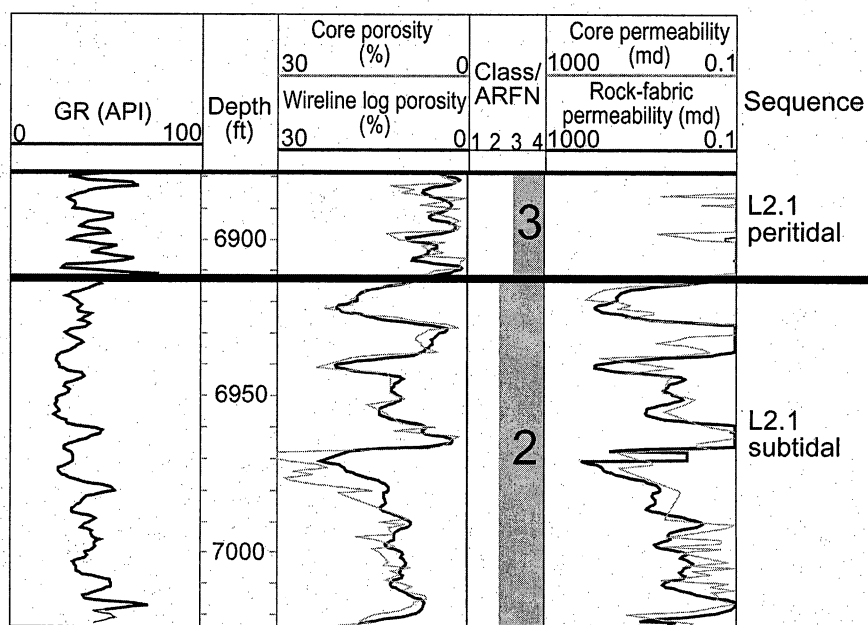


Figure 5. Comparison of core and calculated permeability in sequence L2.1. A class 3 transform is used in the upper peritidal interval and class 2 in the subtidal interval.

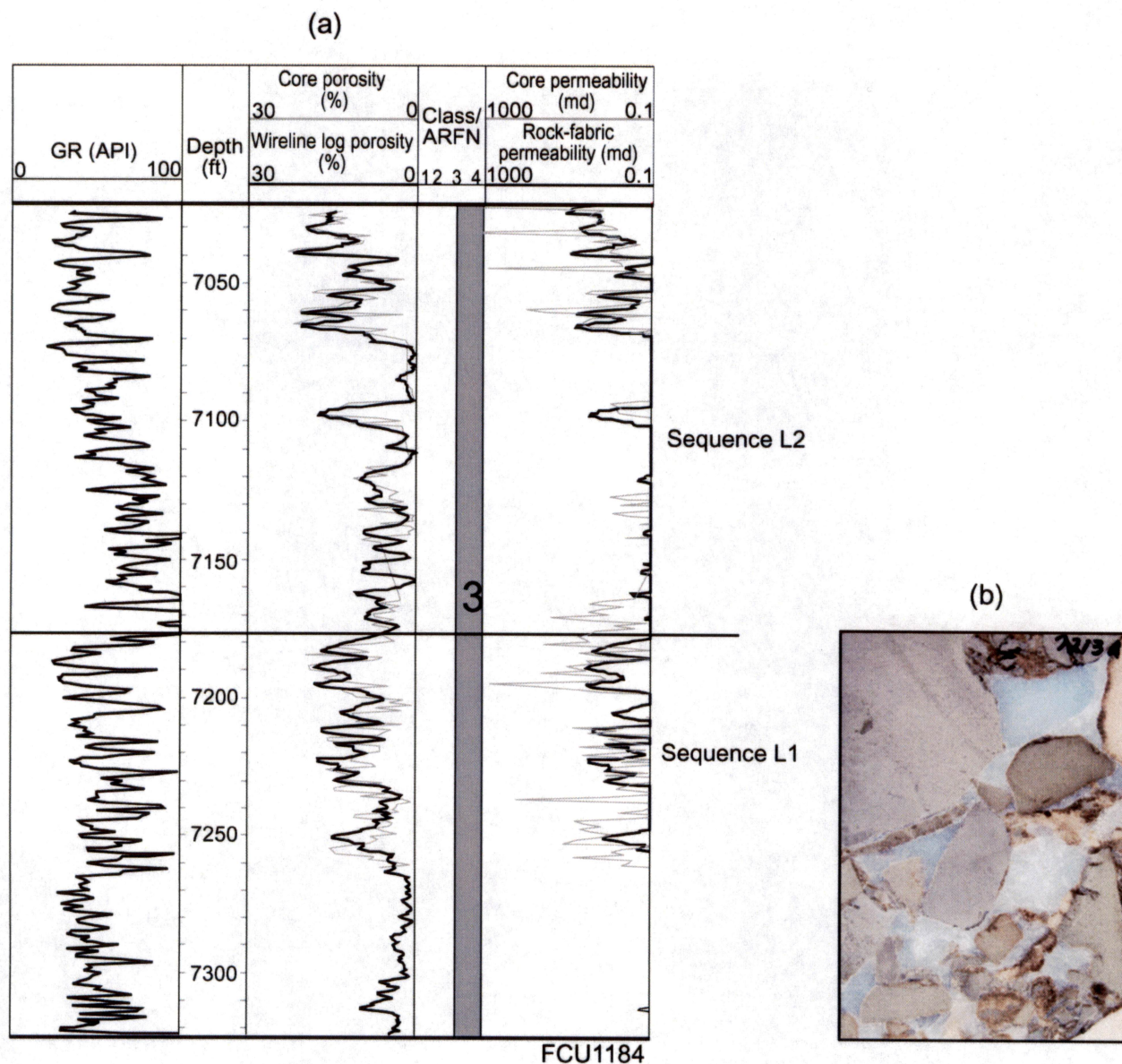


Figure 6. Comparison of core and calculated permeability in the Wichita peritidal facies. (a) A comparison of core and calculated permeability showing good correlation in sequence L2 and poor correlation in L1. (b) A core photograph of karst breccia found in L1 suggesting a touching-vug pore system.

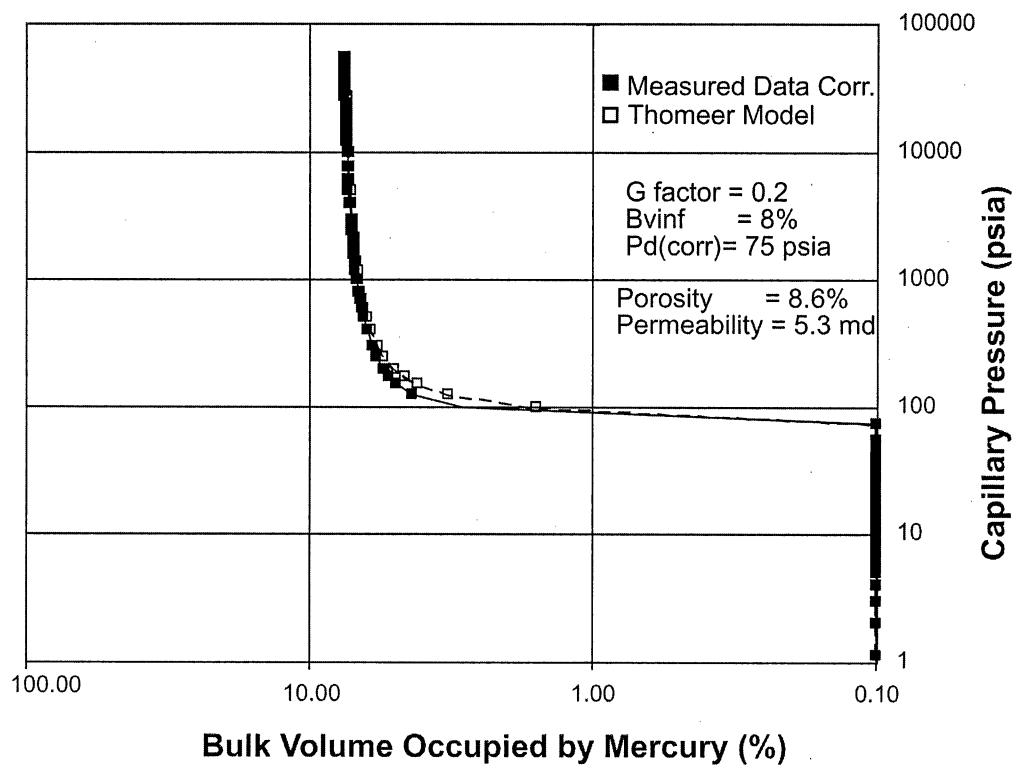


Figure 7. An example of fitting Thomeer parameters to a class 2 medium crystalline dolostone.

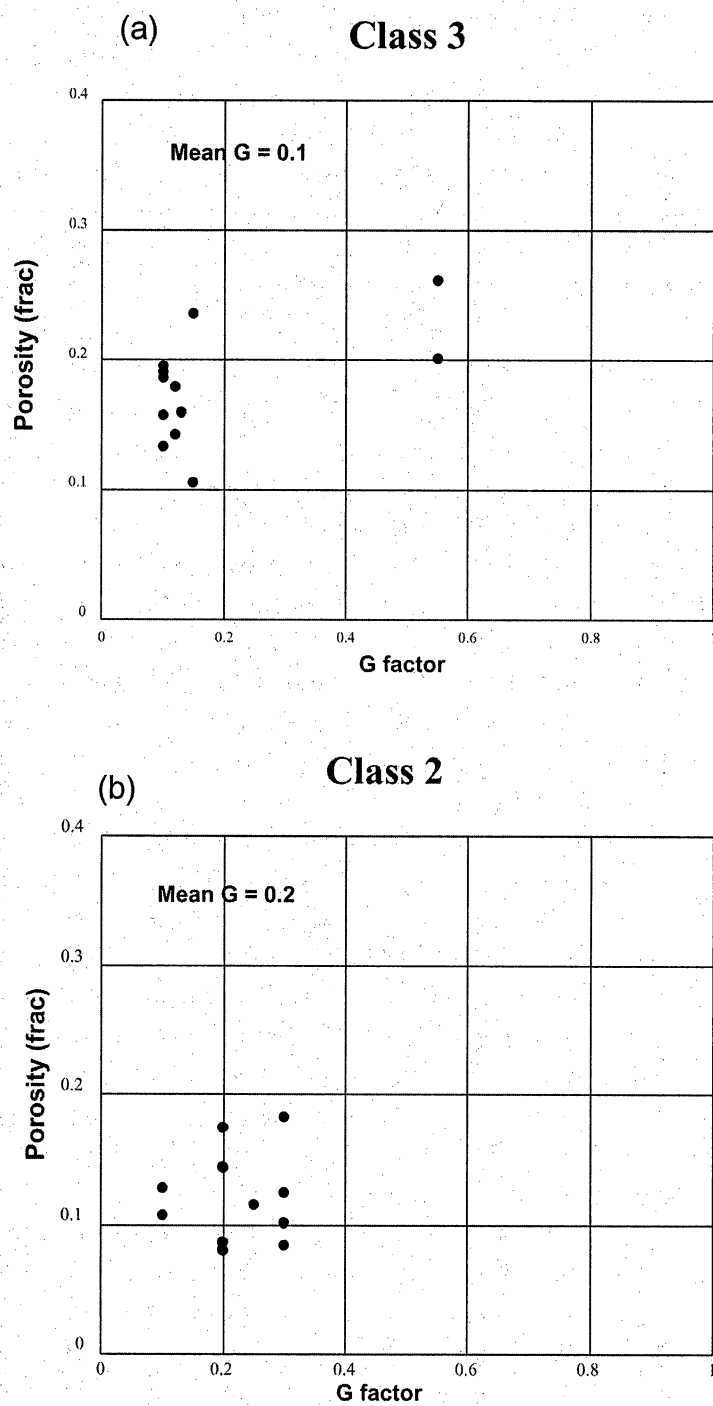
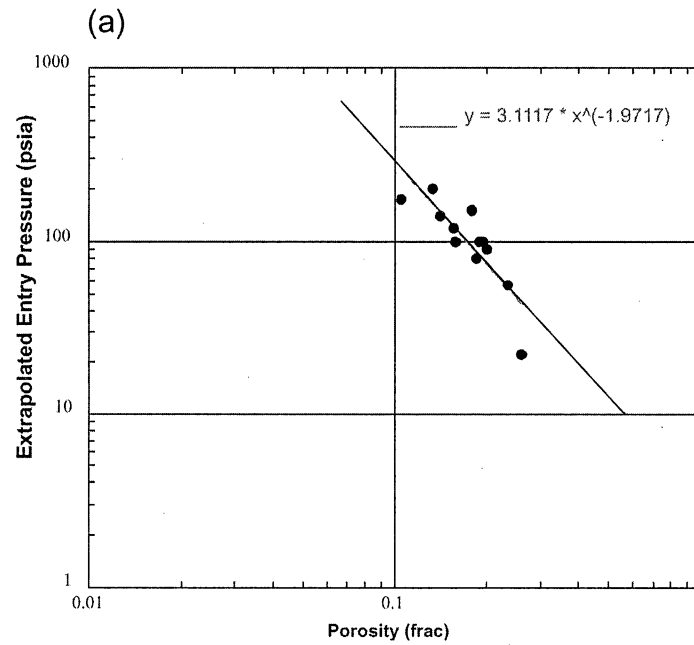


Figure 8. Cross plots of Thomeer G factor and porosity for (a) class 3 fabrics and (b) class 2 fabrics showing little relationship between porosity and G factor. Several of the class 3 samples are bimodal and require two curves to fit, and both G factors are presented in figure a.

Class 3



Class 2

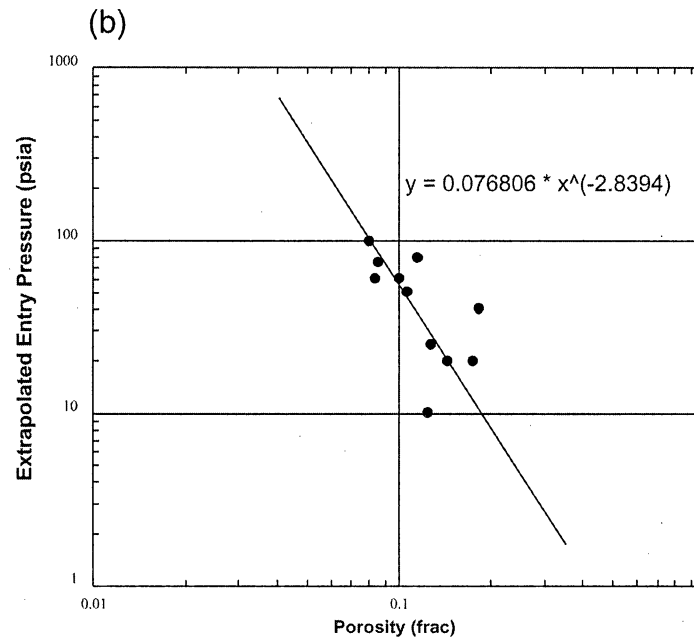


Figure 9. Cross plots of extrapolated entry pressures and porosity for (a) class 3 fabrics and (b) class 2 fabrics showing statistical relationships between entry pressure and porosity.

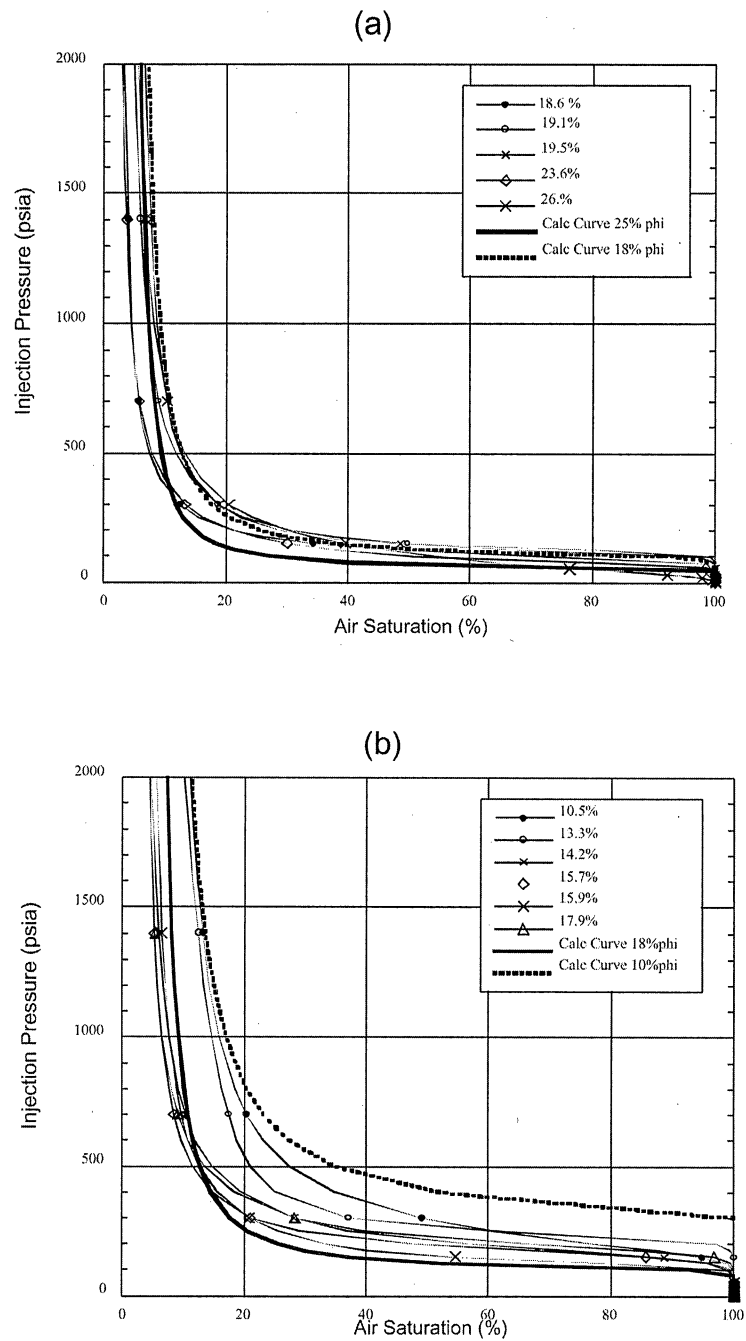


Figure 10. Comparison of class 3 curves with curves calculated using the Thomeer model.
 (a) Porosity less than 18 percent and (b) porosity greater than 18 percent.

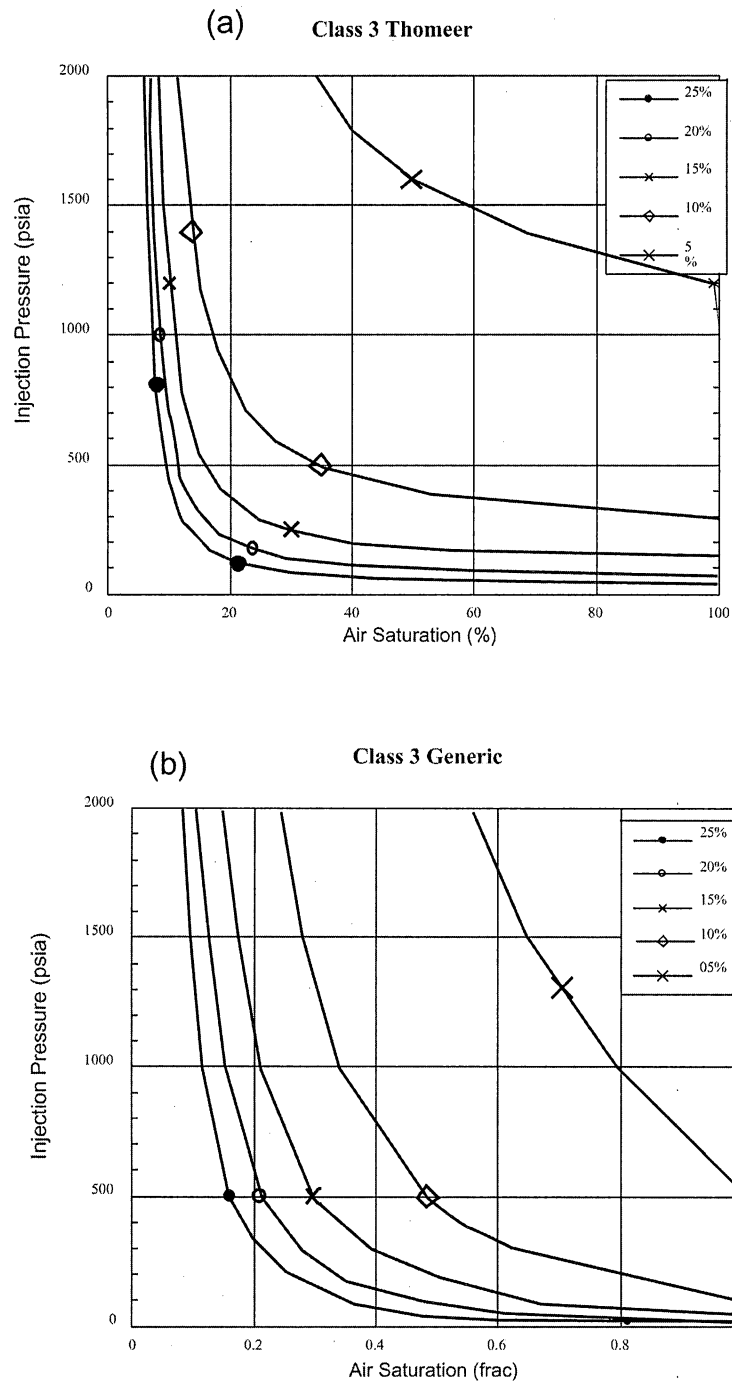
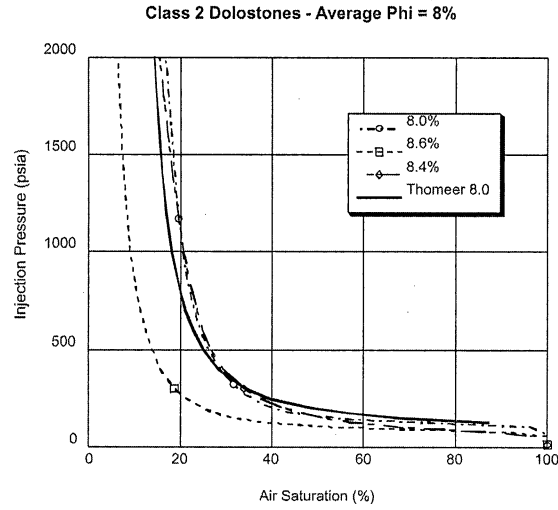
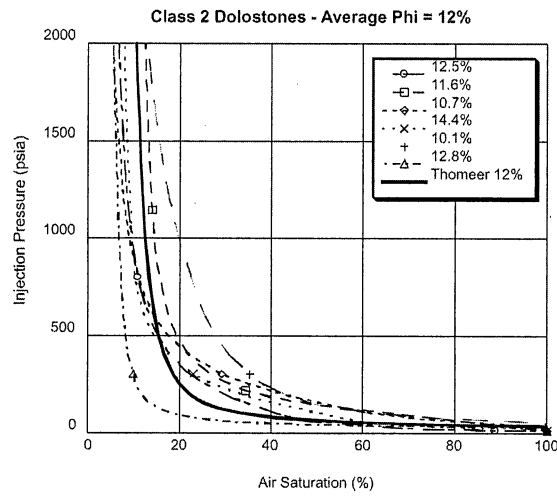


Figure 11. Comparison of (a) Thomeer class 3 capillary pressure model with (b) generic class 3 model.

(a)



(b)



(c)

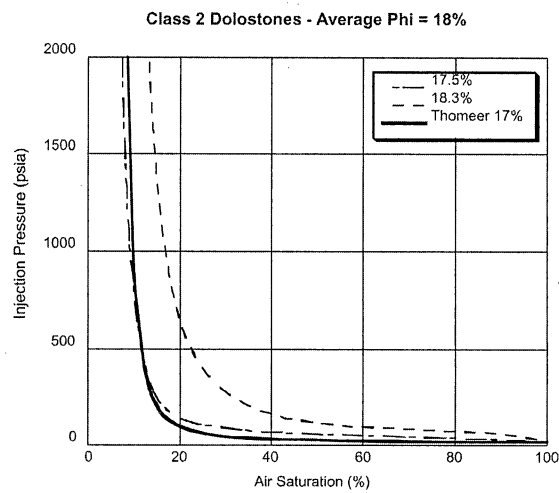


Figure 12. Comparison of class 2 curves with curves calculated using the Thomeer model. (a) Porosity average 8 percent, (b) porosity average 12 percent, (c) porosity average 18 percent.

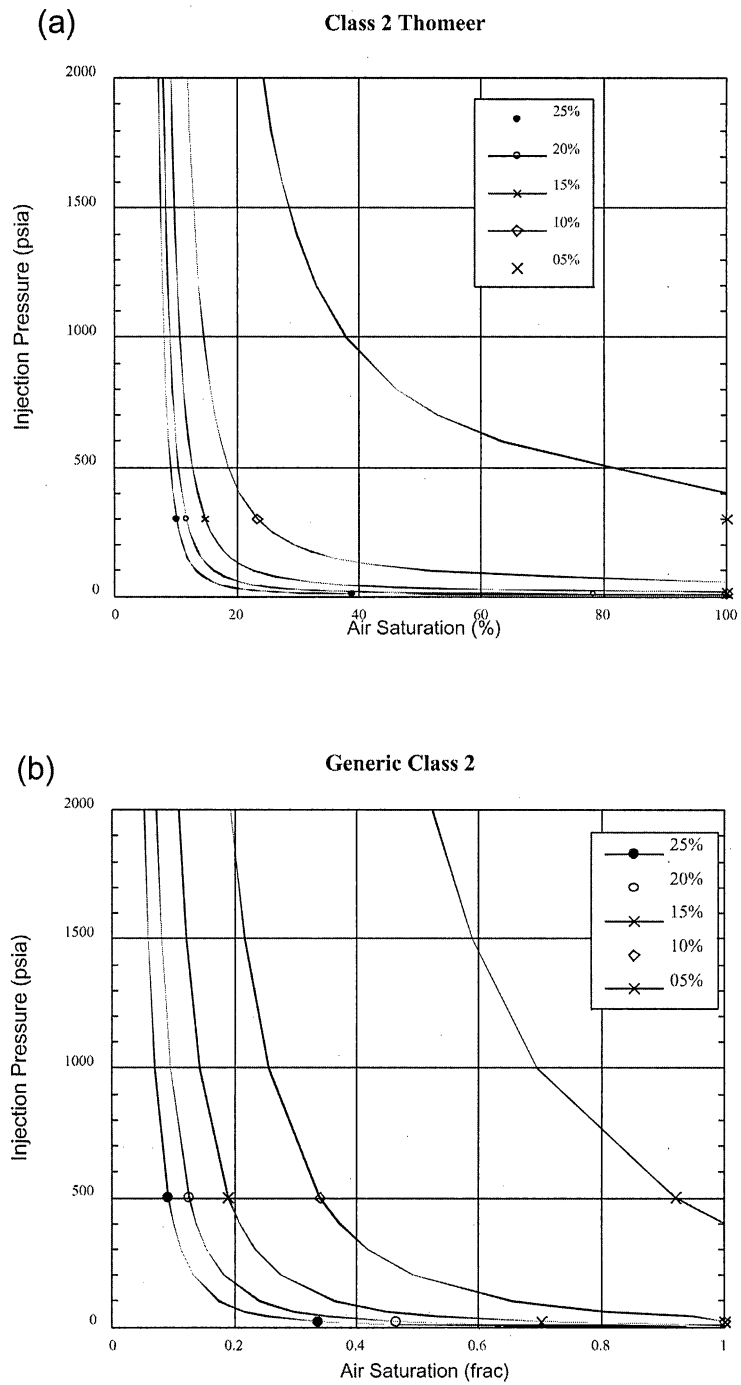


Figure 13. Comparison of (a) Thomeer class 2 capillary pressure model with (b) generic class 2 model.

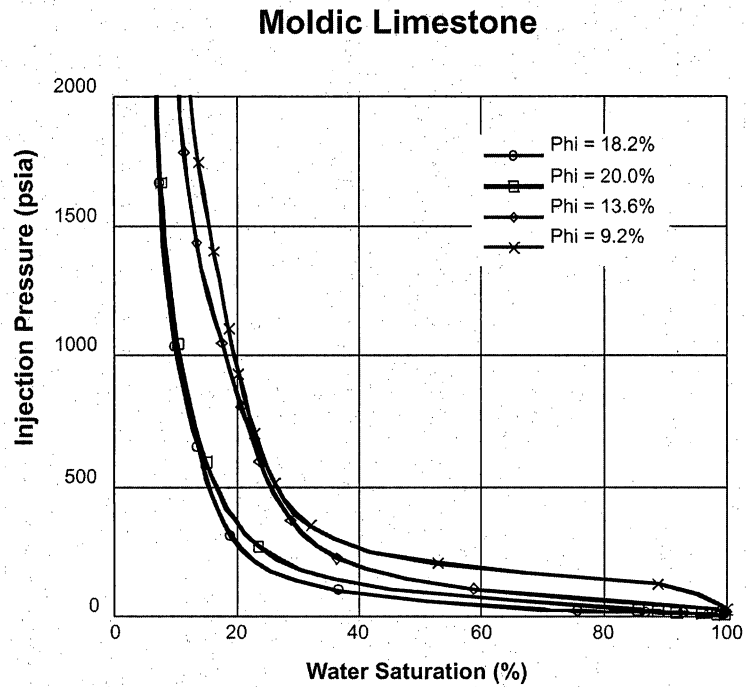


Figure 14. Capillary pressure curves from moldic limestone.

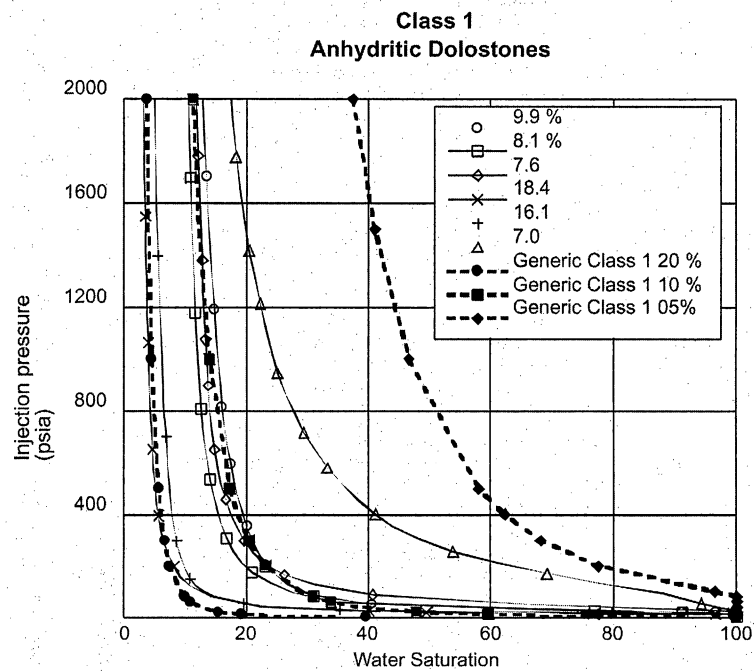


Figure 15. Comparison of capillary pressure curves from class 1 anhydritic dolostones with curves using the generic class 1 model.

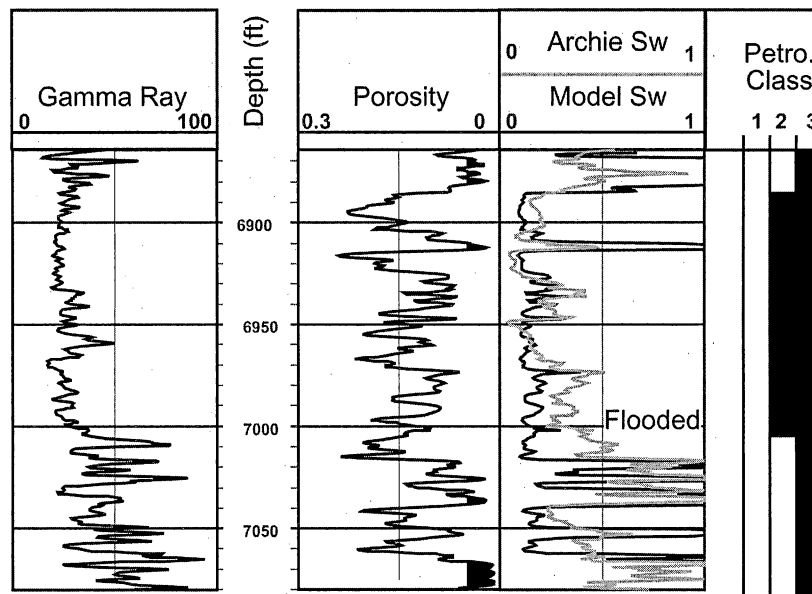


Figure 16. Example of model and Archie S_w from well FCU 5727.

**RESERVOIR MODELING AND SIMULATION OF FULLERTON
CLEAR FORK FIELD, ANDREWS COUNTY, TEXAS**

Fred Wang and F. Jerry Lucia

**Bureau of Economic Geology
Scott W. Tinker, Director
John A. and Katherine G. Jackson School of Geosciences
The University of Texas at Austin
Austin, Texas 78713-8924**

ABSTRACT.....	225
INTRODUCTION	226
3-D RESERVOIR MODELING.....	227
Stratigraphic Modeling	227
Upscaling	229
Petrophysical Modeling	230
Porosity Distribution.....	231
Permeability (k) and kh Distribution	232
S _w and S _o φh Distribution.....	234
VOLUMETRICS	235
Sensitivity Analysis	236
Search Radius in Mapping.....	236
Grid Resolution.....	237
Water-Oil Contact.....	237
Porosity Cutoffs	238
Water Saturation Cutoffs	239
Permeability Cutoffs	239
Compound Effects of Vertical Resolution and Cutoff Values	240
PRODUCTION-TREND ANALYSIS	242
FLOW-UNIT MODEL AND RESERVOIR SIMULATION	243
Flow-unit Model.....	243
Flow Simulation	249
Sensitivity Study.....	250
SUMMARY	253
REFERENCES	256
APPENDIX A: UPSCALING	295

Tables

1. Geologic and reservoir parameters of Fullerton Clear Fork Unit.....	257
2. Geologic frameworks used in 3-D reservoir models.....	258
3. Dimensions of 3-D field models.....	259
4. Formation volume factor, oil-gas ratio, and WOC used in OOIP estimates	259
5. Effect of variable search radius on OOIP estimates of FCU.....	259
6. Effect of water-oil contact on OOIP estimates of FCU.....	260
7. Effect of cutoff values on OOIP	260
8. Effect of cutoff values on OOIP in FCU for WOC at -3940 ft summarized by ExxonMobil zonation	261
9. Effect of cutoff values on OOIP in Fullerton field for WOC at -3940 ft summarized by ExxonMobil zonation	261
10. Effect of cutoff values on OOIP in FCU for WOC at -3940 ft summarized by high- frequency cycles	262
11. Effect of cutoff values on OOIP in Fullerton Clear Fork field for WOC at -3940 ft summarized by high-frequency cycles	263
12. Effect of vertical resolution on OOIP.....	264
13. Summary of parameters affecting OOIP	264
14. Dimensions of 3-D models of initial 2,000-acre model (simulation area).....	264

Figures

1. Production history of waterflooding in Fullerton Clear Fork Unit.....	265
2. Workflow of 3-D modeling	265
3. Geologic framework used to build 3-D models of Fullerton Clear Fork field.....	266
4. Effect of search radius of 2,500 ft and 5,000 ft on porosity mapping.....	266
5. Porosity distribution in fine-grid model	267
6. Average porosity distribution in Zone 1, Zone 2, Wichita, Zone 3, Zone 3B, and Zone 4	267
7. ϕ_h distribution in reservoir Zone 1 (Lower Clear Fork HFS 2.2) by cycle.....	268
8. Porosity distribution in reservoir Zone 1 (Lower Clear Fork. HFS 2.2) by cycle.....	268

9. Porosity distribution in reservoir Zone 2 (Lower Clear Fork. HFS 2.1) by cycle.....	268
10. Porosity distribution in Zones Wichita, 3, 3B, and 4, in the Wichita Formation	269
11. Permeability distribution in 3-D model.....	269
12. Permeability distribution in reservoir zones 1, 2, Wichita, 3, 3B, and 4.....	270
13. Kh distributions in Zone 1, Zone 2, Wichita, Zone 3, Zone 3B, and Zone 4.....	270
14. Results of petrophysical analysis in FCU 5927, 1284, and 1435	271
15. Water saturation distribution in 3-D model with oil-water contact at –3,940 ft	271
16. Water saturation distributions in Zone 1, Zone 2, Wichita, Zone 3, Zone 3B, and Zone 4	272
17. Hydrocarbon volume distributions in Zone 1, Zone 2, Wichita, Zone 3, Zone 3B, and Zone 4	272
18. Hydrocarbon volume distribution in six reservoir zones	273
19. Hydrocarbon volume distribution in Zone 1 (Lower Clear Fork HFS L 2.2)	273
20. Hydrocarbon volume distribution in Zone 2 (Lower Clear Fork HFS 2 L 2.1)	273
21. Hydrocarbon volume distribution in the Wichita Formation	274
22. Formation volume factor and oil-gas ratio of two types of crude in FCU	274
23. Effect of water-oil contact on vertical coverage in Zone 3B, Zone 4, and Zone 5 (Abo).....	275
24. Effect of water-oil contact on areal coverage in Zone 3, Zone 3B, Zone 4, and Zone 5 (Abo)	275
25. Effect of water-oil contacts on OOIP estimate.....	276
26. Effects of porosity cutoffs of 3%, 5% and 10%, and permeability cutoffs of 0.1, 0.5, and 1 mD on volumetrics	276
27. Effects of cutoff values on OOIP estimate porosity, water saturation, and permeability	277
28. Relationship between permeability and porosity cutoff values.....	277
29. Effects of porosity cutoffs and grid vertical resolution on volumetrics, 3%, 5%, and 10% on fine-grid model, and 3%, 5% and 10% on cycle-based model	278
30. Effects of porosity cutoffs and grid vertical resolution on volumetrics, 0.1, 0.5, and 1.0 mD on fine-grid model, and 0.1, 0.5, and 1.0 mD on cycle-based model.....	279
31. Changes in OOIP between high-resolution and cycle-based models with respect to porosity cutoff, water saturation cutoff, and permeability cutoff values	279

32. Production data and trends in primary and waterflooding	280
33. Initial 3:1 line-drive waterflooding pattern	280
34. Porosity and $S_{o\phi}$ in Zone 2, Wichita, and Zone 3, overlaid with production trends.....	281
35. Water-injection patterns in the initial reservoir model area in 2001	281
36. Production data and trends in primary and waterflooding in simulation area.....	282
37. Lawyer Canyon cycle 1 flow-layer model	283
38. Average porosity for various rock fabrics in sequences L2.1 and L2.2	284
39. Flow layers and cycles in sequence L2.1	285
40. Flow layers in sequence L2.2	286
41. Flow layers in the Wichita.....	287
42. Lower Clear Fork and Wichita flow layers in cored wells of simulation area illustrating the use of porosity to build a flow model.....	288
43. Porosity distribution in the simulation area.....	288
44. Permeability distribution in the simulation area.....	289
45. Water saturation distribution in the simulation area.....	289
46. Porosity and $S_{o\phi}$ trends in the simulation area.....	290
47. Porosity distribution in simulation model	290
48. Initial oil saturation in simulation model.....	291
49. Simulated oil saturation in 1960, 1970, 1980, and 2002, simulation area	291
50. Simulated oil saturation in 2002, in Zone 1	292
51. Simulated oil saturation in 2002, in selected model layer slices of the Lower Clear Fork HFS L2.1 (reservoir Zone 2).....	292
52. Simulated oil saturation in 2002, in upper model layers of the Wichita	293
53. Simulated oil saturation in 2002, in model layers of Wichita reservoir Zone 3B	293
54. Corey correlations for relative permeability.....	293
55. Effect of relative permeability on simulated oil rate, water rate, pressure, and oil recovery	294
56. Effect of permeability multiplication on simulated water production.....	294

Reservoir Modeling and Simulation of Fullerton Clear Fork Field, Andrews County, Texas

Fred Wang and F. Jerry Lucia

ABSTRACT

Fullerton Clear Fork field in Andrews County, West Texas, discovered in 1942, produces from lower Clear Fork, Wichita and Abo carbonates. The reservoir consists of tidal-flat to subtidal dolomite and limestone. The field was unitized in 1953, and waterflood began in 1960. Production peaked in 1986 at 15,000 bopd and declined sharply to 6,000 bopd in 2001 (fig. 1). Cumulative oil production from the field had reached 289 million barrels (MMbbl) as of July 2004.

3-D reservoir modeling and simulation studies were carried out in an integrated geologic, petrophysical, and geophysical study to address various issues on data, production, modeling, and simulation. Two 3-D reservoir models, a 2,000-acre window model, and a full-field model were built using a cycle-based geologic framework and rock-fabric-dependent petrophysical properties. Reservoir simulation was performed in a 1,600-acre area in a small-window model. A comprehensive sensitivity study on volumetrics was conducted using the full-field model.

Fullerton Clear Fork field is a highly heterogeneous reservoir with complex lithology and porosity controlled by diagenetic overprints. Porosity is better developed in the mud-dominated inner-ramp Wichita Formation than in the subtidal Lower Clear Fork Formation. Although ϕ_h is higher in the Wichita, k_h is greater in the Lower Clear Fork because of differing rock fabrics.

The simulation study was divided into two phases: (1) sensitivity analysis and (2) history matching. From the sensitivity study we could rank importance of reservoir parameters affecting production performance. In simulation, oil relative permeability for primary recovery has a strong effect on recovery from waterflooding. Because fractures and breccias are common in testing and core data, negative skin factors (or effective well-bore radii) were used to simulate near-well-bore fractures, and permeability values in the Lower Wichita were modified to simulate karst-related breccias. Through history matching, optimal fluid and rock properties were determined.

INTRODUCTION

Fullerton Clear Fork field in Andrews County, West Texas, discovered in 1942, produces 42° API crude from Lower Clear Fork and Wichita carbonates (table 1). The reservoir consists of tidal-flat to subtidal dolomite and limestone (see Ruppel and Jones, this volume, for a detailed description of the geology and mineralogy of the field). The field was unitized in 1953, and waterflood began in 1960. Production peaked in 1986 at 15,000 bopd and declined sharply to 6,000 bopd in 2001 (fig. 1). Cumulative oil production from the field had reached 289 million barrels (MMbbl) as of July 2004.

This report describes data and methodologies used in constructing geologic and flow models. Issues on geologic framework, petrophysical properties, water-oil contact, volumetrics, and upscaling are discussed. The objectives of 3-D modeling are to detect discrepancies among geologic, petrophysical, and engineering data; to build geologically realistic reservoir models; to establish criteria for volumetric estimations; to explore techniques of upscaling; to identify critical issues and parameters controlling production and injection fluid flow; and to develop strategies for reservoir management and

production enhancement. 3-D modeling is, therefore, an iterative process (fig. 2), which integrates geologic, petrophysical, and geophysical and engineering data and improves consistencies among these data.

3-D RESERVOIR MODELING

Geological, petrophysical, geophysical, and engineering data were used to build 3-D geologic and flow models. Two models were built for the field. The first encompasses an area of about 2,000 acres in the north-central part of the field (fig. 3a). This area, sometimes referred to as the Phase-I Study Area, was selected for initial detailed, integrated, geologic, petrophysical, and engineering characterization of the field because it includes the highest density of cores and best suites of wireline logs in the field. The second model includes the entire Fullerton Clear Fork Unit (fig. 3a). For both models, RMS software from Roxar and Gocad software from Earthscience Division were used for model construction. The 2,000-acre model includes 140 wells, whereas the full-field model includes a total of 730 wells out of the 1,250 wells in the unit.

Stratigraphic Modeling

Oil has been recovered from three formations—Lower Clear Fork, Wichita, and Abo. Core and outcrop data (see Ruppel and Jones, this report) show that the depositional setting changed from prograding subtidal during Abo deposition to aggradational peritidal during the Wichita deposition then to aggradation to progradation subtidal during Lower Clear Fork deposition. Ruppel and Jones (this report) discussed depositional and diagenetic history of the field, the controls over porosity development, and the methods used to construct the reservoir framework in detail.

The geologic framework used in the construction of the two 3-D models differed only slightly. For the initial 2,000-acre model, three high-frequency cycles (table 2) were defined and used to subdivide the Lower Clear Fork HFS 2.1 (Zone 1) reservoir section. Later, during full-field characterization, it was found that this part of the section was better characterized as having eight high-frequency cycles.

The full-field 3-D model was constructed using 36 stratigraphic horizons (table 2) and wireline-log data from 730 wells using good-quality data (fig. 3a). The horizons were correlated and mapped on the basis of well picks guided by the conceptual geological model and seismic data. Twenty-five high-frequency cycle tops (table 2) were identified in cores and correlated using wireline logs from the Lower Clear Fork (Zone 1) to the top of the Abo. Cycle tops were ultimately picked and correlated in a total of about 1,000 wells to improve layer interpolation and limit model boundary effects. Only 730 wells, however, were actually used to distribute petrophysical data.

From outcrop and seismic data, the Abo is recognized to be a west-east-prograding outer-ramp succession (Ruppel and Jones, this report). However, because only scattered core data are available and limited deep wells were drilled to the Abo Formation, detailed core and log correlations necessary to accurately model the true architecture of the Abo are unavailable. Instead, 11 horizons (table 2) were arbitrarily defined on the basis of the probable geological architecture of the Abo (according to outcrop and seismic data), mapped, and were then used to create a conceptual prograding-wedge model. Figure 2b shows 9 of the 11 horizons used to build the Abo unit.

Two 3-D-model software packages (RMS from ROXAR and GOCAD from Earthscience Division) were used to build the full-field geological model. Petrophysical properties of porosity, permeability, and initial water saturation were derived from wireline-log data for 730 selected wells. These data were converted from the standard LAS format into RMS well format to load into both packages. Two 3-D models, a high-resolution fine-grid model and a cycle-based model were built. The models contained grid cells of 242 (150 ft) in x direction, 432 (150 ft) in y direction, and 380 layers in fine-grid model and 35 layers in cycle-based model. Total numbers of cell in the full-field models are about 42 millions in the fine-grid model and 3.7 millions in the cycle-based model (table 3). The reservoir architecture built into the 3-D model (fig. 3c) shows prograding wedges in the Abo unit.

Upscaling

One of the most important and controversial issues in 3D petrophysical modeling is upscaling. Upscaling occurs in several levels during 3D modeling such as upscaling wireline log data to high-resolution grid and upscaling high-resolution grid into coarse grid for seismic-data guided modeling and reservoir simulation. Because upscaling has significant effects on volumetric estimates and permeability, the vertical resolution of 3D model and the method used for permeability scaleup need to be decided before petrophysical modeling.

Because the assumption of random distribution in porosity and permeability is only valid for limited reservoirs and geologic scales, meaning and utility of statistical averages can be confusing and sometimes misleading. This can be illustrated by the permeability average in vertical direction. Permeability average in vertical direction is

normally calculated by arithmetic average, geometric average and k - ϕ correlations. Because differences in these averages can be significant, especially when models are used for reservoir simulation, we conducted a detailed study on permeability upscaling using five two-layer models with seventy cases. The detailed petrophysical properties of two layer models and results are discussed in Appendix A.

Table A.1 lists the parameters used in fourteen cases of a two-layer model (figure A.1), layer 1 is a 2-ft layer with porosity (20%) and permeability (70.06 mD), and layer 2 is a 5-ft layer with varying porosities and permeabilities. According the theory of fluid flow through porous media, average permeability of these models are the arithmetic means. Results in table A.2 and fig. A.2 show that geometric means tend to underestimate average permeabilities, and difference between arithmetic mean and geometric mean increases with the permeability contrast between the two layers. This difference can be in an order of magnitude or higher in highly heterogeneous, stratified systems. Note that permeabilities in stratified systems do not follow k - ϕ correlations derived from core data. Permeabilities in most 3D models with vertical scales greater than scales of log and core data are commonly controlled by large-scale features such as stratifications, stacking patterns, permeability contrasts among strata, fractures, *etc.*, and are much higher than those calculated from geometric mean and k - ϕ correlations.

Petrophysical Modeling

Petrophysical properties of rock fabric, porosity, permeability, and water saturation from 730 selected wells were calculated (Kane, this report; Lucia and Kane, this report) and loaded into ROXAR and Gocad. Petrophysical properties were first upscaled to grid resolution of 3-D models and mapped using the inverse-distance

technique with search radii of 2,500 and 5,000 ft. Figure 4 shows porosity distributions in two layers, with search radii of 2,500 and 5,000 ft. Because in the west and south parts of the unit (circled areas in fig. 4) most wells are old with poor log quality, spacing of wells selected is sparse, and a search radius of 2,500 ft leaves many areas unmapped, we widened the search radius to 5,000 ft to increase mapping coverage.

Porosity Distribution

Porosity and ϕ_h distributions in Fullerton Clear Fork field (figs. 5, 6 and 7) are a complex function of facies, rock fabric, lithology, and diagenesis overprints. Figures 5 through 10 suggest that this reservoir is highly heterogeneous, both laterally and vertically. Porosity patterns and flow barriers can be recognized by cycle, zone, and area. The unit is conventionally divided into north- and south-dome areas and the north dome can be further divided into east and west sub-regions. Overall, porosity is best developed in the Lower Clear Fork (ExxonMobil Zone 2) and in the Wichita (ExxonMobil Zones Wichita [W] and 3B).

Figures 6a and 8 show that porosity in Zone 1 (Lower Clear Fork l 2.2), a grain-rich subtidal interval, is higher in the south dome area than the north dome. In the north dome, porosity is better developed in two areas, a NW-SE-trending belt in the middle of the field and a narrow NS belt farther west (shown in fig. 8) in cycles L2220 to L2260. Porosity in Zone 1 is normally less than 10 percent.

Zone 2 reservoir (Lower Clear Fork HFS 2.1) is a grain-dominated subtidal unit. Porosity in Zone 2 (figs. 6b and 9) is higher than that in Zone 1. In the north dome, porosity is best developed in a NW-SE trend (outlined area), mostly in L2105 to 2140 cycles. Reservoir quality sharply decreases away from this high-porosity trend, and Zone-

2 porosity in most of the west part of the field is very low. Zone 2 is separated from Zone 1 by laterally extensive, low-permeability, tidal-flat cycles at the base of Zone 1 and the top of Zone 2 (between L2220 and L2150 in Figs. 8 and 9). No such continuous flow barriers exist between Zone 2 and the Wichita zone.

The Wichita at the Fullerton Clear Fork Unit (FCU), includes four operator-named zones: Wichita (Zone W), Zone 3, Zone 3B, and Zone 4. Essentially all of these rocks are mud-dominated, inner-ramp, tidal-flat facies. Generally speaking, porosity in the Wichita Zone-uppermost Wichita Formation (fig. 6) is significantly higher than that in Zone 1 (Lower Clear Fork HFS 2.2) and slightly higher than porosity in Zone 2 (Lower Clear Fork HFS 2.1). As shown in figure 10, porosity distributions in W1 and W2 cycles are similar to that in Zone 2. It is best developed in the east half of the north dome and decreases sharply to the south and west. Porosity is much more widely scattered in W4 and W5 cycles. W4 is generally a low-porosity interval over most of the north dome area. Porosity is generally high and evenly distributed in intervals W8 to W11 (Zone 3B). In the north part of the north dome, the Wichita Formation can be separated into two reservoir intervals (W1 to W3 and W8 to W12) by the tight W4 and W5 cycles. In the south half of the north dome, however, this barrier vanishes because W4 and W5 are much more porous.

Permeability (k) and kh Distribution

Lucia (1985) has shown that permeability, for a given porosity, can be an order of magnitude higher for a carbonate grainstone (Class I) than that for a mud-dominated rock (Class III). Therefore, permeability values are significantly lower in the mud-dominated, inner-ramp Wichita Formation than those in the Lower Clear Fork (fig. 11). Permeability

values were calculated from porosity and rock fabric (see Kane, this report; Lucia and others, this report, respectively, for details) and upscaled vertically to resolutions of the 3-D model using the arithmetic averaging technique before being mapped into 3-D space.

Figures 12 and 13 show permeability and kh distributions in operator reservoir Zones 1, 2, Wichita, 3, 3B, and 4. Because permeability and kh are better displayed in a logarithmic scale, special procedures were taken for generating these averaged permeability and kh maps in logarithmic scale. Permeability and kh in the fine-grid model were upscaled to a seven-layer zone model using arithmetic mean. Permeability and kh maps were generated on the logarithmic values of upscaled permeability and kh.

Average permeability and kh (figs. 12 and 13) in the Fullerton reservoir are significantly higher in the Lower Clear Fork Formation (reservoir Zones 1 and 2) than in the Wichita Formation (Zones Wichita, 3, 3B, and 4). With highest permeability and kh, Zone 2 (Lower Clear Fork HFS 2.1) has the highest waterflood recovery efficiency.

Anomalous water production has been reported from the Wichita. Although not predicted or explained by matrix porosity or permeability data, these observations may be due to the presence of zones of karst brecciation in the Wichita. Breccias and related fractures have been reported from reservoir Zones 3 and 3B in several cores in the field (see Ruppel and Jones, this report) and may be the cause of nonmatrix flow.

Alternatively, anomalous water production may be associated with fractures induced by high-pressure water injection, a common problem in high-porosity, low-permeability reservoir zones like the Wichita.

S_w and $S_o\phi$ Distribution

One of the petrophysical problems in FCU is that the resistivity log response to grain-dominated rock fabrics in Zone 1 (Lower Clear Fork HFS 2.2) and in the Abo are higher than expected, according to Archie equation calculations. As a result, water saturations derived from resistivity logs are very low. In other words, oil saturations derived from resistivity log data are too high for low-porosity rocks. Water saturation values derived from capillary-pressure data (Lucia and others, this report) are generally much higher than those derived from resistivity data (fig. 14). These observations suggest that water-saturation estimates from the Archie equation are not reliable when porosity is less than 5 percent. Figure 15 shows water-saturation distribution in the full-field 3-D model.

Figures 16 and 17 show water saturation and $S_o\phi$ distributions by reservoir zones. These plots reveal that the greatest volume (39 percent) of original-oil-saturated pore volume is in Lower Clear Fork HFS 2.1 (reservoir Zone 2). Although not apparent from figure 18, the Lower Clear Fork HFS 2.2 (reservoir Zone 1) is the second-richest oil reservoir zone in the field (among four Wichita reservoir zones), with 18 percent of the oil, and the Wichita with 42 percent of the oil.

Figures 19 through 21 show $S_o\phi$ distribution by cycle. Although 18 percent of the original oil in place (OOIP) was in Zone 1 (Lower Clear Fork HFS 2 L 2.2), it is not apparent in $S_o\phi$ maps, and most of the oil is in the south dome. Instead, highest hydrocarbon pore volumes are found in porosity belts in L2140, L2130, L2120, L2110, L2105, W1, and W5 cycles.

VOLUMETRICS

One of the purposes of 3-D geologic models is to provide an accurate and flexible way for making original-oil-in-place (OOIP) estimates. OOIP is calculated from 3-D models by

$$V_o = 0.1781 B_o \sum_{k=1}^{kk} \sum_{j=1}^{jj} \sum_{i=1}^{ii} A_{ijk} h_{ijk} \phi_{ijk} (1 - S_{w,ijk}) pay_{ijk} \quad (1)$$

where

- V_o : original oil in place (BSTB)
- B_o : formation volume factor (bbl/STB)
- A_{ijk} : area (ft²)
- h_{ijk} : thickness (ft)
- ϕ_{ijk} : porosity (fraction)
- $S_{w,ijk}$: water saturation (fraction)
- pay_{ijk} : pay flag, 0 or 1

Figure 22 shows two types of oil with formation volume factors of 1.615 and 1.36 documented in the reservoir (Exxon Field Study Group, 1973). The second type of oil was found in the Lower Wichita in the north dome area. Because areal and vertical coverage of the second oil type is not clearly determined and thought to be relatively small, a formation volume factor of 1.6 (table 4) was used in this study for the entire reservoir.

In Equation 1, the pay flag is determined by cutoff values. Major sources of error in volumetric estimations are wireline-log data (porosity and water saturation),

limitations of petrophysical models, water-oil contact, mapping parameters, and vertical resolution of 3D models.

Sensitivity Analysis

Cutoff values are used to reduce errors in wireline logs, to reduce uncertainties in petrophysical equations at low porosity intervals, to eliminate high water-bearing intervals, and to remove non-reservoir-quality rocks from averaging petrophysical properties such as permeability, water saturation, etc.

For mature hydrocarbon fields such as Fullerton Clear Fork field, many wells were drilled before the arrival of modern porosity and resistivity tools. Accordingly, accurate modern porosity logs are of limited availability, and OOIP estimates can thus vary significantly. A sensitivity analysis was performed to determine the most likely range of OOIP of Fullerton Clear Fork field and unit. Parameters studied include

- (1) search radius in mapping,
- (2) grid vertical resolution,
- (3) water-oil contact,
- (4) porosity,
- (5) water saturation, and
- (6) permeability.

Search Radius in Mapping

As discussed in the petrophysical property section, search radius affects OOIP estimates by controlling the smoothness and coverage of petrophysical properties. In areas with close well spacing, a small search radius will not leave significant acreages unmapped (fig. 4). On the other hand, in areas or intervals with wide spacings and, thus,

high uncertainties, large search radii will overestimate OOIP. As shown in table 5, increasing the search radius from 2,500 to 5,000 ft resulted in 5- to 15-percent increases in OOIP. The largest (15 percent) increase in OOIP was in the Abo, where well control is scarce. With high uncertainties in the Abo, a search radius of 2,500 ft could reduce the risk of making too-optimistic predictions.

Grid Resolution

The vertical resolution of the 3-D model also has a significant impact on OOIP estimates. The optimal vertical resolution of the 3-D model needs to be determined as the coarsest resolution of the 3-D model with the least effect on OOIP estimate. We tested the effect of vertical resolution of 3-D models on OOIP using a zone-based model, a cycle-based model, and a 380-layer, fine-grid model. The calculated OOIP values are 1.19, 1.405, and 1.582 BSTB for zone-base, coarse-grid cycle-base, and fine-grid cycle-base models, respectively. The 20-percent difference in OOIP suggests that fine-grid models are necessary for OOIP calculations.

Water-Oil Contact

Similar to those for Zone 1 Lower Clear Fork HFS 2.2, resistivity values in the Abo are consistently high. This high resistivity is caused by the low water salinity. These high resistivity values, in turn, result in calculations of lower initial water saturations than are estimated from capillary-pressure data. They also make it difficult to determine true water-oil contact (WOC) from wireline-log data. Accordingly, four water-oil contacts (-3,940, -4,000, -4,050, and -4,100 ft) were tested to study the effect of WOC on OOIP. The -3,940 ft WOC is the shallowest reported in previous studies (by the operator). A WOC of -4,100 ft was used in this study to estimate original water saturation from

capillary curves. This value is supported by core saturation data in a downdip core in the field (Amoco FM-1). OOIP values (total pore volume) range from 1.582 BSTB for the WOC case at -3,940 ft to 1.917 BSTB for the WOC case at -4,100 ft (tables 6).

Figures 23 and 24 show vertical and area coverages of Wichita Zones 3B and 4 and the Abo (Zone 5). In the case of the WOC at -4,100 ft, the Abo (Zone 5) is included in the hydrocarbon volume calculations. A WOC of -3,940 ft reduces hydrocarbon volumes about 13 percent in Zone 3B and 46 percent in Zone 4 and eliminates almost all oil in the Abo (figs. 23 through 25). The main difference in OOIP among these cases is OOIP in the Abo unit. With a WOC at -4,100 ft, estimated OOIP in the Abo is 236 MMSTB. Because wells completed in the Abo unit are limited and the salinity of formation water in Abo is much lower than that in lower Clear Fork and Wichita, porosity and water saturation cannot be properly estimated as well as mapped, and uncertainty in this OOIP estimate in Abo is thus high.

Porosity Cutoffs

Four porosity cutoff values were studied: 3, 5, 7, and 10 percent. Fig. 26.a to c shows effects of porosity cutoffs of 3, 5 and 10 percent on volumetrics on 380-layer fine-grid and cycle-based models. Table 7 lists OOIP estimates in the unit and model areas for WOC at -3,940 and -4,100 ft. In unit and model areas at WOC of -3940 ft, detailed OOIP estimates by ExxonMobil zonations (tables 8 and 9) and by high-frequency cycles (tables 10 and 11) are also listed. In figure 27a, OOIP is plotted against the porosity cutoff value. The OOIP value decreases gradually with porosity cutoff values from 0 to 5%, and the rate of decrease increases sharply when the porosity cutoff value is greater than 5%.

It is important to understand that the porosity cutoff value should vary with rock fabric. For a specific porosity value, water saturation is lower in grain-dominated fabrics than in mud-dominated fabrics. Therefore, porosity cutoff values for the Lower Clear Fork should be lower than that for the Wichita. Instead of using porosity, water saturation and permeability can be used to resolve this rock-fabric-dependent issue.

Water Saturation Cutoffs

Water saturation is another commonly used parameter for cutoff in OOIP estimates. The purposes of water saturation cutoff are to remove errors and uncertainties in porosity, resistivity, and water saturation models in low-porosity intervals and to remove nonproductive, high-water-saturation transition-zone intervals. OOIP estimates for WOC at -3,940 and -4,100 ft in the unit and model areas are listed in tables 7-11. Results for the unit with a WOC at -3,940 ft are plotted in figure 27b. OOIP values increase with water saturation cutoff from 0.84 BSTB at 50 percent to 1.4 BSTB. OOIP value is pessimistically reduced when a 50-percent water saturation cutoff is used. Although intervals with less than 50-percent oil saturation can be considered nonproductive for waterflooding, oil in these intervals is part of the OOIP. The trade-off is that the recovery factor increases with decreasing OOIP.

Permeability Cutoffs

Three permeability cutoff values were calculated: 0.1, 0.5, and 1 mD. As shown in figure 28, the equivalent porosity cutoff values for Classes I, II, and III rocks are 0.055, 0.07, and 0.09, when 0.1-mD permeability is used; 0.065, 0.09, and 0.12, when 0.5 mD permeability is used; and 0.07, 0.10, and 0.14, when 1.0 mD permeability is used. Permeability cutoffs provide an easy way to determine rock-fabric-dependent porosity

cutoff values. This is clearly shown in figure 26.c with 10% porosity cutoff and figure 26.f with 1-mD permeability cutoff. Most of the low-porosity, high-permeability Zone 1 excluded by 10% porosity cutoff (fig. 26.c) is kept by 1-mD permeability cutoff (fig. 26.f), and vice versa for the high-porosity, low-permeability Wichita.

OOIP values for the entire Fullerton Clear Fork Unit at a WOC of –3,940 ft are 1.537, 1.342, and 1.139 billion barrels (Bbbl) for 0.1, 0.5, and 1.0 mD permeability cutoff values (table 7). Detailed OOIP estimates by ExxonMobil zonations and high-frequency cycles are listed in tables 8-11. Figure 27c shows that OOIP estimates decrease with permeability cutoff value linearly. The selection of permeability cutoff value is field-specific, depending on rock and fluid properties and operation considerations.

Compound Effects of Vertical Resolution and Cutoff Values

Discussed in the section of grid resolution, when no cutoff was applied the OOIP estimate decreases from 1.582 BSTB in the 380-layer high-resolution model to 1.405 BSTB in the cycle-based model. Since petrophysical properties are smoothed with the increase of vertical resolution of 3D grid, effects of cutoff values on OOIP are expected to vary significantly with the vertical resolution. This hypothesis is studied in details using a simple ten-layer model. Shown in figure A.3, this 10-layer model was upscaled into a two-layer flowunit model, and subsequently into a single-layer model. Fig. A.4 reveals that at 5% porosity cutoff volumetric estimate from the single-layer model is higher than the 10-layer model, and volumetric estimate is lowest from two-layer model. This simple example shows that the compound effects of grid vertical resolution and cutoffs on OOIP are complex and unpredictable. Hence, the same cutoff values used for the high-resolution model were performed on a coarser cycle-based model (table 3).

Figures 29 and 30 show changes in porosity and permeability coverages at Row 350 in fine-grid and cycle-based models with cutoffs. Most thin porosity and permeability layers in the fine-grid model are either excluded or averaged into thicker layers. Table 12 compares OOIP values calculated from high-resolution fine-grid and cycle-based model for porosity cutoffs from 0.0 to 10%, water saturation cutoffs from 50% to 100% and permeability cutoffs from 0 to 1 mD. The percent change in OOIP (5th column in table 12) was calculated by the difference in OOIP between high-resolution and cycle-based model divided by the OOIP from the high-resolution model. In figure 31, percent changes in OOIP are plotted with respect to porosity, water saturation and permeability cutoffs. The effect of vertical resolution on OOIP varies significantly with the cutoff criteria. Changes in OOIP between two models increase from 11 to 30 percent with the increase in porosity cutoff from 0 to 0.1 and with the decrease in water saturation cutoff from 100 to 50% but decrease slightly from 11 to 8% with the increase in permeability cutoff from 0.1 to 1 mD. The change in OOIP is highly sensitive to porosity and water saturation cutoffs but not sensitive to the permeability cutoff because arithmetic-mean permeabilities in stratified reservoirs are higher than those calculated from k - ϕ correlations and not very sensitive to grid vertical resolution (discussed in Appendix A). This special advantage in stability makes permeability a better cutoff parameter than porosity and water saturation.

Among parameters studied, vertical grid resolution and WOC have much greater effects on OOIP than search radius and areal coverage (table 13), and high-resolution models should be use for volumetric calculations.

PRODUCTION-TREND ANALYSIS

3-D modeling is an iterative process involving analyses of geology, geophysics, petrophysics, production data, and volumetrics calculations (fig. 2). Problems with geological or structural interpretations are normally detected during the construction of static models. Problems in petrophysical properties in well logs and static models can be identified using production data, production trends, and volumetrics.

Primary- and waterflood-recovery data are shown as bubbles in figure 32. During primary recovery, production from the north-dome area (outlined by three ellipsoids) was significantly higher than in other parts of the field and was generally highest along a NNW-SSE trend (fig. 32a).

Oil recovery from waterflooding has been complicated by the use of widely varying injection patterns through time and episodes of infill drilling. Waterflood operations have been dominated by an early 3:1 line-drive pattern (fig. 32). Oil recovery from such a pattern is expected to be higher at wells in the middle row (red circles in fig. 33) than wells in the other two rows that are closer to injectors (green circles in fig. 33). Four 3:1 line-drive patterns (colored boxes in fig. 32b) were created in the north-dome area during the initial phase of waterflooding (fig. 32b). The expected higher recovery from the middle row of producers was observed in the three 3:1 line-drive patterns in the east (outlined by the orange, green, and purple boxes in fig. 32b), but not in the pattern in the west (outlined by the blue box in fig. 32b).

Figure 34 shows the porosity and $S_o\phi_h$ maps in Zone 2, Wichita, and Zone 3 overlaid with production trends. The high-production areas during primary and waterflooding coincide well with the high porosity and $S_o\phi_h$ trends. Best productions

from the nose- area stem from the fact that it has highest S_{oph} values in all three zones. The drastic changes in petrophysical properties to the west have complicated recovery from patterned waterflooding (blue-colored polygon in fig. 34). The waterflooding recovery in this area decreases to the west.

FLOW-UNIT MODEL AND RESERVOIR SIMULATION

To develop an early understanding of the geology and petrophysics, a 2,000-acre area (fig. 35), containing the highest density of cores and best suites of wireline logs, was selected for detailed, integrated, geologic, petrophysical, and simulation study. After more than forty year waterflooding and extensive infill drillings, the area is currently under complex waterflooding patterns with 10 to 20-ac spacing (fig. 35). Reservoir simulation was performed on a 1600-ac area (red outlined box in fig. 35). Bubble maps of primary and waterflooding recoveries (fig. 36) shows that oil production from the east has been significantly higher than the west area. Because study in this reservoir simulation area was performed in the initial phase of the project, geologic framework, petrophysical models and methods used in 3D modeling were slightly different from those used in full-field models, and results of this study are only briefly discussed here.

Flow-unit Model

Distributing petrophysical properties within a geologic model is one of the most difficult tasks in building a simulation model. In this study, as well as in other reservoir studies done at the Bureau of Economic Geology, the basic geological framework within which the properties are distributed is the high-frequency cycle (HFC). Outcrop studies, however, have shown a systematic layering of petrophysical properties within the HFC related to the vertical succession of rock fabrics (Kerans and others, 1994, Lucia and

others, 1995). HFC's tend to show an upward increase in carbonate grains resulting in an ideal vertical succession from mud-dominated fabrics (mudstone, wackestone, mud-dominated packstone) to grain-dominated packstone and grainstone. Each fabric tends to form a geologic bed, and each fabric has a specific porosity-permeability transform. Therefore, each rock-fabric bed should be defined as a layer within the HFC. If this condition is not satisfied low permeability layers will be averaged with high permeability layers and the basic heterogeneity of the system will be compromised.

Values for porosity, permeability, and initial water saturation are calculated from wireline logs and provide the basic data used to populate the geologic model. There are numerous statistical methods for filling the interwell space with the calculated properties. Whatever method is used it must be constrained by the rock-fabric flow layers in order to preserve the petrophysical heterogeneity. The rock-fabric approach to distributing petrophysical properties is illustrated by outcrop results (fig. 37) (Lucia and others, 1992, Lucia, 1999). At Lawyer Canyon, Guadalupe Mountains, New Mexico, a single HFC has been mapped for 2700 ft along an outcrop and about 2000 permeability measurements made. Statistical analysis of the permeability data shows 1) a significant difference between the average permeability in the upper grainstone and the lower mud-dominated fabrics and 2) little or no spatial correlation of the permeability values within a rock-fabric layer, in this case the grainstone layer (Jennings and others, 2000). The implications are that only rock-fabric layers can be correlated between wells, not petrophysical properties, and that petrophysical properties should be statistically distributed within rock-fabric layers, not within HFC's.

In this study the HFC's are correlated using porosity logs calibrated to core descriptions (Ruppel and Jones, this volume). Cycles within the Lower Clear Fork sequences L2.2 and L2.1 are defined by an upward increase in graininess. Wichita cycles are composed of mud-dominated fabrics and are typically capped by tidal-flat fabrics. The cycles are typically dolostone but limestone may be present at the cycle base (Ruppel and Jones, this volume).

The grainy top of the Lower Clear Fork HFC's tend to be more porous than the muddy base, which is true for both limestones and dolostones. As pointed out by Ruppel and Jones in this volume, much of the core-log calibration was done by comparing core descriptions with porosity logs. The calibration can also be done by comparing thin section descriptions with porosity measurements when the thin sections are taken directly from the core plugs. An analysis of rock fabrics and porosity using data from sequences L2.2 and L2.1 (fig. 38) shows that, for dolostones, grain-dominated packstones average 11.5% porosity, mud-dominated packstones 9.4%, and wackestones and mudstones 4.9%. For limestones, grainstones average 14.9% porosity, grain-dominated packstones 8.2%, mud-dominated packstones 7.6%, and wackestone and mudstones 7.0%. Although there is significant overlap in the porosity ranges, there is a clear increase in porosity with increasing graininess in the dolostones. In the limestones the grainstones (moldic grainstones) are clearly more porous than other fabrics. The lime grain-dominated packstones have an average porosity similar to the mud-dominated fabrics. This result may be related to difficulties in distinguishing between grain- and mud-dominated fabrics. The distinction often becomes a matter of judgment by the observer as to whether or not the inter-grain volume is completely or partially filled with mud.

For simplicity, the HFC's are divided into two rock-fabric flow layers, a lower low porosity layer and an upper high porosity layer. In the Lower Clear Fork sequences L2.1 and L2.2, the porosity changes are used as a surrogate for a lower mud-dominated fabric and an upper grain-dominated fabric. Because there is considerable overlap of porosity values for each fabric, a single porosity value can not be used to separate rock fabrics. Instead, the vertical porosity profile must be used and a judgment made as to where a significant change in rock fabric is likely to occur. Seven HFC are defined in sequence L2.1 each with two flow layers except for cycle 2105, which did not appear to have a low to high porosity profile in the simulation area (fig. 39). The cycle types correlate quite well with porosity, grain-dominated fabrics, and tidal flat facies but not with lithology. In most cycles the distinction between low porosity and high porosity is quite clear. The upper two cycles are class 3 fine crystalline dolostones and the porosity is too low to be productive. Three HFC's were originally defined in sequence L2.2 and are illustrated in figure 40. The cycles were defined based on limestone upward-shoaling successions found in the core from well 6122, and were difficult to pick in the dolostone wells because of low porosity values. As such, the flow layers in this sequence are somewhat arbitrary. Sequence L2.2 was later divided into eight HFC based on core descriptions outside of the simulation area (see Ruppel and Jones, this volume). The simulation model has six flow layers whereas the full field model has eight HFC. There is an imperfect match between the flow layers in the simulation model and the new HFC's (fig. 40). There has been no attempt to integrate the eight HFC into the simulation model.

In the Wichita there is no clear relationship between fabric and porosity because the cycles are typically composed of mud-dominated fabrics, either limestone of

dolostone. The limestones, however, have less than 3 percent porosity and are typically found at the base of the cycles that have porous dolostone tops. Many cycles have no limestone, however, and the upper intervals are more porous than the lower intervals. Ten HFC's were picked in the Wichita each with two flow layers (fig. 41). The upper cycles from W1-W5 typically have thin limestones at the base and are easily correlated throughout the simulation area. No cycles were picked between cycle W5 and W8 because the interval is composed of limestone and dolostone, typically has less the 10 percent porosity, and therefore is nonproductive. Cycles W8-W12 are based solely on the porosity profiles and have little relationship to tidal-flat capped cycles or lithology. Therefore, these cycles and flow layers are the most arbitrary of all the layers in the simulation model.

The importance of the flow layers is to preserve layers of high and low permeability (fig. 42). The individual cycles, however, are characterized by a single transform. The Wichita is characterized by a class 3 transform because it is typically a lime wackestone or fine crystalline dolowackestone. The Lower Clear Fork L2.1 sequence is characterized by a class 2 transform in the lower interval and a class 3 transform in the upper interval. The Lower Clear Fork L2.2 sequence is characterized by a class 1 transform. Therefore, the permeability contrast between the upper and lower flow layers is related the difference in porosity, not the difference in rock fabric. A more accurate permeability contrast could be obtained if the different limestone fabrics could be distinguished.

Out of a total of 140 wells in the model area, 85 (fig. 35) were initially selected for detailed geologic and petrophysical characterization. However, early 3-D models

based on these 85 wells revealed that tops of flowunit mapped using only these wells did not match well tops at unselected wells and that there were significant boundary-effect problems at the model's edges. To correct these problems, all wells in the study area and a line of wells immediately outside the study area were subsequently correlated and included, thus affecting the model.

A fine-scale geological model containing 3.165 million cells (table 14) was then constructed for the area, and porosity (from Kane, this report) was mapped through the 3-D space (fig. 43). The layers average 2.2 ft, and the cells are 100 ft square. Permeability and water saturation (figs. 44 and 45) were calculated from porosity on the basis of correlations provided by Lucia and others (this report). Rock-fabric-dependent permeability-porosity relationships are shown in figure 28. The rock-fabric-based water-saturation-porosity relationships used in this 2,000-acre model were the generic relationships, not the new Thomeer model described by Lucia and Kane (this report).

Porosity and $S_o\phi h$ maps (fig. 46) show that reservoir quality is poor in Zone 1 except the northwest corner, is good in the central and southeastern areas in Zone 2 where primary recovery was higher, and increases to the south in Wichita. Careful examination of figures 43 and 44 shows that although ϕh in the model area is higher in the Wichita, kh is greater in the Lower Clear Fork. This is due to the very different rock fabrics in each. Note that oil saturation (fig. 45) is highest in the Lower Clear Fork, again owing to the presence of better quality rock fabrics in this part of the reservoir (see Lucia and Kane, this report).

Following construction of the fine-scale reservoir model, the model was scaled up to the flow-unit thickness for reservoir simulation. The flow-unit model contains 136,656

cells (73 by 48 by 39). Again, porosity was averaged arithmetically, and permeability and water saturation were calculated using correlations to porosity and rock fabric (figs. 47 and 48). In figure 47, the reservoir appears highly compartmentalized in both lateral and vertical directions, because only cells with porosity values greater than 6 percent are shown.

Flow Simulation

The simulation study was divided into two phases: (1) sensitivity analysis and (2) history matching. From the sensitivity study, it is possible to rank the importance of reservoir parameters affecting production performance.

Figure 49 displays simulated oil-saturation distributions in 1960, 1970, 1980, and 2002. Water injection was initiated in 1960. The blue areas in the 1960 image represent high gas saturation. As water injection progressed, water displaced oil from the injectors into these high-gas-saturation areas, as seen in 1970 and 1980 images.

Figure 50 shows simulated oil-saturation distributions in 2002 in two layers of the Lower Clear Fork HGS L2.2 (reservoir Zone 1). Because Zone 1 is a heterogeneous, locally low permeability interval, reservoir continuities between injectors and producers are poor, and sweep efficiency during waterflooding has been low.

The model shows that the Lower Clear Fork HFS L2.1 (reservoir Zone 2) contains the highest ϕ , k , and oil in place. The area of highest porosity trends through the east part of model area (fig. 50); however, reservoir continuity in this area is somewhat limited, as revealed by the presence of many small areas of very low oil saturation. Simulated oil-saturation distributions in 2002 at layers 11, 13, 15, and 17 (fig. 51) indicate that many areas have not been swept by water.

In the model area, porosity and reservoir continuity are best developed in Wichita cycles W1 to W3. Simulated oil-saturation distributions (fig. 52) in 2002 at layers 20 and 22 (upper flow units in W1 and W2) indicate that W1 and W2 have been fully swept except for the southeasternmost corner of the model area, where the W2 zone is not perforated in wells 1331, 1333, 1431, or 1433.

Wichita Formation reservoir Zone 3, which includes model layers W4 and W5, exhibits very low permeability in the model area. This low-permeability interval separates porosity and oil saturation in the uppermost Wichita (layers W1 and W2) from relatively high porosity, permeability, and oil saturation in Wichita Zone 3B.

Simulated oil-saturation distributions in year 2002 in model layers 30 and 32 (fig. 53) indicate that Wichita layers W8 and W9 (operator reservoir Zone 3B) have been well swept in areas where wells have been perforated. The southeasternmost corner of the model area, however, has not been flooded because many injectors (wells 1326, 1334, 1430, 1432, and 1434) have not been perforated.

Sensitivity Study

The reservoir flow model was used for history matching of production data of the simulation window (shown in fig. 35). History matching was complicated by (1) lack of reliable primary production data, (2) gas injection, (3) upscaling, (3) relative permeability, and (4) karst breccias and fractures.

Because permeabilities in the simulation model was calculated from k - ϕ correlation from porosity which could underestimate cell permeabilities significantly (discussed in Appendix A), permeability data was increased five to thirty folds during history matching. In addition, relative permeability and ratio of k_{vh} , two of the most

dominating factors affecting oil recovery from reservoir simulation, need to be optimized through history matching.

There are six relative permeabilities for gas, oil, and water phases in drainage and imbibition processes. This raises the question as to what the most critical relative permeability is. A good matching on primary recovery is essential for good matches on secondary and tertiary recoveries. A sensitivity study of oil relative permeability for primary recovery was performed by changing Corey's exponent of oil curve from 2 to 5. Fig. 54 shows that oil and water relative permeabilities decrease with the increase in Corey exponent. The bold curves are oil and water relative permeabilities suggested by ExxonMobil FCU team.

Figures 55a through d show effects of oil relative permeability data on matching oil rate, water rate, pressure and oil recovery. Note that oil permeability had no significant effects on oil and water production during primary recovery from 1942 through 1960 but strong effects on production and pressure data during waterflooding. The effect of oil permeability in primary recovery is on pressure rather than oil. Using oil relative permeability curves with Corey exponents of 2.2 and 3 oil production and pressure histories during waterflooding can be matched reasonably well, but water production history cannot. On the other hand, Using oil relative permeability curves with Corey exponents of 4 and 5, simulation runs match water production history during waterflooding but miss oil production and pressure histories significantly.

Because pressure test data measure pressures in connected pores and simulations calculate average pressures of all pores, simulated pressures should be higher than

measured field pressures. Measured field pressures can be corrected by the fraction of connected oil volume over total oil volume using

$$\Delta P = \Delta P_m \frac{V_{o_conn}}{V_o} = \Delta P_m \frac{V_{o_MB}}{V_o} \quad (2)$$

$$P_i - \bar{P} = (P_i - P_m) \frac{V_{o_MB}}{V_o} \quad (2a)$$

$$\bar{P} = P_i - (P_i - P_m) \frac{V_{o_MB}}{V_o} \quad (2b)$$

Where

ΔP : corrected pressure change, psi,

ΔP_m : measured pressure change, psi,

P_i : initial pressure, psia,

\bar{P} : average pressure, psia,

P_m : measured pressure, psia,

V_{o_conn} , V_{o_MB} : connected oil volume (bbl) from material balance,

V_o : total oil volume (bbl).

One of the difficulties in this simulation was to match water production and injection rates. Both water production and injection from the area were found to be significantly higher than those simulated on the basis of matrix permeability in the static model. Nonmatrix flow has been indicated by negative skin factors from -3 to -5 in well-testing data, anomalous water production, and breccias reported from reservoir Zones 3 and 3B in several cores in the field (see Ruppel and Jones, this report). In addition, near-well-bore fractures might have been induced by high-pressure water injection. Hence,

negative skin factors of -3 (or effective well-bore radii) were used to simulate near-well-bore fractures, and permeability values in the Lower Wichita were modified to simulate karst-related breccias. Two simulation runs were performed by increasing permeability values in the Lower Wichita (Zone 3B) by factors of 25 and 30. Figure 55 compares results of these simulations with cumulative water production of the area (crosses in figure 55). Without permeability modification, simulated water production (the black curve in fig. 55) is significantly lower than the field data (crosses). Two cases with increasing permeability values in Zone 3B by a factor of 25 (green curve) and 30 (purple curve) significantly improve the matches between simulated water productions to the field data. Both cases tend to overestimate water production during the early stage of waterflooding from 1960 through 1985.

Simulation results provide an important glimpse into reservoir response in West Texas Clear Fork carbonate reservoirs. Both techniques were used to construct model and results and can serve as a basis for improved modeling and simulation of other shallow-water carbonate-platform reservoirs.

SUMMARY

Fullerton Clear Fork field is a highly heterogeneous reservoir with complex lithology and porosity trends controlled by diagenetic overprints. Porosity is better developed in the mud-dominated inner-ramp Wichita Formation than the subtidal Lower Clear Fork Formation. Although ϕ_h is higher in the Wichita, hydrocarbon volume and kh are greater in the Lower Clear Fork because of differing rock fabrics.

In Zone 1, reservoir continuity and quality are best in the south dome area and generally poor in the north dome, with scattered, local porosity developments. With the

highest hydrocarbon pore volume, and good ϕ and k_h , the high-porosity trends in Zone 2 in the Lower Clear Fork and Zone W in the Upper Wichita are the best units in Fullerton Clear Fork field. Reservoir quality decreases sharply away from these porosity trends.

Zone 3 (W4 and W5) is tight in the north half of the north dome and becomes porous in the south half of the north dome and the south dome. Zone 3B is a more homogeneous unit, with high porosity and continuity. However, karst-related breccias and fractures have complicated production and injection in Zone 3B.

Because OOIP and permeability distribution are functions of vertical resolution, high-resolution static model should be built as the base geological model.

For stratified reservoirs, arithmetic means rather than geometric means should be used in permeability scaling because it is based on the theory of single phase fluid flow through porous media. Geometric means tend to underestimate permeabilities by an order of magnitude or more in highly heterogeneous, stratified reservoirs.

Permeability values in large-scale stratified reservoirs are higher than those derived from permeability-porosity correlations from core data because permeability values in 3D models are controlled by large-scale features such as stratification, stacking patterns, permeability contrasts, fractures, *etc.*

Original oil in place (OOIP) is a complex function of log-data quality, mapping parameters, vertical resolution of the 3-D grid, water-oil contact, and cutoff values in porosity, permeability, and water saturation. Permeability and water saturation are equivalent to rock-fabric-dependent porosity cutoffs.

Using a simple 10-layer test model (in Appendix A), we showed that the compound effects of grid vertical resolution and cutoffs are complicated. Volumetrics from high-resolution models are more realistic but not always higher than that from coarse models.

High-vertical-resolution 3-D models should be used in volumetric calculation. OOIP estimate depends strongly on the selection of cutoff values. With WOC at -3,940 ft, the estimated OOIP is 1.58 BSTB without using any cutoff, 1.32 BSTB with a 5-percent porosity cutoff, 1.23 BSTB with a 0.5-mD permeability cutoff, and 1.32 BSTB with a 60-percent water saturation cutoff.

The 380-layer, high-resolution model, calculates higher OOIP than the 36-layer, cycle-based model by 8 to 30%, depending on cutoff criteria. Due to the unique nature of arithmetic mean in stratified reservoirs, permeability cutoffs are less sensitive to grid vertical resolution than porosity and water saturation cutoffs.

In simulation, oil relative permeability for primary recovery has a strong effect on recovery from waterflooding. Because pressure test data measure pressures among connected pores and simulated pressures calculate average pressures of all pores, simulated pressures should be higher than measured field pressures.

Because most high-permeability streaks were averaged out by upscaling, both oil and water relative permeabilities used in simulations were higher than those measured in the lab.

Because fractures and breccias are common in testing and core data, negative skin factors (or effective well-bore radii) were used to simulate near-well-bore fractures, and

permeability values in the Lower Wichita were modified to simulate karst-related breccias. Through history matching, optimal fluid and rock properties were determined.

Simulation results provide an important glimpse into reservoir response in West Texas Clear Fork carbonate reservoirs. Both the techniques used to construct the model and the results can serve as a basis for improved modeling and simulation of other shallow-water carbonate-platform reservoirs.

REFERENCES

- Exxon Company, 1973, Plan for depletion, Fullerton Clearfork Unit, Andrew County, Texas: Internal Report, Field Study Group, Production Department, Midcontinent Division, 70 p.
- Jennings, J. W., Ruppel, S. C., and Ward, W. B., 2000, Geostatistical analysis of permeability data and modeling of fluid-flow effect in carbonate outcrops: SPE Reservoir Evaluation and Engineering, v. 3, no. 4, p. 292–303.
- Kerans, C., Lucia, F. J., and Senger, R. K., 1994, Integrated characterization of carbonate ramp reservoirs using Permian San Andres Formation outcrop analogs: American Association of Petroleum Geologists Bulletin, v. 78, no. 2, p. 181–216.
- Lucia, F. J., 1999, Carbonate reservoir characterization: New York, Springer-Verlag, 226 p.
- Lucia, F. J., Kerans, Charles, and Senger, R. K., 1992, Defining flow units in dolomitized carbonate-ramp reservoirs: Society of Petroleum Engineers, Paper No. SPE 24702, p. 399–406.
- Lucia, F. J., Kerans, Charles, and Wang, F. P., 1995, Fluid-flow characterization of dolomitized carbonate-ramp reservoirs: San Andres Formation (Permian) of Seminole field and Algerita Escarpment, Permian Basin, Texas and New Mexico, *in* Stoudt, E. L., and Harris, P. M., eds., Hydrocarbon reservoir characterization: geologic framework and flow unit modeling: SEPM (Society for Sedimentary Geology), SEPM Short Course Notes, v. 34, p. 129–153.
- Railroad Commission of Texas, 1986, Docket No. 8-87,428: Hearing File, Texas Railroad Commission, May 1986.

Table 1. Geologic and reservoir parameters of Fullerton Clear Fork Unit (Modified from Docket No. 8-87,428, Texas Railroad Commission, 1986).

Parameter	Value
Reservoir	Clear Fork & Wichita-Albany
Discovery Date	December 1941
Unitization Date	1953
Structure Type	NW-SE-Trending Anticline
Rock Type	Dolomite/Limestone
Primary Drive Mechanism	Solution Gas
Secondary Recovery	Waterflood
Original Oil Productive Area	44,000 ac
Unit Area	29,541 ac
Reservoir Temperature	110°F
Porosity	10.6% ¹
Permeability	15 mD ¹
Water Salinity	90,000 ppm
API Oil Gravity	42° at 60°F
Oil Gravity	0.82
Oil Viscosity	0.43 cP at 110°F and 2940 psi
Original FVF	1.6 RB/STB
Gas Gravity	0.97
Original Reservoir Pressure	2,940 psi at 7200 ft 2,852 at -3950 ft
Original Saturation Pressure	2,370 psia
Original Solution GOR	1,250 SCF/STB
1986 Reservoir Pressure	3,100 psia
1986 Solution GOR	700 SCF/STB

¹Based on 6% porosity cutoff and 0.1-mD permeability cutoff.

Table 2. Geologic frameworks used in 3-D reservoir models.

Sequence	ExxonMobil Zones	Phase-I Study Model			Field Model	
		Horizon	Flow Unit	Subgrid No.	Cycle	Subgrid No.
Lower Clear Fork HFS 2.2	Zone 1	LC1	LC1	1	2300 (not included)	
			LC1a	2	2270	1
		LC2	LC2	3	2260	2
			LC2a	4	2250	3
		LC3	LC3	5	2240	4
			LC3a	6	2230	5
		LC 4	LC 4	7	2220	6
			LC4a	8	2210	7
		LC 5	LC 5	9	2200	8
			LC5a	10	2150	9
Lower Clear Fork HFS 2.1	Zone 2	LC 6	LC 6	11	2140	10
			LC6a	12		
		LC 7	LC 7	13	2130	11
			LC7a	14		
		LC 8	LC 8	15	2120	12
			LC8a	16		
		LC 9	LC 9	17	2110	13
			LC9a	18		
		LC 10	LC 10	19	2105	14
Wichita	Wichita	W1	W1	20	W1	15
			W1a	21		
		W2	W2	22	W2	16
			W2a	23		
	Zone 3	W3	W3	24	W3	17
			W3a	25		
		W4	W4	26	W4	18
			W4a	27		
		W5	W5	28	W5	19
			W5a	29		
	Zone3B	W8	W8	30	W8	20
			W8a	31		
		W9	W9	32	W9	21
			W9a	33		
		W10	W10	34	W10	22
			W10a	35		
	Zone 4	W11	W11	36	W11	23
			W11a	37		
		W12	W12	38	W12	24
			W12a	39		
ABO	Zone 5	ABO	Not included	Not included	ABO	25
					ABO10	26
					ABO9	27
					ABO8	28
					ABO7	29
					ABO6	30
					ABO5	31
					ABO4	32
					ABO3	33
					ABO2	34
					ABO1	35
					ABO1+100 ft	36

Table 3. Dimensions of 3-D field models.

Item Name	Fine-Grid Model		Cycle-Based Model	
	Dimension (ft)	No. of Cells	Dimension (ft)	No. of Cells
X	150	239	150	239
Y	150	462	150	462
Z		380		36
Total		42×10^6		3.7×10^6

Table 4. Formation volume factor, oil-gas ratio, and WOC used in OOIP estimates.

Parameter	Value	
Formation Volume Factor (bbl/STB)	1.6	
Gas-Oil Ratio (SCF/STB)	1,250	
Water-Oil Contact (ft)	ExxonMobil -3,940	This Study -4,100

Table 5. Effect of variable search radius on OOIP estimates of FCU.

	Search Radius (ft)	2500	5000
OOIP (BSTB)	Zone 1	0.2591	0.2791
	Zone 2	0.5744	0.5995
	Wichita	0.2114	0.2173
	Zone 3	0.2672	0.2779
	Zone 3B	0.2038	0.2164
	Zone 4	0.0777	0.0907
	Subtotal	1.5936	1.6810
	Zone 5 (ABO)	0.1969	0.2357
	Total	1.7905	1.9167

Table 6. Effect of water-oil contact on OOIP estimates of FCU.

		WOC (ft)			
		-3940	-4000	-4050	-4100
OOIP (BSTB)	Zone 1	0.2791	0.2791	0.2791	0.2791
	Zone 2	0.5991	0.5995	0.5995	0.5995
	Wichita	0.2108	0.2170	0.2173	0.2173
	Zone 3	0.2594	0.2746	0.2773	0.2779
	Zone 3B	0.1849	0.2063	0.2142	0.2164
	Zone 4	0.0485	0.0737	0.0824	0.0907
	Subtotal	0.7036	1.6501	1.6698	1.6810
	Zone 5 (ABO)	0.0002	0.0281	0.1048	0.2357
Total		1.5821	1.6783	1.7746	1.9167

Table 7. Effect of cutoff values on OOIP.

		OOIP (BSTB)			
		WOC at -3,940 ft		WOC at -4,100 ft Excluding ABO	
		Unit	Model	Unit	Model
	No Cutoff	1.582	1.694	1.681	1.796
Porosity	0.03	1.577	1.688	1.676	1.789
	0.05	1.514	1.614	1.612	1.715
	0.07	1.344	1.423	1.440	1.521
	0.10	0.998	1.044	1.084	1.132
Water Saturation	0.50	1.184	1.253	1.228	1.295
	0.60	1.329	1.406	1.378	1.460
	0.70	1.427	1.521	1.494	1.587
	0.80	1.505	1.608	1.584	1.686
Permeability (mD)	0.10	1.537	1.642	1.635	1.743
	0.50	1.342	1.434	1.433	1.528
	1.00	1.139	1.224	1.219	1.304

Table 8. Effect of cutoff values on OOIP in FCU for WOC at -3940 ft summarized by ExxonMobil zonation.

	Zone	Base Case	OOIP (BSTB)											
			Porosity Cutoff				Water Saturation Cutoff					Permeability Cutoff		
			0.03	0.05	0.07	0.10	0.5	0.6	0.7	0.8	0.9	0.1	0.5	1.0
Lower Clear Fork	Zone 1	0.279	0.277	0.245	0.157	0.048	0.212	0.240	0.259	0.270	0.277	0.264	0.229	0.205
	Zone 2	0.599	0.596	0.571	0.507	0.347	0.494	0.532	0.559	0.580	0.593	0.576	0.516	0.473
	Subtotal	0.878	0.874	0.817	0.664	0.395	0.706	0.772	0.818	0.850	0.870	0.840	0.744	0.678
Wichita	Wichita	0.211	0.210	0.208	0.202	0.176	0.163	0.179	0.191	0.201	0.207	0.207	0.175	0.138
	Zone 3	0.259	0.259	0.256	0.249	0.215	0.162	0.193	0.219	0.239	0.253	0.256	0.211	0.153
	Zone 3B	0.185	0.185	0.184	0.183	0.172	0.131	0.149	0.163	0.174	0.181	0.184	0.168	0.135
	Zone 4	0.049	0.049	0.048	0.047	0.041	0.022	0.029	0.035	0.042	0.046	0.048	0.043	0.035
	Subtotal	0.704	0.703	0.697	0.681	0.603	0.478	0.550	0.609	0.655	0.687	0.696	0.597	0.461
	Zone 1-4	1.582	1.576	1.514	1.344	0.997	1.184	1.323	1.427	1.505	1.557	1.536	1.341	1.139
Abo	Zone 5	0.000	0.000	0.000	0.000	0.000	0.000	0.000	0.000	0.000	0.000	0.000	0.000	0.000
Total		1.582	1.577	1.514	1.344	0.998	1.184	1.323	1.427	1.505	1.557	1.537	1.342	1.139

Table 9. Effect of cutoff values on OOIP in Fullerton field for WOC at -3940 ft summarized by ExxonMobil zonation.

	Zone	Base Case	OOIP (BSTB)											
			Porosity Cutoff				Water Saturation Cutoff					Permeability Cutoff		
			0.03	0.05	0.07	0.10	0.5	0.6	0.7	0.8	0.9	0.1	0.5	1.0
Lower Clear Fork	Zone 1	0.314	0.311	0.274	0.174	0.051	0.234	0.267	0.289	0.303	0.311	0.295	0.256	0.230
	Zone 2	0.647	0.643	0.613	0.542	0.371	0.526	0.568	0.600	0.623	0.639	0.621	0.556	0.511
	Subtotal	0.960	0.954	0.887	0.716	0.422	0.760	0.836	0.889	0.926	0.950	0.916	0.812	0.741
Wichita	Wichita	0.219	0.219	0.216	0.210	0.182	0.167	0.184	0.198	0.208	0.215	0.215	0.181	0.144
	Zone 3	0.272	0.271	0.268	0.259	0.222	0.167	0.200	0.227	0.249	0.264	0.268	0.220	0.161
	Zone 3B	0.188	0.188	0.187	0.186	0.174	0.132	0.150	0.165	0.176	0.184	0.187	0.171	0.137
	Zone 4	0.049	0.049	0.048	0.047	0.041	0.022	0.029	0.035	0.042	0.046	0.048	0.043	0.035
	Subtotal	0.727	0.726	0.720	0.702	0.619	0.488	0.564	0.626	0.675	0.709	0.719	0.615	0.477
	Zone 1-4	1.688	1.681	1.608	1.418	1.041	1.248	1.400	1.515	1.601	1.659	1.635	1.427	1.218
Abo	Zone 5	0.007	0.007	0.006	0.006	0.004	0.005	0.006	0.006	0.007	0.007	0.007	0.007	0.007
Total		1.694	1.688	1.614	1.423	1.044	1.253	1.406	1.521	1.608	1.666	1.642	1.434	1.224

Table 10. Effect of cutoff values on OOIP in FCU for WOC at -3940 ft summarized by high frequency cycles.

OOIP (BSTB) for WOC at -3940 in FCU															
Formation	Sequence	Cycle	Base Case	Porosity Cutoff				Water Saturation Cutoff					Permeability Cutoff		
				0.03	0.05	0.07	0.10	0.5	0.6	0.7	0.8	0.9	0.1	0.5	1.0
Lower Clear Fork	HSF L2.2	L2270	0.018	0.017	0.014	0.008	0.003	0.012	0.014	0.015	0.017	0.017	0.016	0.013	0.011
		L2260	0.033	0.032	0.029	0.019	0.005	0.026	0.029	0.031	0.032	0.032	0.031	0.027	0.024
		L2250	0.041	0.041	0.037	0.024	0.008	0.032	0.036	0.039	0.040	0.040	0.039	0.034	0.031
		L2240	0.058	0.058	0.054	0.037	0.012	0.048	0.053	0.056	0.058	0.058	0.057	0.051	0.046
		L2230	0.053	0.053	0.048	0.029	0.007	0.041	0.047	0.050	0.052	0.053	0.051	0.045	0.040
		L2220	0.044	0.043	0.037	0.022	0.006	0.031	0.036	0.040	0.042	0.043	0.040	0.034	0.030
		L2210	0.033	0.032	0.027	0.018	0.007	0.021	0.025	0.028	0.031	0.032	0.030	0.025	0.023
		Zone 1	0.279	0.277	0.245	0.157	0.048	0.212	0.240	0.259	0.270	0.277	0.264	0.229	0.205
	HFS L2.1	L2200	0.027	0.027	0.025	0.022	0.011	0.014	0.018	0.021	0.024	0.026	0.023	0.012	0.007
		L2150	0.025	0.025	0.023	0.019	0.009	0.013	0.016	0.019	0.021	0.024	0.020	0.010	0.007
		L2140	0.107	0.106	0.101	0.092	0.066	0.090	0.097	0.101	0.104	0.106	0.104	0.099	0.095
		L2130	0.123	0.122	0.117	0.105	0.077	0.106	0.112	0.117	0.120	0.122	0.120	0.114	0.107
		L2120	0.140	0.139	0.134	0.119	0.086	0.121	0.128	0.133	0.137	0.139	0.136	0.126	0.118
		L2110	0.097	0.096	0.092	0.080	0.049	0.082	0.088	0.092	0.094	0.096	0.093	0.083	0.073
		L2105	0.082	0.081	0.078	0.070	0.048	0.068	0.073	0.077	0.079	0.081	0.080	0.072	0.066
		Zone 2	0.599	0.596	0.571	0.507	0.347	0.494	0.532	0.559	0.580	0.593	0.576	0.516	0.473
Wichita	HFS L1	W1	0.098	0.098	0.097	0.095	0.087	0.083	0.088	0.092	0.095	0.097	0.096	0.088	0.078
		W2	0.055	0.055	0.054	0.053	0.045	0.041	0.046	0.050	0.052	0.054	0.054	0.044	0.032
		W3	0.058	0.057	0.057	0.054	0.044	0.039	0.045	0.050	0.054	0.056	0.057	0.043	0.028
		Wichita	0.211	0.210	0.208	0.202	0.176	0.163	0.179	0.191	0.201	0.207	0.207	0.175	0.138
		W4	0.063	0.063	0.062	0.059	0.049	0.040	0.047	0.053	0.058	0.062	0.062	0.049	0.034
		W5	0.196	0.196	0.194	0.189	0.166	0.122	0.146	0.165	0.181	0.191	0.194	0.162	0.118
		Zone 3	0.259	0.259	0.256	0.249	0.215	0.162	0.193	0.219	0.239	0.253	0.256	0.211	0.153
		W8	0.064	0.064	0.063	0.063	0.060	0.048	0.054	0.058	0.061	0.063	0.063	0.059	0.048
		W9	0.051	0.051	0.051	0.051	0.048	0.037	0.042	0.046	0.048	0.050	0.051	0.047	0.038
		W10	0.044	0.044	0.043	0.043	0.040	0.027	0.032	0.037	0.040	0.042	0.043	0.038	0.029
		W11	0.026	0.026	0.026	0.026	0.024	0.018	0.021	0.023	0.024	0.026	0.026	0.024	0.019
		Zone 3B	0.185	0.185	0.184	0.183	0.172	0.131	0.149	0.163	0.174	0.181	0.184	0.168	0.135
		W12	0.049	0.049	0.048	0.047	0.041	0.022	0.029	0.035	0.042	0.046	0.048	0.043	0.035
		Zone 4	0.049	0.049	0.048	0.047	0.041	0.022	0.029	0.035	0.042	0.046	0.048	0.043	0.035
LCF+W			1.582	1.576	1.514	1.344	0.997	1.184	1.323	1.427	1.505	1.557	1.536	1.341	1.139
Abo	Abo	Abo12	0.000	0.000	0.000	0.000	0.000	0.000	0.000	0.000	0.000	0.000	0.000	0.000	0.000
		Abo11	0.000	0.000	0.000	0.000	0.000	0.000	0.000	0.000	0.000	0.000	0.000	0.000	0.000
		Abo10	0.000	0.000	0.000	0.000	0.000	0.000	0.000	0.000	0.000	0.000	0.000	0.000	0.000
		Abo09	0.000	0.000	0.000	0.000	0.000	0.000	0.000	0.000	0.000	0.000	0.000	0.000	0.000
		Abo08	0.000	0.000	0.000	0.000	0.000	0.000	0.000	0.000	0.000	0.000	0.000	0.000	0.000
		Abo07	0.000	0.000	0.000	0.000	0.000	0.000	0.000	0.000	0.000	0.000	0.000	0.000	0.000
		Abo06	0.000	0.000	0.000	0.000	0.000	0.000	0.000	0.000	0.000	0.000	0.000	0.000	0.000
		Abo05	0.000	0.000	0.000	0.000	0.000	0.000	0.000	0.000	0.000	0.000	0.000	0.000	0.000
		Abo04	0.000	0.000	0.000	0.000	0.000	0.000	0.000	0.000	0.000	0.000	0.000	0.000	0.000
		Abo03	0.000	0.000	0.000	0.000	0.000	0.000	0.000	0.000	0.000	0.000	0.000	0.000	0.000
		Abo02	0.000	0.000	0.000	0.000	0.000	0.000	0.000	0.000	0.000	0.000	0.000	0.000	0.000
		Abo01	0.000	0.000	0.000	0.000	0.000	0.000	0.000	0.000	0.000	0.000	0.000	0.000	0.000
		Zone 5	0.000	0.000	0.000	0.000	0.000	0.000	0.000	0.000	0.000	0.000	0.000	0.000	0.000
Total			1.582	1.577	1.514	1.344	0.998	1.184	1.323	1.427	1.505	1.557	1.537	1.342	1.139

Table 11. Effect of cutoff values on OOIP in Fullerton Clear Fork field for WOC at -3940 ft summarized by high frequency cycles.

			OOIP (BSTB) for WOC at -3940 in Fullerton Clear Fork field												
Formation	Sequence	Cycle	Base Case	Porosity Cutoff				Water Saturation Cutoff					Permeability Cutoff		
				0.03	0.05	0.07	0.10	0.5	0.6	0.7	0.8	0.9	0.1	0.5	1.0
Lower Clear Fork	HSF L2.2	L2270	0.020	0.020	0.015	0.009	0.003	0.013	0.015	0.017	0.019	0.020	0.018	0.014	0.012
		L2260	0.035	0.034	0.030	0.019	0.005	0.027	0.030	0.032	0.034	0.034	0.033	0.028	0.025
		L2250	0.044	0.044	0.039	0.026	0.008	0.034	0.039	0.041	0.043	0.044	0.042	0.037	0.034
		L2240	0.066	0.065	0.060	0.041	0.013	0.054	0.059	0.063	0.064	0.065	0.063	0.057	0.052
		L2230	0.060	0.060	0.054	0.033	0.008	0.046	0.053	0.057	0.059	0.060	0.058	0.051	0.045
		L2220	0.050	0.050	0.043	0.025	0.007	0.036	0.041	0.046	0.048	0.049	0.046	0.039	0.035
		L2210	0.039	0.038	0.032	0.021	0.007	0.025	0.030	0.033	0.036	0.038	0.035	0.030	0.027
		Zone 1	0.314	0.311	0.274	0.174	0.051	0.234	0.267	0.289	0.303	0.311	0.295	0.256	0.230
	HFS L2.1	L2200	0.028	0.028	0.027	0.022	0.011	0.015	0.018	0.021	0.024	0.027	0.024	0.012	0.007
		L2150	0.027	0.026	0.025	0.019	0.009	0.013	0.017	0.020	0.023	0.025	0.022	0.011	0.008
		L2140	0.114	0.114	0.109	0.098	0.070	0.095	0.103	0.108	0.111	0.114	0.112	0.106	0.101
		L2130	0.138	0.137	0.131	0.118	0.087	0.119	0.125	0.130	0.134	0.136	0.134	0.127	0.121
		L2120	0.150	0.149	0.143	0.127	0.092	0.128	0.136	0.142	0.147	0.149	0.146	0.135	0.127
		L2110	0.104	0.103	0.099	0.086	0.052	0.086	0.093	0.098	0.101	0.103	0.100	0.089	0.079
		L2105	0.086	0.085	0.082	0.072	0.049	0.069	0.075	0.080	0.083	0.085	0.083	0.075	0.069
		Zone 2	0.647	0.643	0.613	0.542	0.371	0.526	0.568	0.600	0.623	0.639	0.621	0.556	0.511
Wichita	HFS L1	W1	0.103	0.103	0.102	0.100	0.091	0.086	0.092	0.097	0.100	0.102	0.102	0.093	0.083
		W2	0.056	0.056	0.055	0.053	0.046	0.041	0.046	0.050	0.053	0.055	0.055	0.045	0.032
		W3	0.060	0.060	0.059	0.056	0.045	0.040	0.046	0.051	0.055	0.058	0.059	0.044	0.029
		Wichita	0.219	0.219	0.216	0.210	0.182	0.167	0.184	0.198	0.208	0.215	0.215	0.181	0.144
		W4	0.066	0.066	0.064	0.061	0.050	0.040	0.048	0.055	0.060	0.064	0.065	0.050	0.034
		W5	0.206	0.205	0.204	0.198	0.173	0.127	0.152	0.173	0.189	0.200	0.204	0.170	0.127
		Zone 3	0.272	0.271	0.268	0.259	0.222	0.167	0.200	0.227	0.249	0.264	0.268	0.220	0.161
		W8	0.065	0.065	0.065	0.064	0.061	0.049	0.054	0.059	0.062	0.064	0.065	0.060	0.049
		W9	0.052	0.052	0.051	0.051	0.048	0.037	0.042	0.046	0.049	0.051	0.051	0.047	0.038
		W10	0.045	0.045	0.045	0.044	0.041	0.028	0.033	0.038	0.041	0.044	0.045	0.040	0.030
		W11	0.027	0.027	0.026	0.026	0.024	0.018	0.021	0.023	0.025	0.026	0.026	0.024	0.020
		Zone 3B	0.188	0.188	0.187	0.186	0.174	0.132	0.150	0.165	0.176	0.184	0.187	0.171	0.137
		W12	0.049	0.049	0.048	0.047	0.041	0.022	0.029	0.035	0.042	0.046	0.048	0.043	0.035
		Zone 4	0.049	0.049	0.048	0.047	0.041	0.022	0.029	0.035	0.042	0.046	0.048	0.043	0.035
		LCF+W	1.688	1.681	1.608	1.418	1.041	1.248	1.400	1.515	1.601	1.659	1.635	1.427	1.218
Abo	Abo	Abo12	0.004	0.004	0.004	0.003	0.002	0.003	0.003	0.004	0.004	0.004	0.004	0.004	0.004
		Abo11	0.003	0.003	0.003	0.002	0.001	0.002	0.002	0.003	0.003	0.003	0.003	0.003	0.003
		Abo10	0.000	0.000	0.000	0.000	0.000	0.000	0.000	0.000	0.000	0.000	0.000	0.000	0.000
		Abo09	0.000	0.000	0.000	0.000	0.000	0.000	0.000	0.000	0.000	0.000	0.000	0.000	0.000
		Abo08	0.000	0.000	0.000	0.000	0.000	0.000	0.000	0.000	0.000	0.000	0.000	0.000	0.000
		Abo07	0.000	0.000	0.000	0.000	0.000	0.000	0.000	0.000	0.000	0.000	0.000	0.000	0.000
		Abo06	0.000	0.000	0.000	0.000	0.000	0.000	0.000	0.000	0.000	0.000	0.000	0.000	0.000
		Abo05	0.000	0.000	0.000	0.000	0.000	0.000	0.000	0.000	0.000	0.000	0.000	0.000	0.000
		Abo04	0.000	0.000	0.000	0.000	0.000	0.000	0.000	0.000	0.000	0.000	0.000	0.000	0.000
		Abo03	0.000	0.000	0.000	0.000	0.000	0.000	0.000	0.000	0.000	0.000	0.000	0.000	0.000
		Abo02	0.000	0.000	0.000	0.000	0.000	0.000	0.000	0.000	0.000	0.000	0.000	0.000	0.000
		Abo01	0.000	0.000	0.000	0.000	0.000	0.000	0.000	0.000	0.000	0.000	0.000	0.000	0.000
		Zone 5	0.007	0.007	0.006	0.006	0.004	0.005	0.006	0.006	0.007	0.007	0.007	0.007	0.007
		Total			1.694	1.688	1.614	1.423	1.044	1.253	1.406	1.521	1.608	1.666	1.642

Table 12. Effect of vertical resolution on OOIP.

		OOIP (BSTB) WOC at -3,940 ft		
		Fine Grid	Cycle	Change (%)
No Cutoff		1.582	1.405	11.2
Porosity	0.03	1.577	1.398	11.4
	0.05	1.514	1.315	13.1
	0.07	1.344	1.124	16.4
	0.10	0.998	0.731	26.8
Water Saturation	0.50	1.184	0.843	28.8
	0.60	1.329	1.027	22.4
	0.70	1.427	1.177	17.5
	0.80	1.505	1.298	13.8
	0.90	1.557	1.376	11.6
Permeability (mD)	0.10	1.537	1.39	9.6
	0.50	1.342	1.23	8.3
	1.00	1.139	1.05	7.8

Table 13. Summary of parameters affecting OOIP.

Parameter	Change (%)
Search radius	4-7
Vertical resolution	8-29
Areal Coverage	6-10
Water-oil contact	
-3940 to -4100 ft	20-25
-3940 to top of Abo	4-6

Table 14. Dimensions of 3-D models of initial 2,000-acre model (simulation area).

Item Name	Fine-Grid Model		Simulation Model	
	Dimension (ft)	No. of Cells	Dimension (ft)	No. of Cells
X	103	140	200	73
Y	105	90	200	48
Z	2.2 (0-16)	254		39
Total		3.165×10^6		136,656

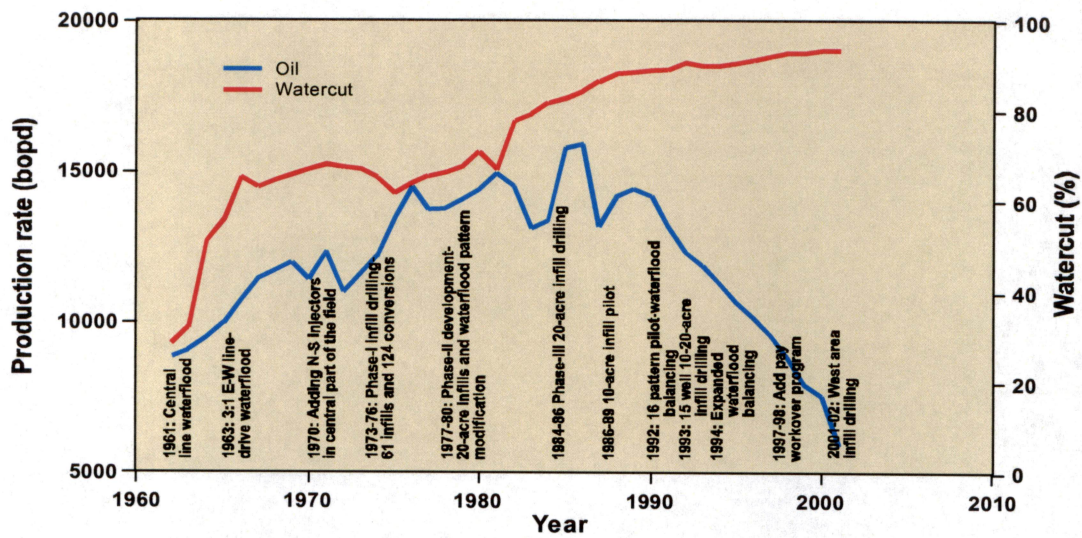


Figure 1. Production history of waterflooding in Fullerton Clear Fork Unit.

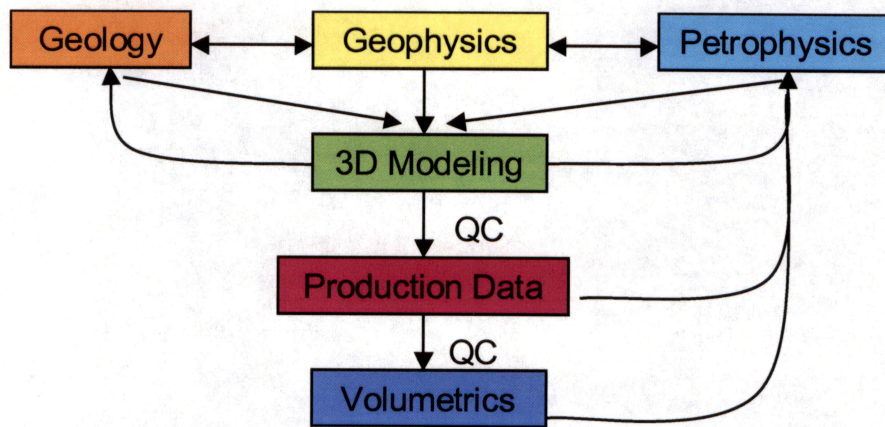


Figure 2. Workflow of 3-D modeling.

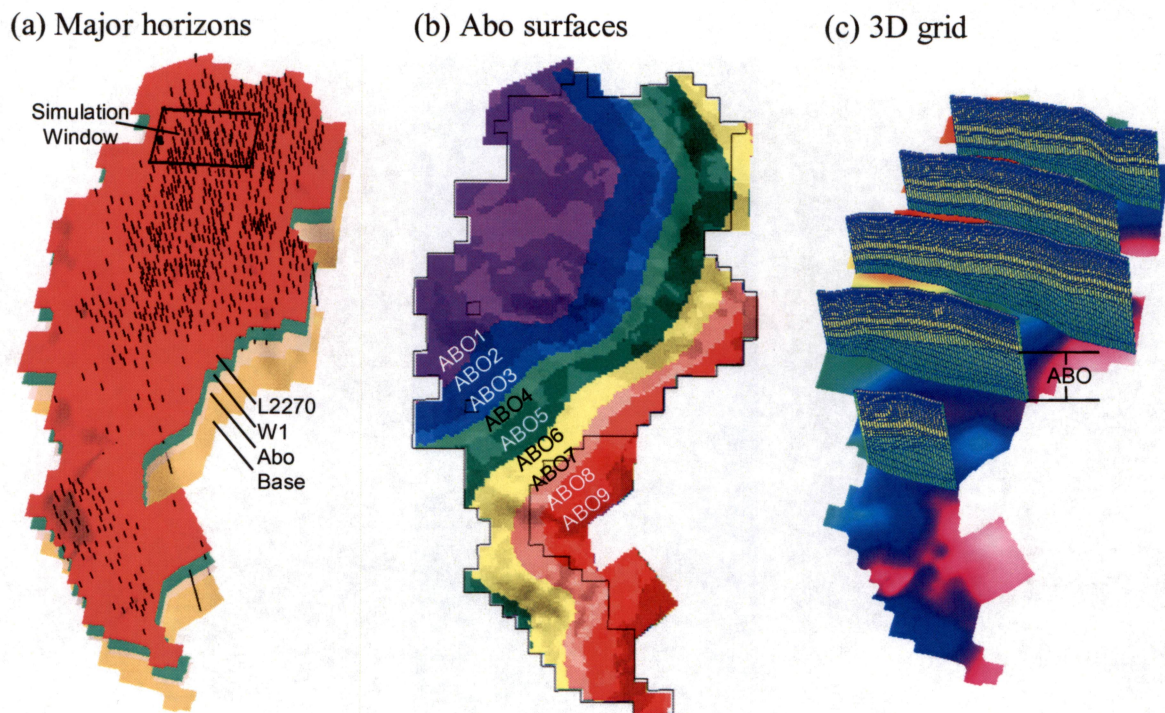


Figure 3. Geologic framework used to build 3-D models of Fullerton Clear Fork field. (a) four major horizons, 730 selected wells, and the simulation window; (b) 9 west-east prograding units used in building Abo model; and (c) sections of 3-D grids showing the prograding Abo unit.

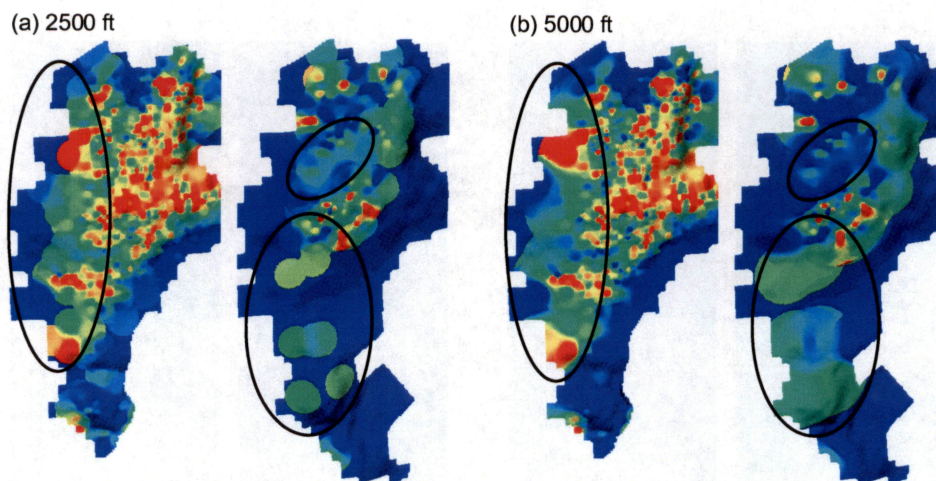


Figure 4. Effect of search radius of (a) 2,500 ft and (b) 5,000 ft on porosity mapping. Circled areas show that a search radius of 5,000 ft improves mapping coverages.

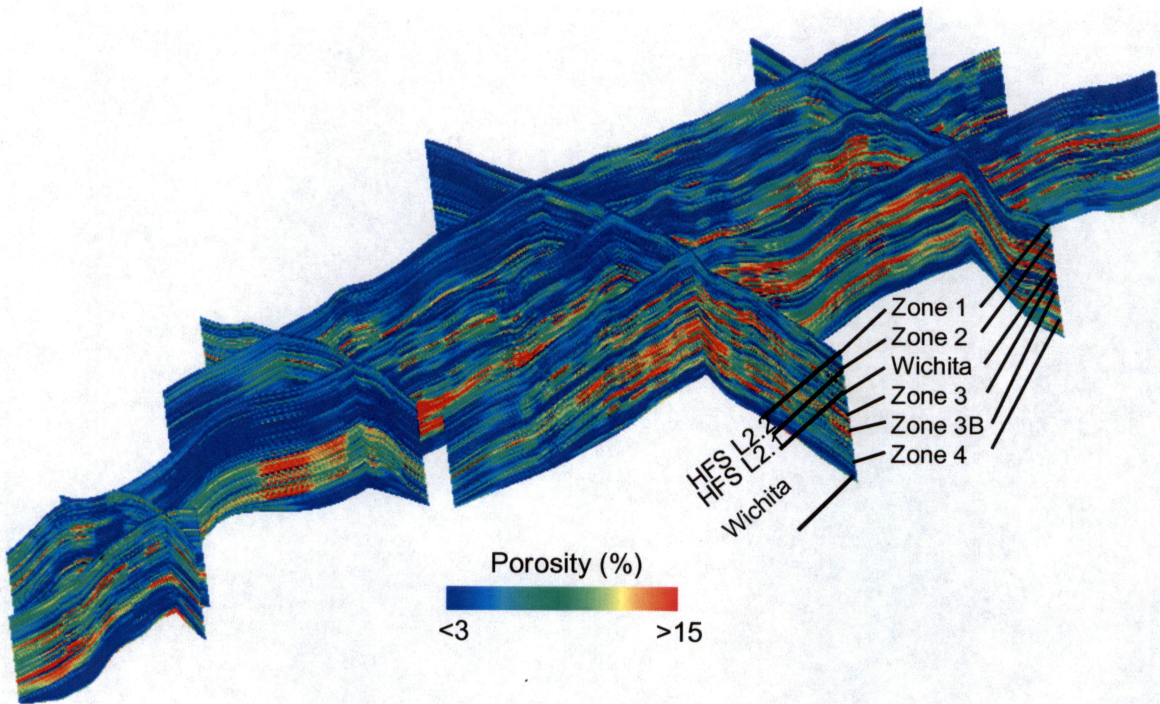


Figure 5. Porosity distribution in fine-grid model.

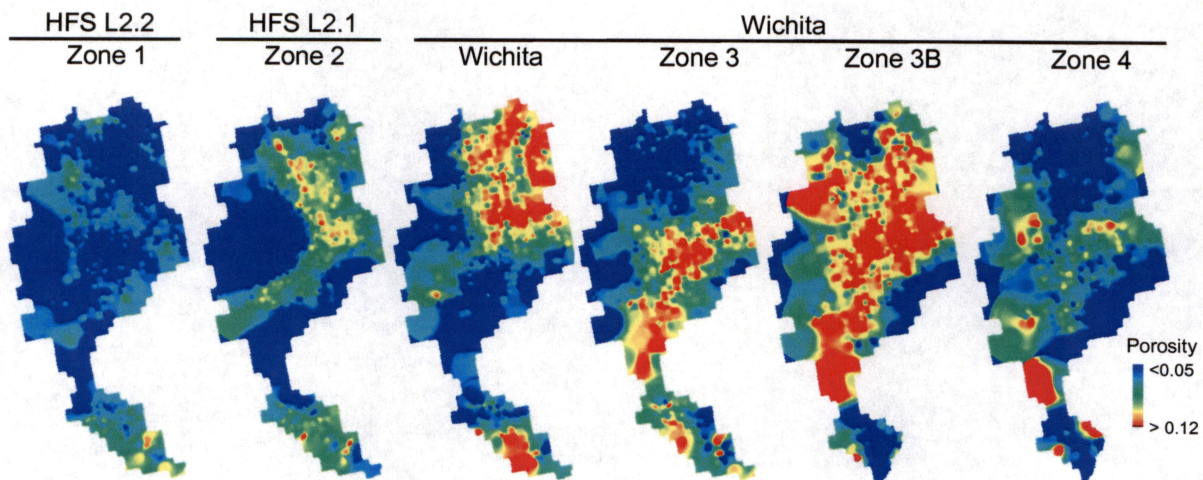


Figure 6. Average porosity distribution, from left to right, in Zone 1, Zone 2, Wichita, Zone 3, Zone 3B, and Zone 4.

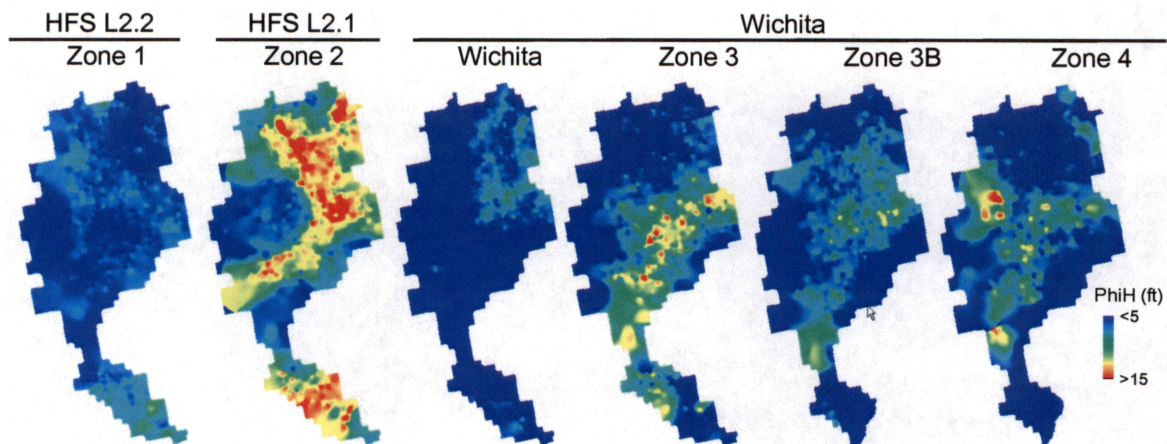


Figure 7. ϕh distribution in reservoir Zone 1 (Lower Clear Fork HFS 2.2) by cycle.

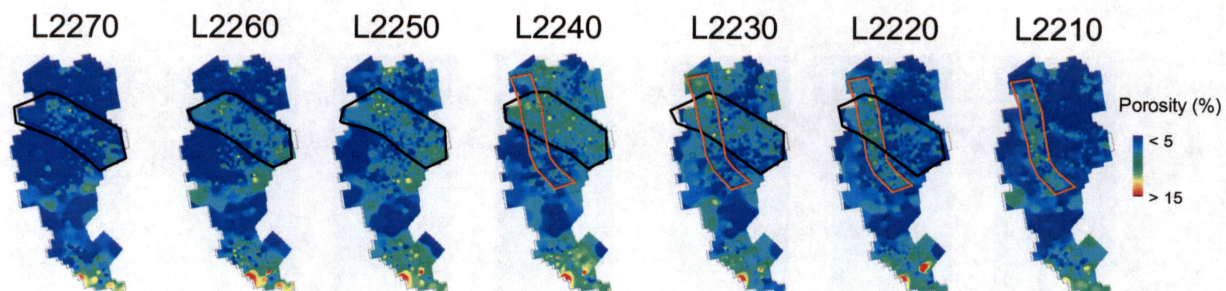


Figure 8. Porosity distribution in reservoir Zone 1 (Lower Clear Fork. HFS 2.2) by cycle.

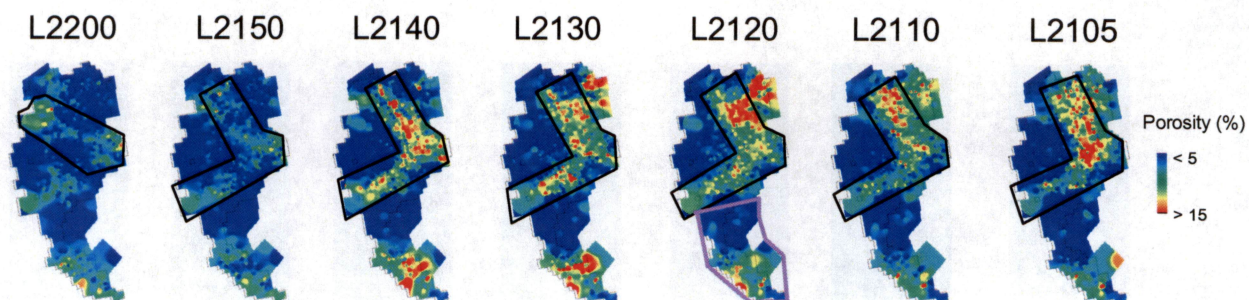


Figure 9. Porosity distribution in reservoir Zone 2, (Lower Clear Fork. HFS 2.1) by cycle.

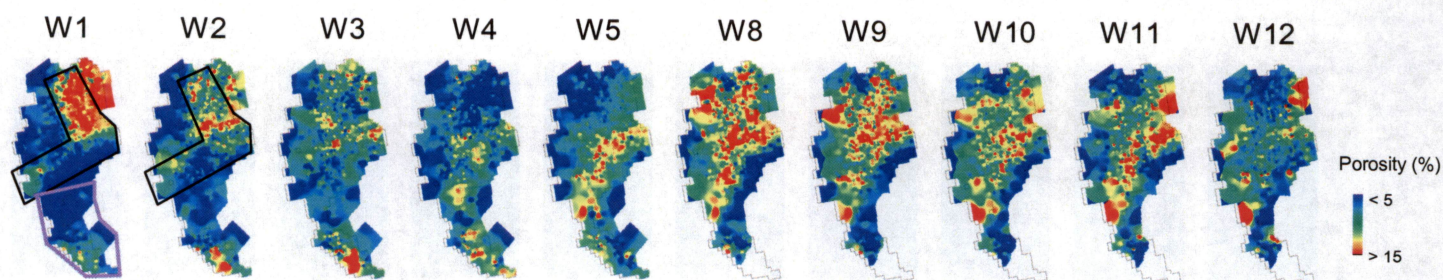


Figure 10. Porosity distribution in Zones Wichita, 3, 3B, and 4, in the Wichita Formation.

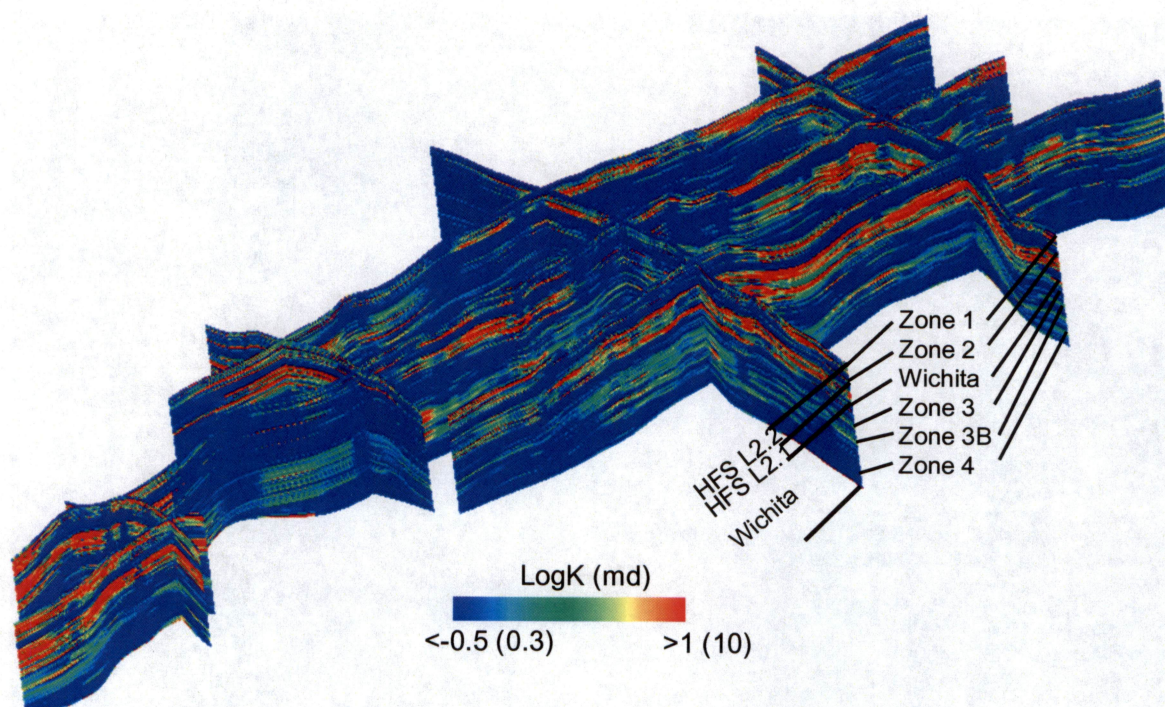


Figure 11. Permeability distribution in 3-D model.

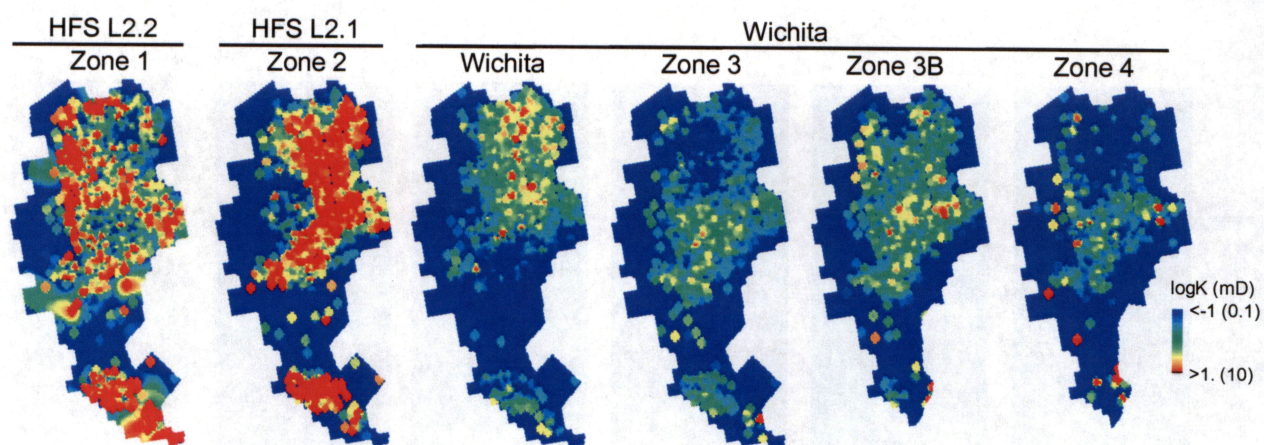


Figure 12. Permeability distribution in reservoir zones 1, 2, Wichita, 3, 3B, and 4.

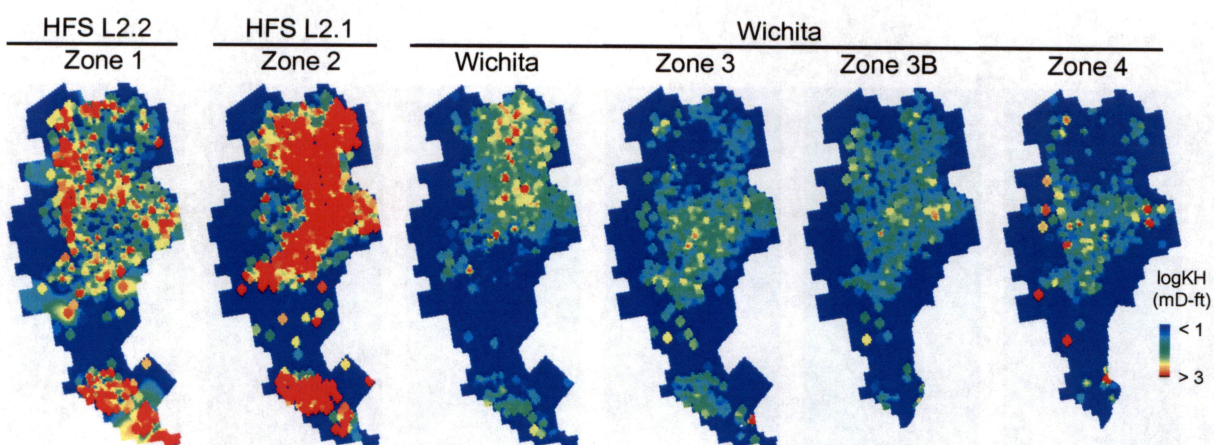


Figure 13. kh distribution in Zone 1, Zone 2, Wichita, Zone 3, Zone 3B, and Zone 4.

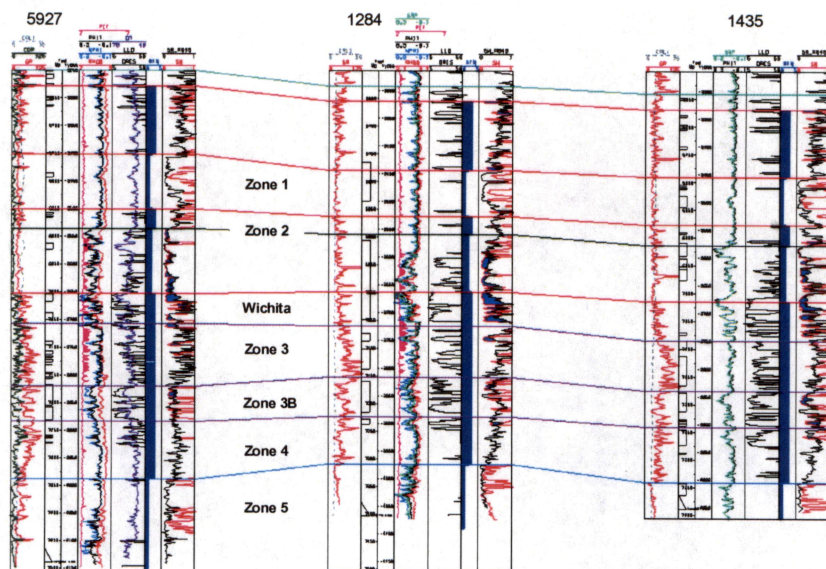


Figure 14. Results of petrophysical analysis in FCU 5927, 1284, and 1435. In the rightmost track, the black curve is water saturation calculated from resistivity, and the red curve is water saturation calculated from capillary pressure correlations (Lucia, this volume).

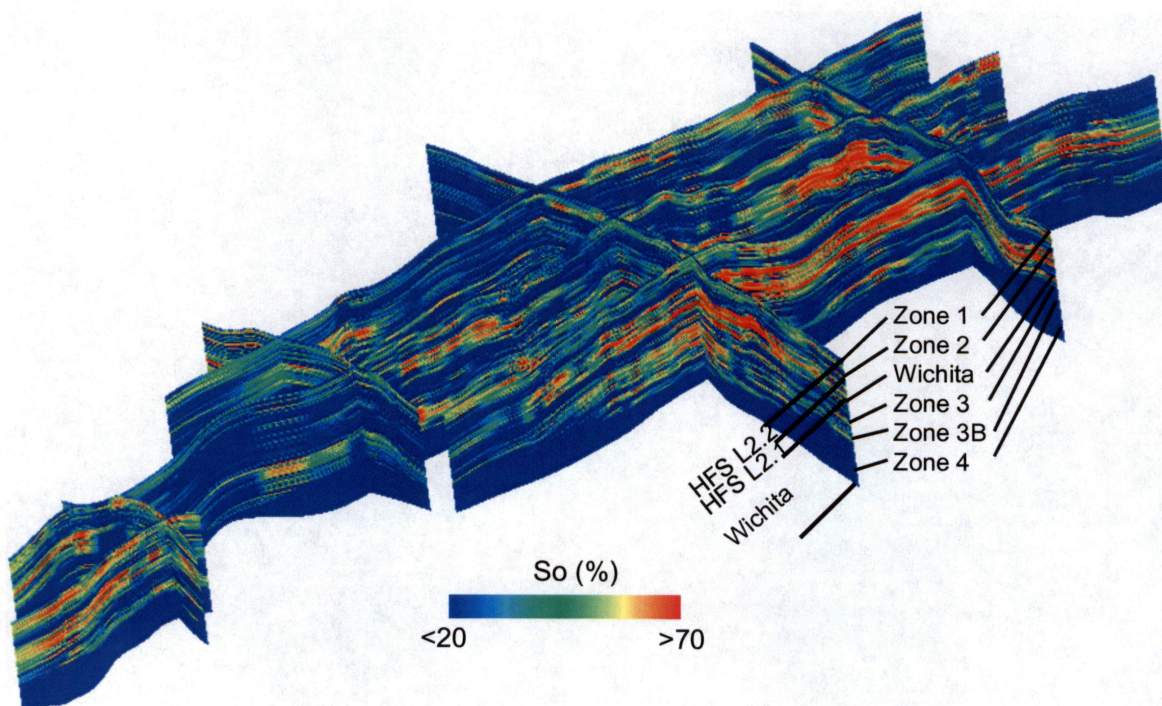


Figure 15. Water saturation distribution in 3-D model with oil-water contact at -3,940 ft.

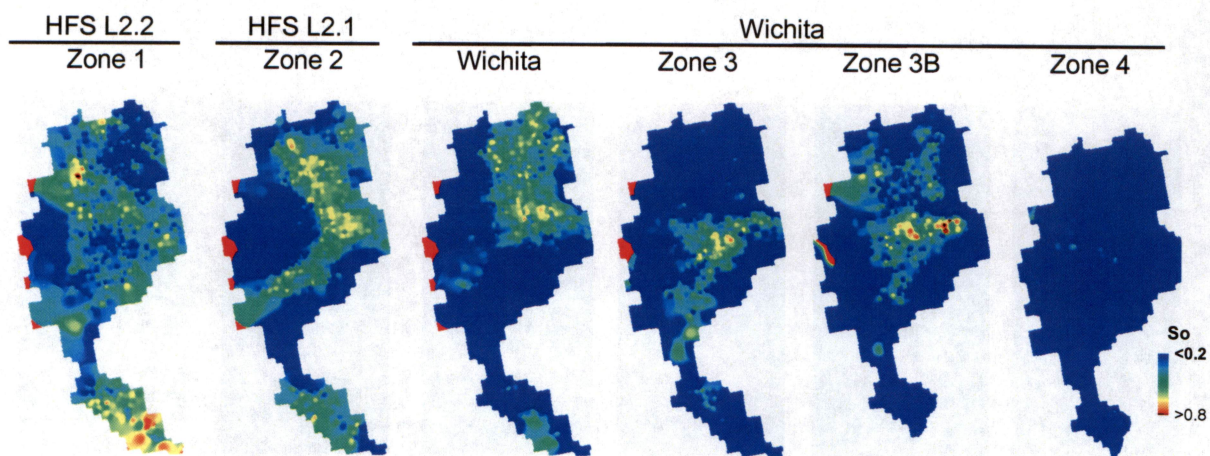


Figure 16. Water saturation distribution in Zone 1, Zone 2, Wichita, Zone 3, Zone 3B, and Zone 4.

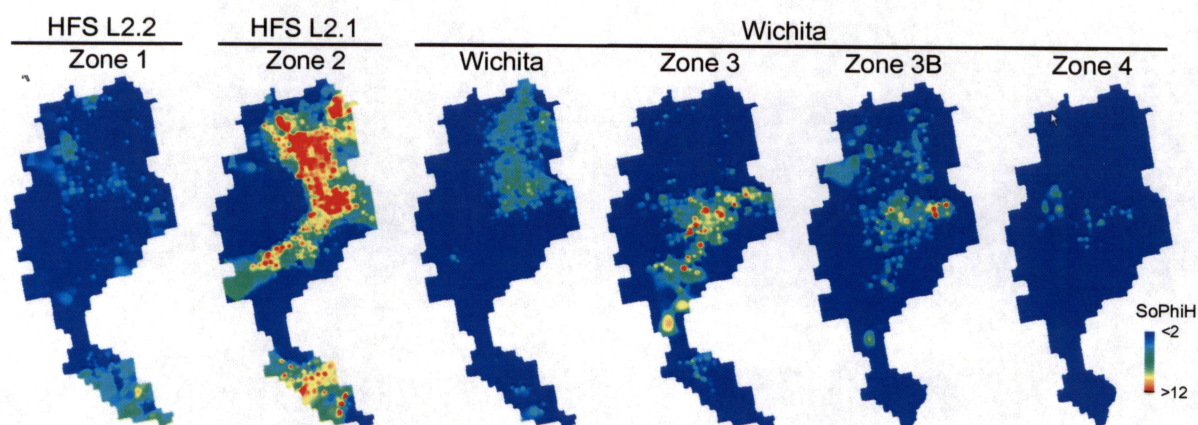


Figure 17. Hydrocarbon volume ($S_o\phi h$) distribution in Zone 1, Zone 2, Wichita, Zone 3, Zone 3B, and Zone 4.

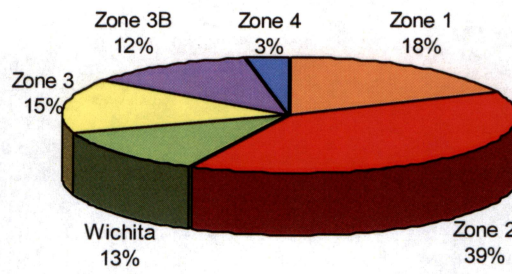


Figure 18. Hydrocarbon volume distribution in six reservoir zones.

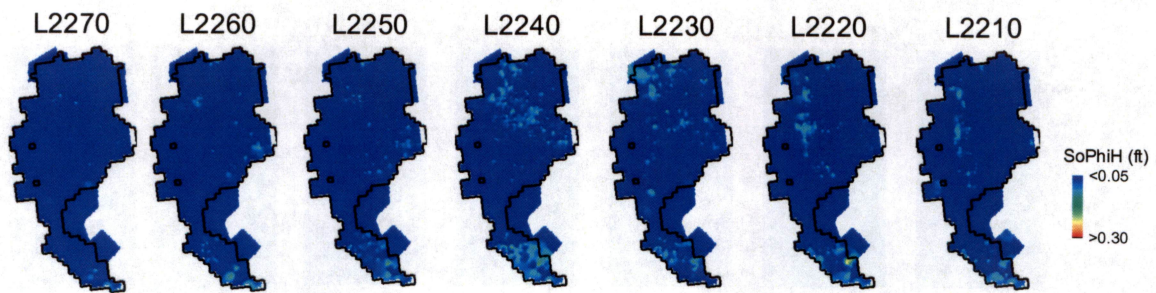


Figure 19. Hydrocarbon volume ($S_o\phi h$) distribution in Zone 1 (Lower Clear Fork HFS L 2.2).

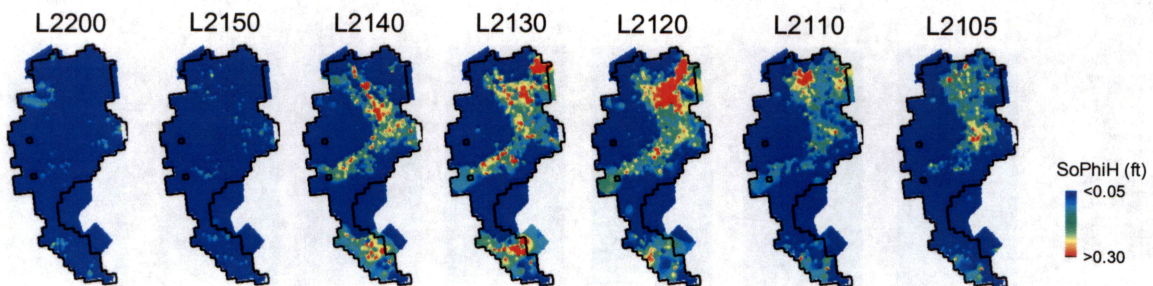


Figure 20. Hydrocarbon volume ($S_o\phi h$) distribution in Zone 2 (Lower Clear Fork HFS L 2.1).

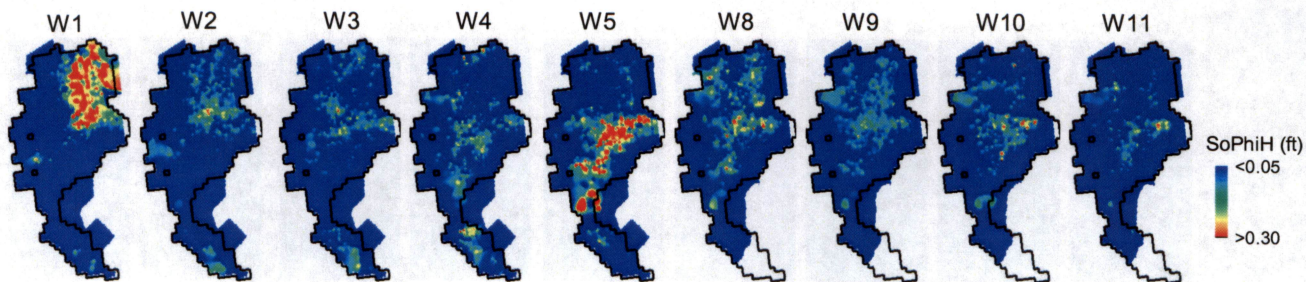


Figure 21. Hydrocarbon volume ($S_o\phi h$) distribution in the Wichita Formation.

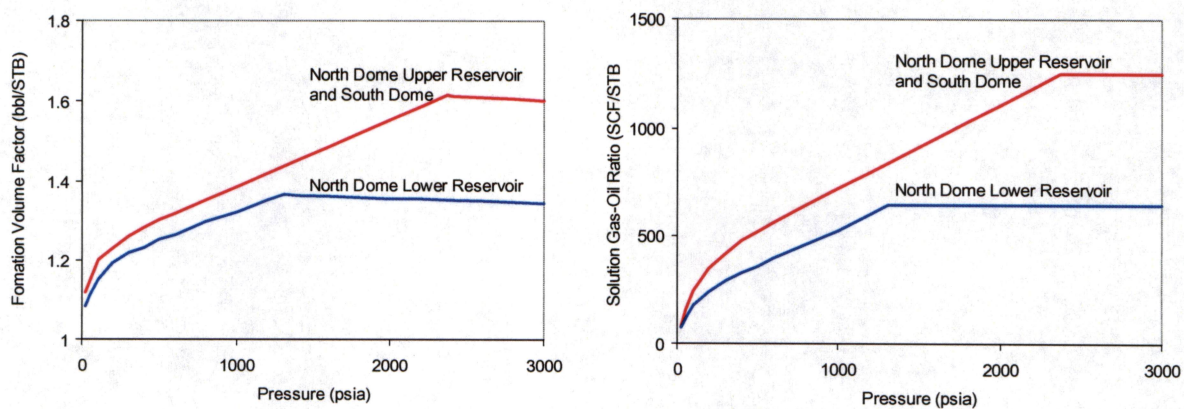


Figure 22. Formation volume factor and oil-gas ratio of two types of crude in FCU (from Field Study Group, 1973).

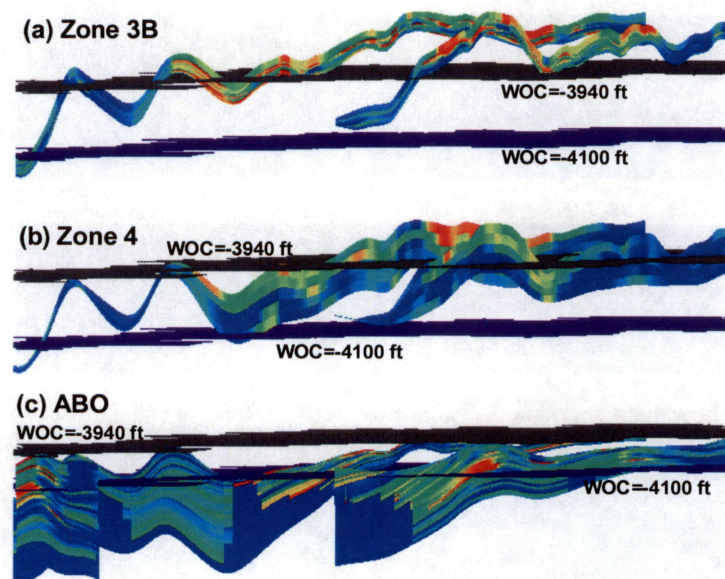


Figure 23. Effect of water-oil contact on vertical coverage in (a) Zone 3B, (b) Zone 4, and (c) Zone 5 (Abo).

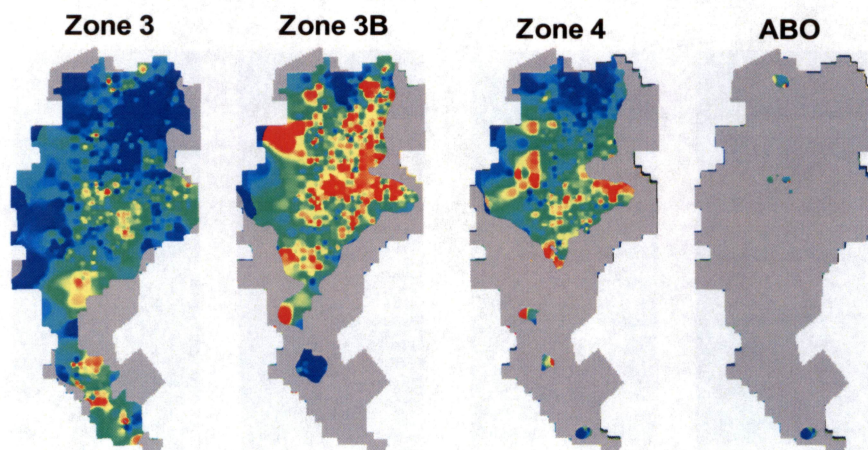


Figure 24. Effect of water-oil contact on areal coverage in Zone 3, Zone 3B, Zone 4, and Zone 5 (Abo).

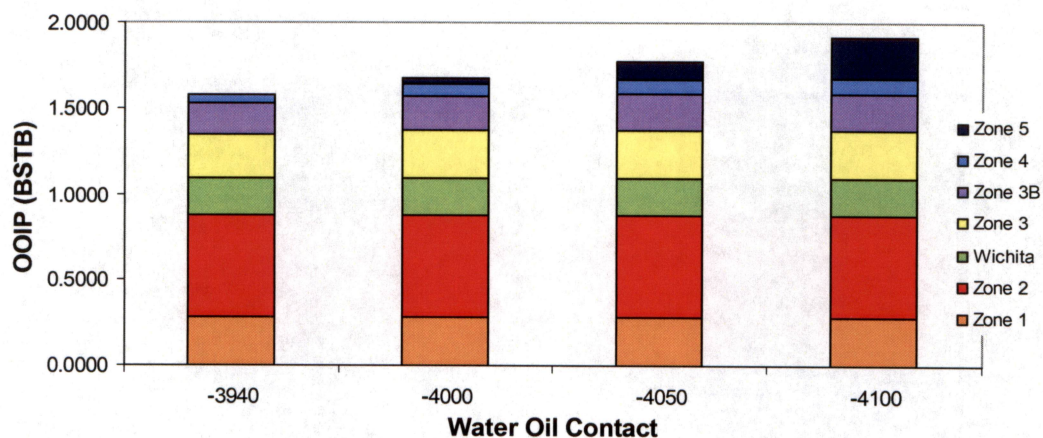


Figure 25. Effect of water-oil contacts on OOIP estimate.

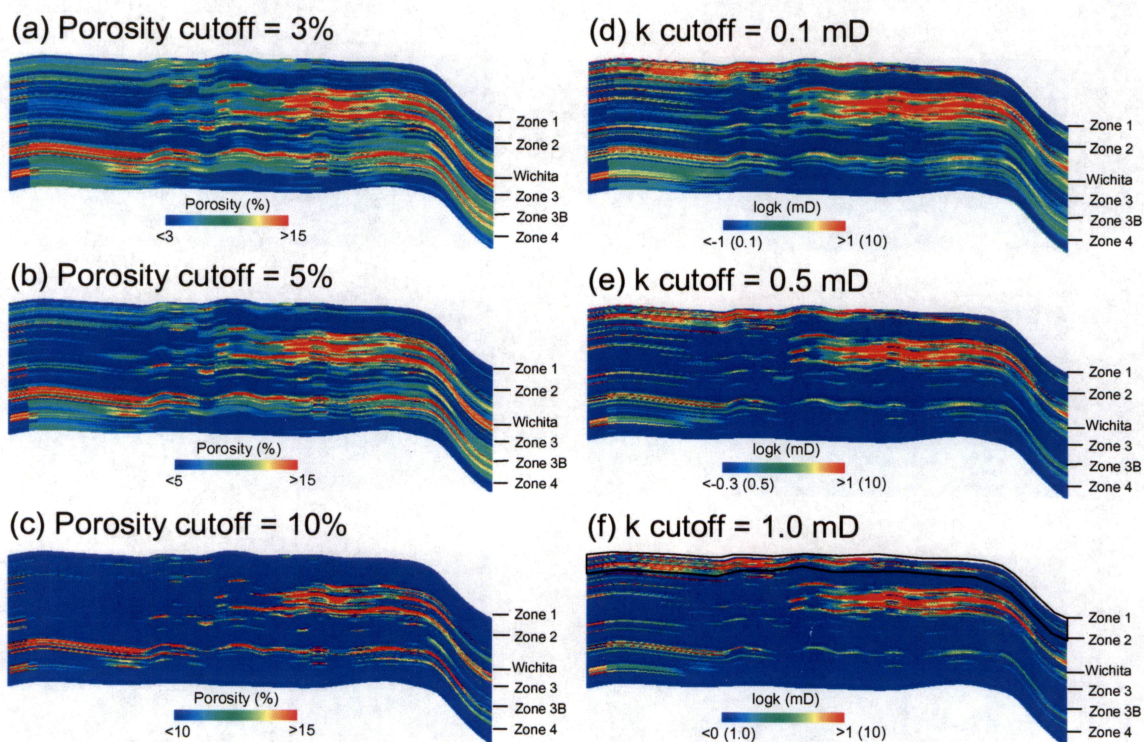


Figure 26. Effects of porosity cutoffs of (a) 3%, (b) 5% and (c) 10%, and permeability cutoffs of (d) 0.1, (e) 0.5 and (f) 1 mD on volumetrics.

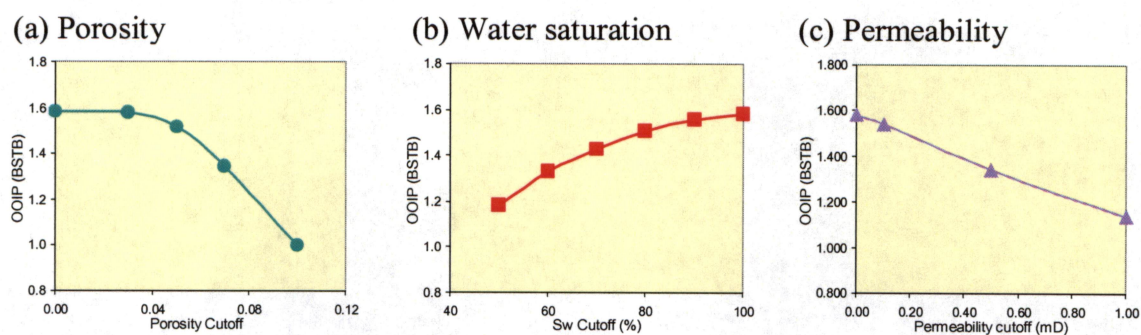


Figure 27. Effects of cutoff values on OOIP estimate: (a) porosity, (b) water saturation and (c) permeability.

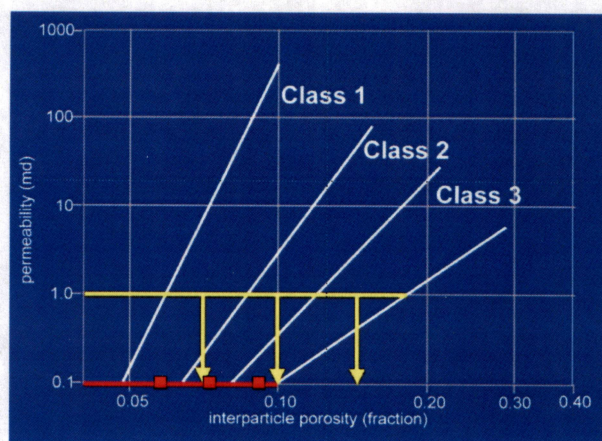


Figure 28. Relationship between permeability and porosity cutoff values. A specific permeability cutoff represents rock-fabric-dependent porosity cutoffs.

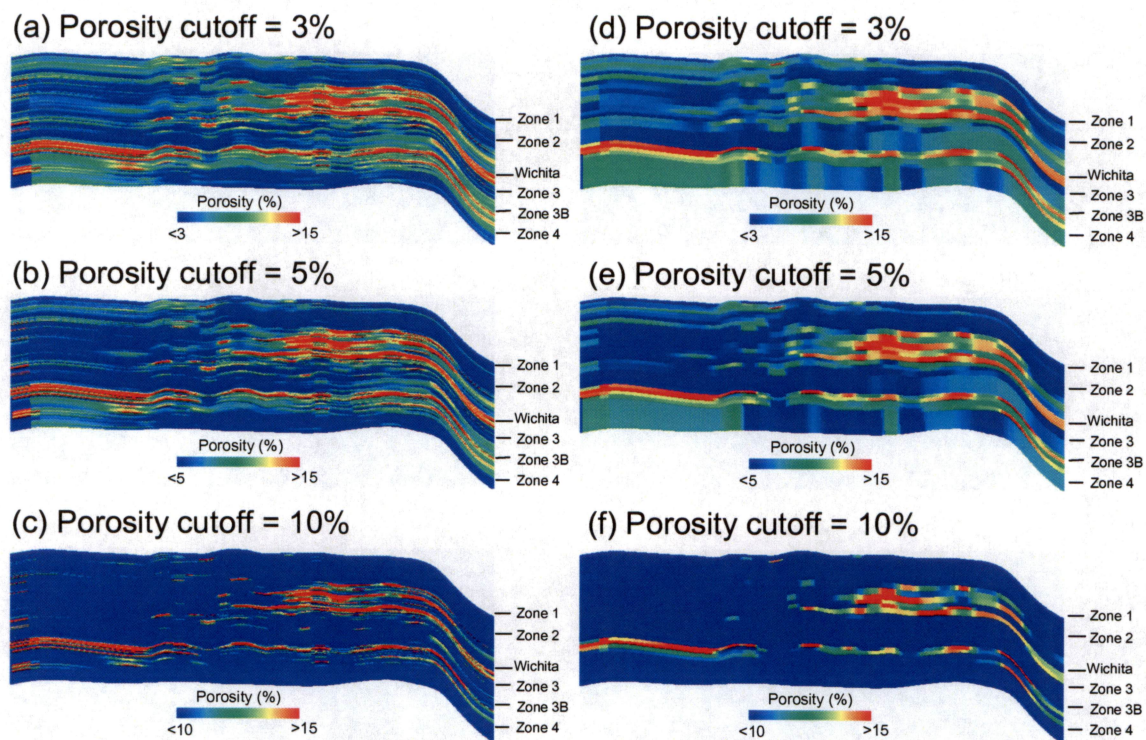


Figure 29. Effects of porosity cutoffs and grid vertical resolution on volumetrics, (a) 3%, (b) 5% and (c) 10% on fine-grid model, and (d)) 3%, (e) 5% and (f) 10% on cycle-based model.

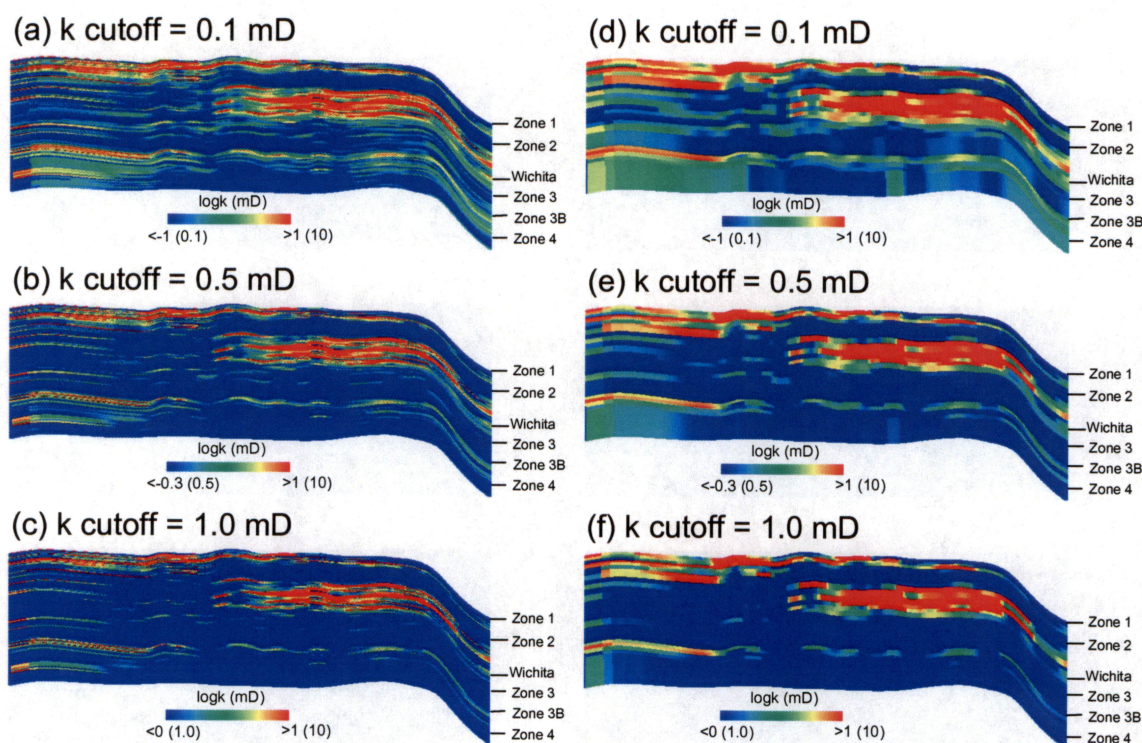


Figure 30. Effects of porosity cutoffs and grid vertical resolution on volumetrics, (a) 0.1, (b) 0.5 and (c) 1.0 mD on fine-grid model, and (d) 0.1, (e) 0.5 and (f) 1.0 mD on cycle-based model.

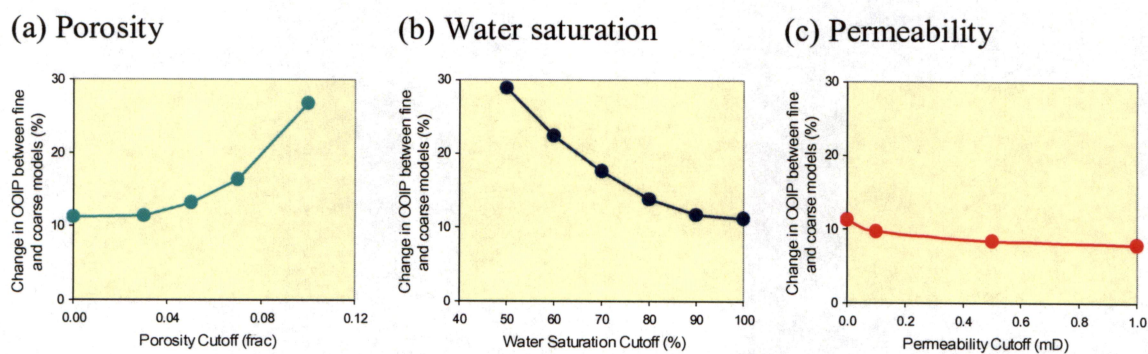


Figure 31. Changes in OOIP between high-resolution and cycle-based models with respect to (a) porosity cutoff, (b) water saturation cutoff and (c) permeability cutoff values.

Figure 33. Initial 3:1 line-drive waterflooding pattern. Production is expected to be higher in the middle row of producers (red) than in the other two rows of producers closer to injectors (green).

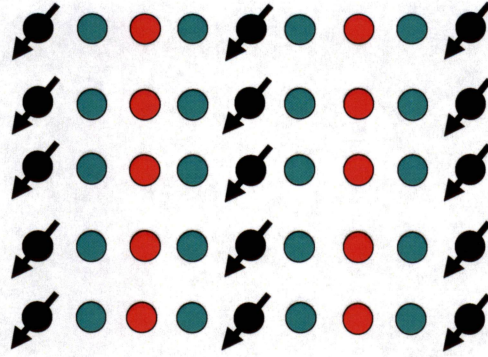
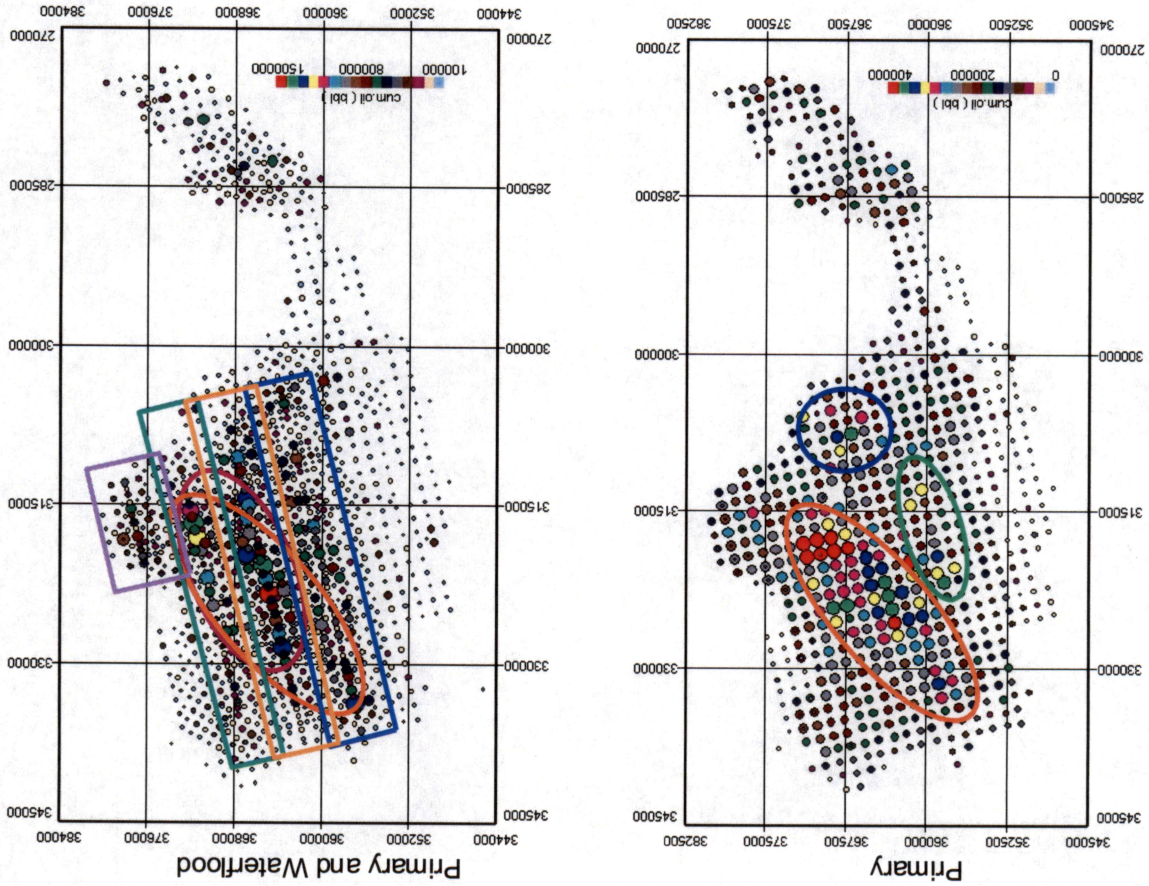


Figure 32. Production data and trends in primary and waterflood.



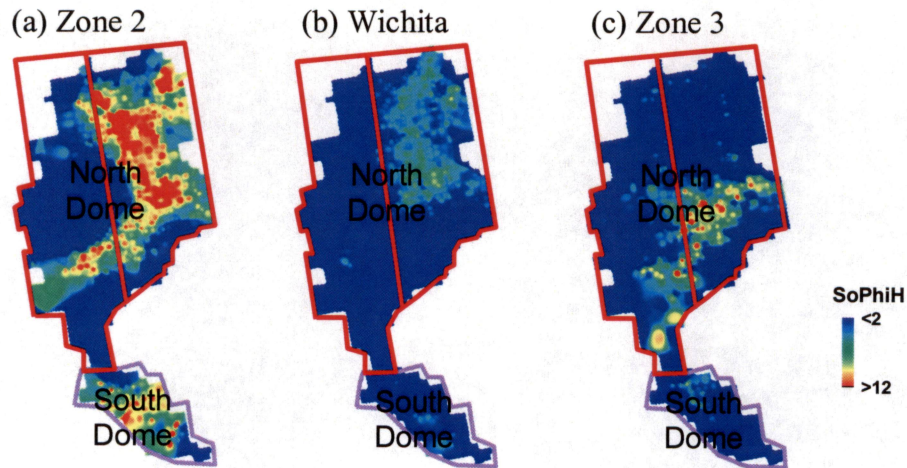


Figure 34. Porosity and $S_0\phi h$ in (a) Zone 2, (b) Wichita, and (c) Zone 3, overlaid with production trends. The best production areas during primary and waterflooding coincide with the high porosity and $S_0\phi h$ trends in zone.

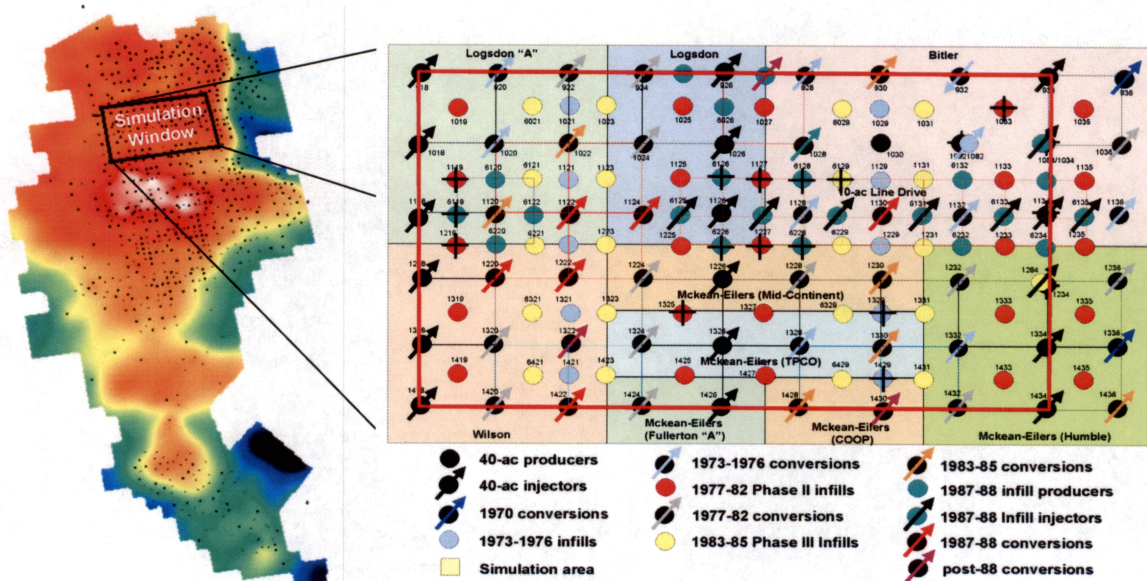
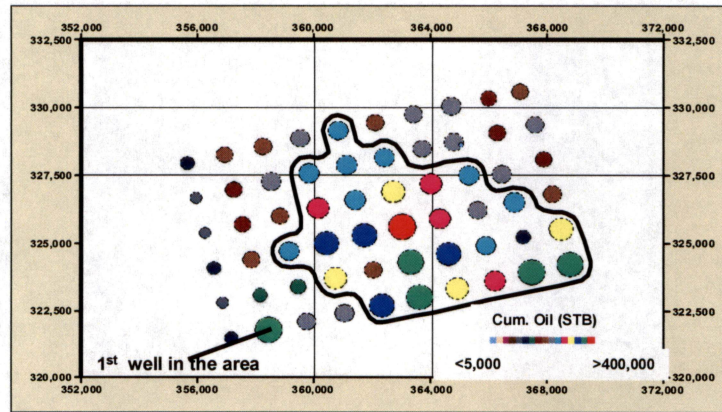


Figure 35. Water-injection patterns in the initial reservoir model area in 2001. The area of reservoir simulation is outlined by the red box. Development history is illustrated by colored symbols.

(a) Primary recovery



(b) Waterflooding recovery

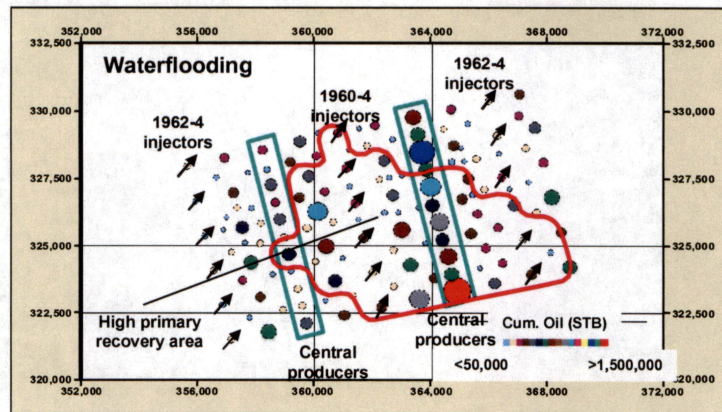


Figure 36. Production data and trends in (a) primary and (b) waterflooding in simulation area.

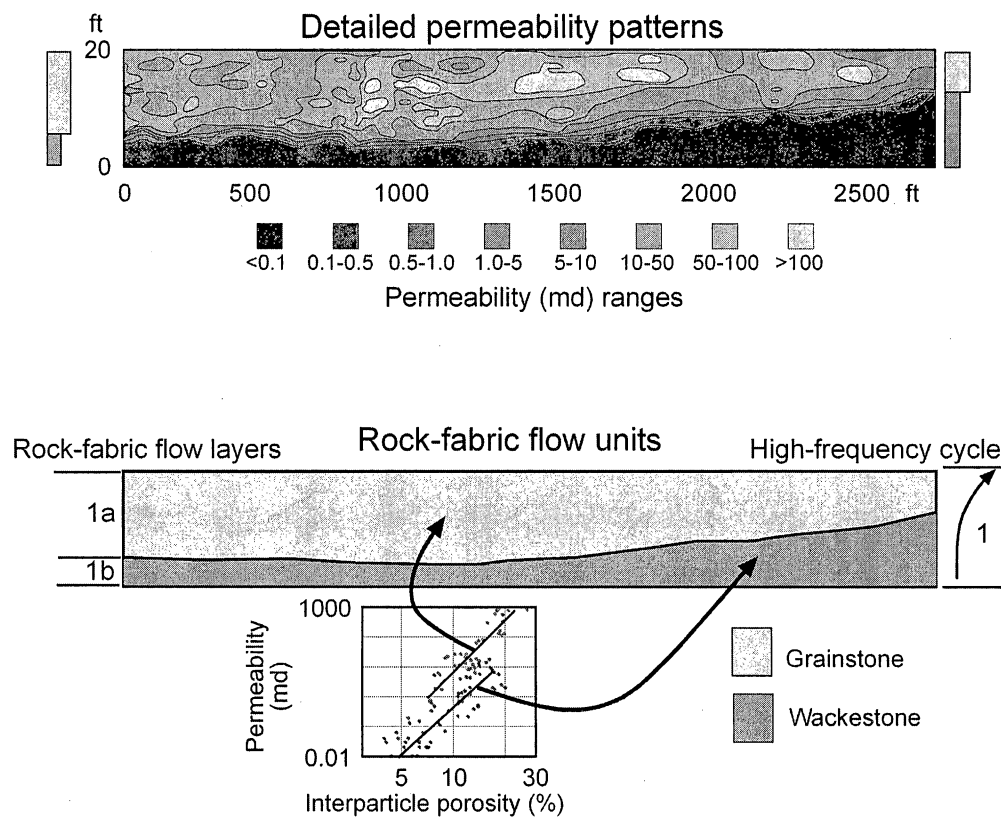


Figure 37. Lawyer Canyon cycle 1 flow-layer model.

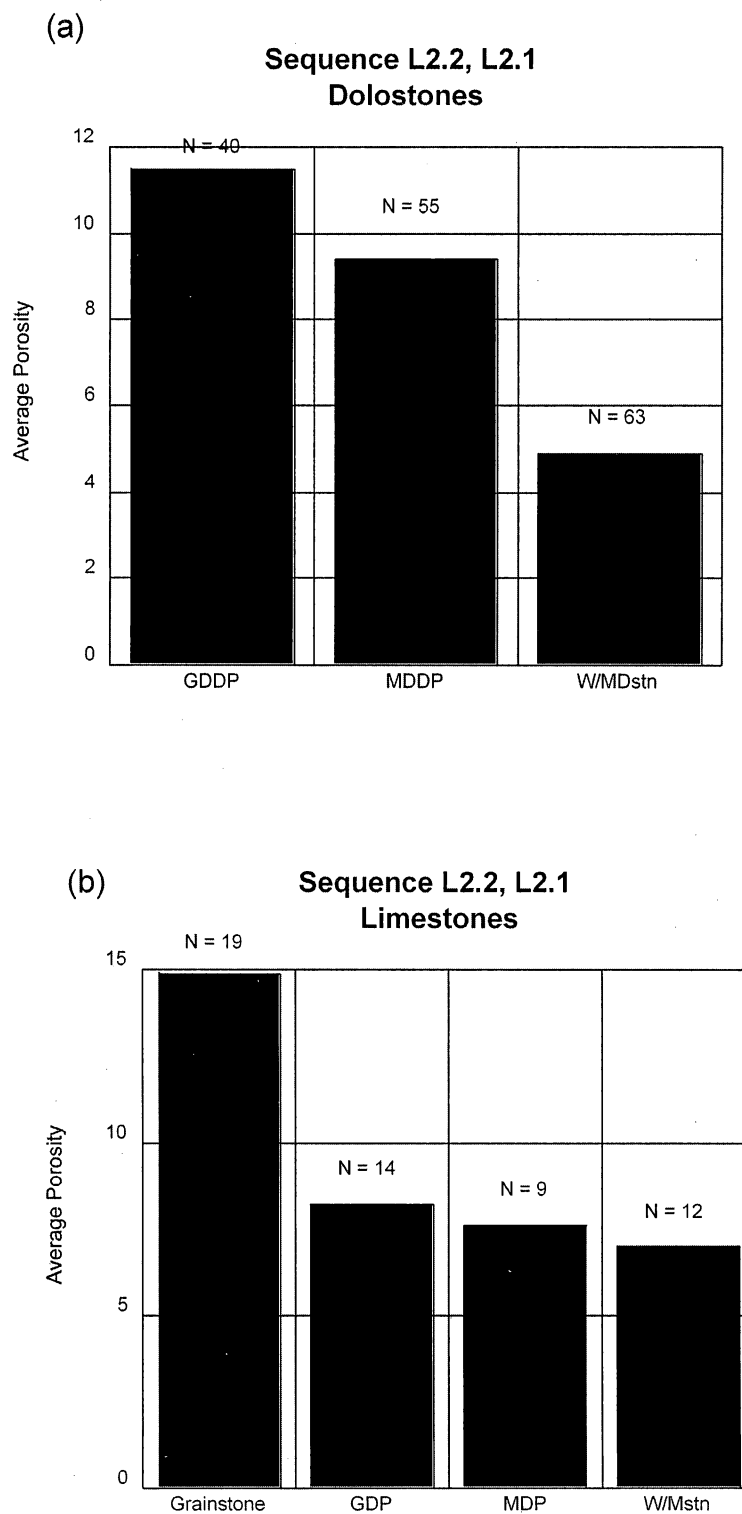


Figure 38. Average porosity for various rock fabrics in sequences L2.1 and L2.2. (a) Dolostone rock fabrics showing decrease in porosity with increasing lime mud. (b) Limestone rock fabrics showing high porosity correlated with grainstones. Grain-dominated packstones (GDP) may have sufficient lime mud to be described as mud dominated packstones (MDP).

Sequence L2.1
FCU 5927

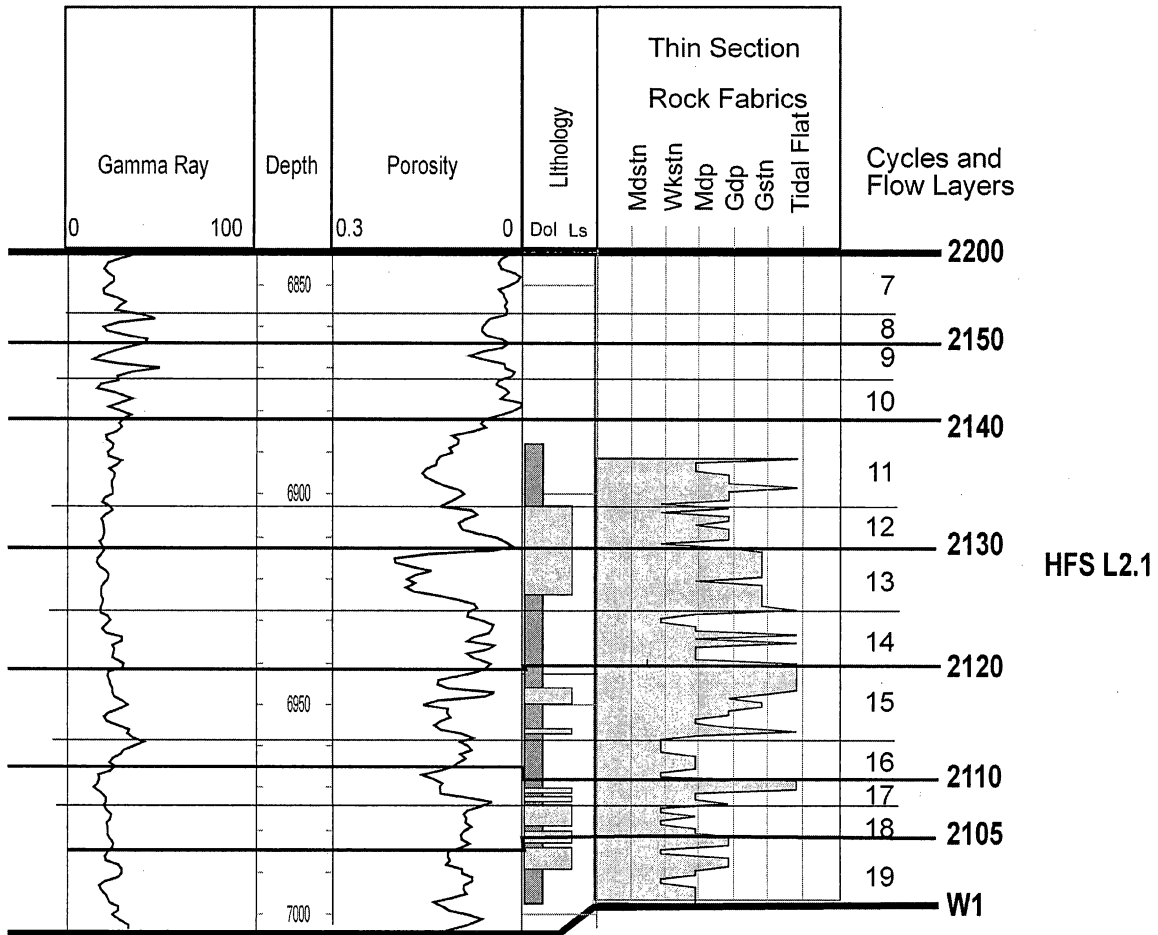


Figure 39. Flow layers and cycles in sequence L2.1.

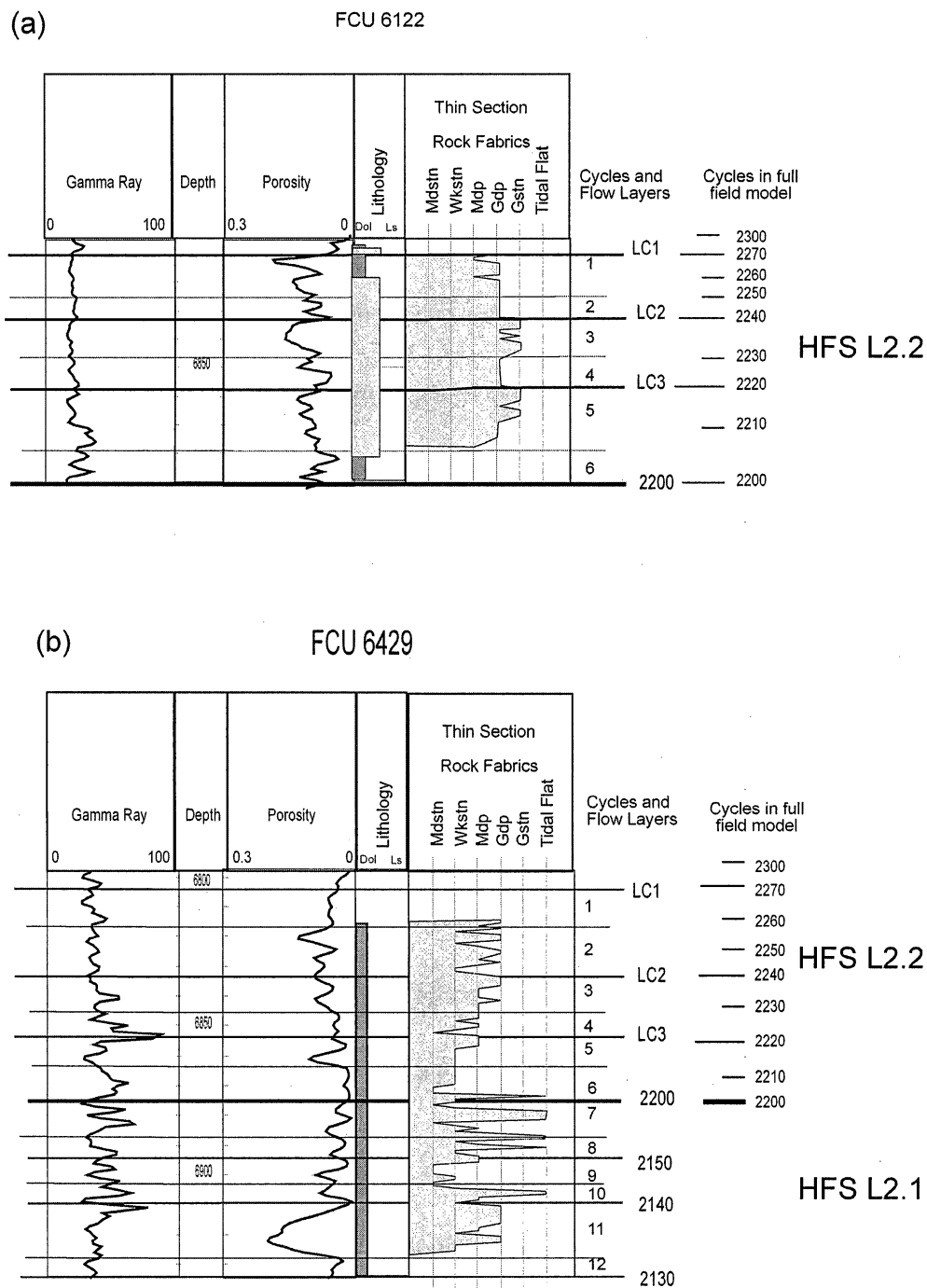


Figure 40. Flow layers in sequence L2.2. The cycles and flow layers in the simulation model are compared with the cycles in the full field model. (a) In the limestone area there is a reasonable correlation between cycles, flow layers, and porosity. (b) In the dolostone area the correlation between cycles, flow layers, and porosity is less apparent.

Wichita FCU 5927

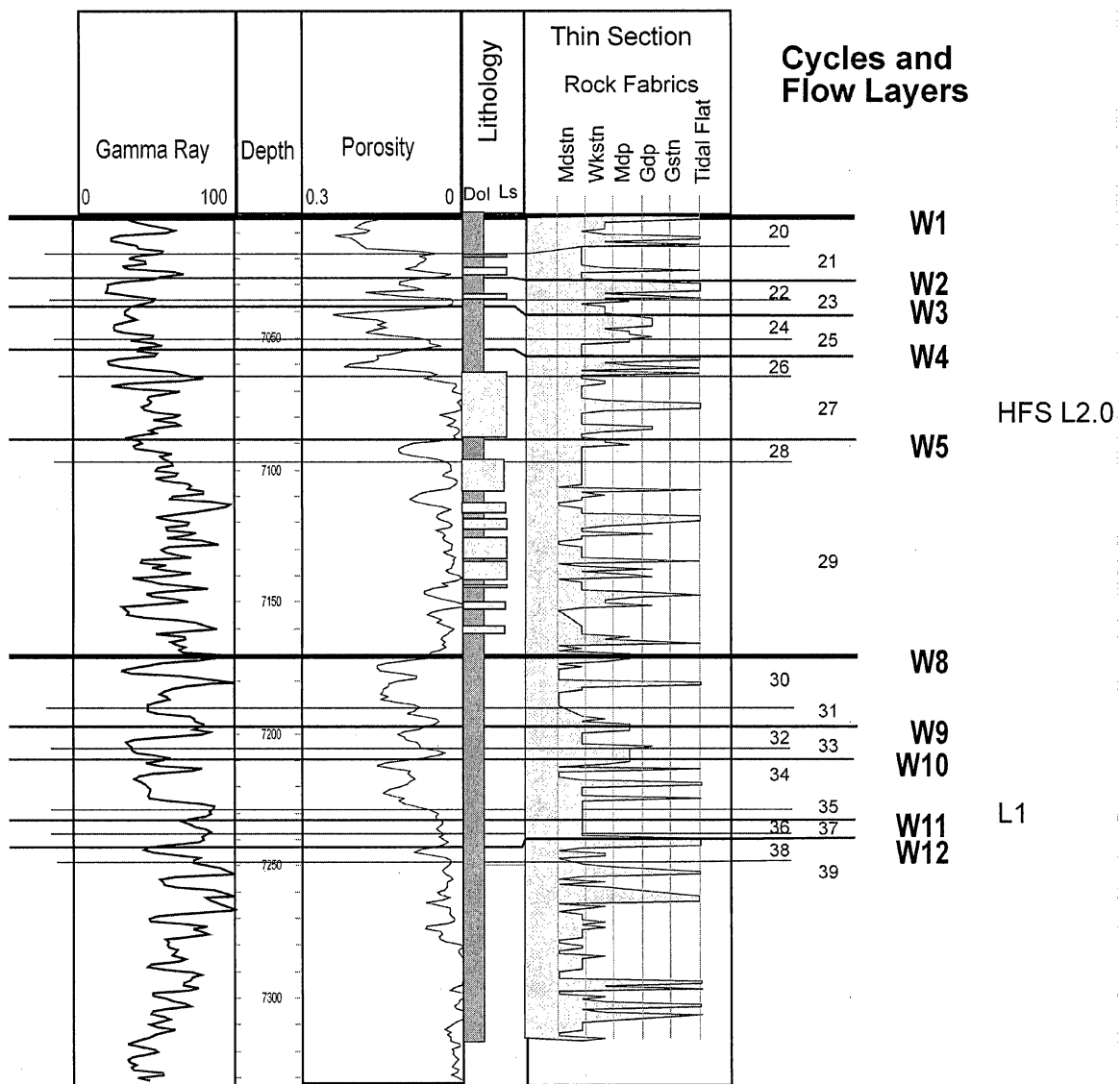


Figure 41. Flow layers in the Wichita.

Flow Unit Architecture Fullerton Clear Fork/Wichita Reservoir

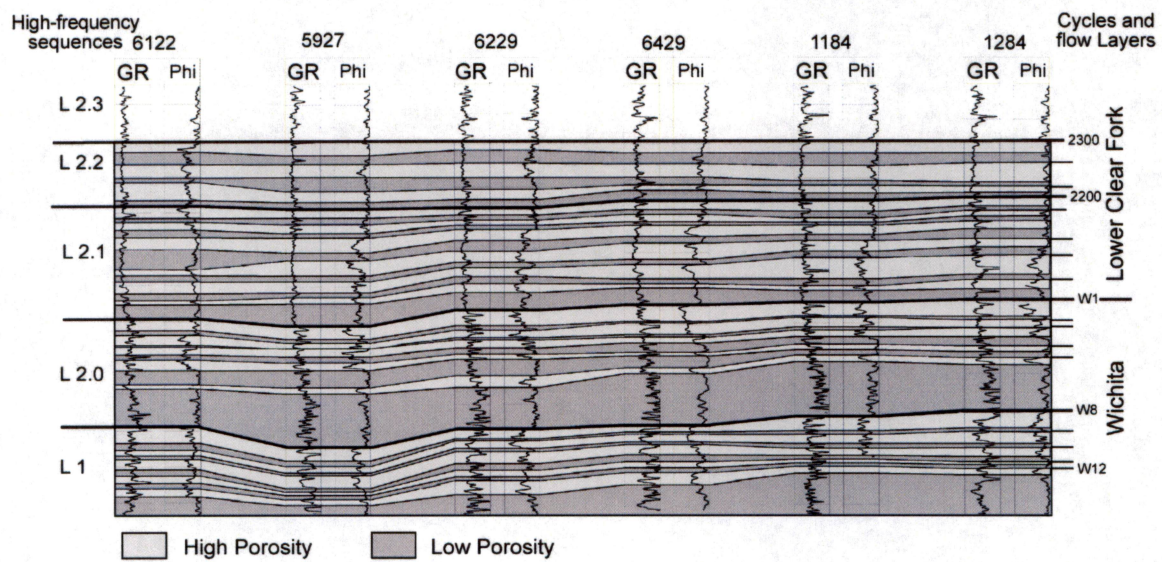


Figure 42. Lower Clear Fork and Wichita flow layers in cored wells of simulation area illustrating the use of porosity to build a flow model.

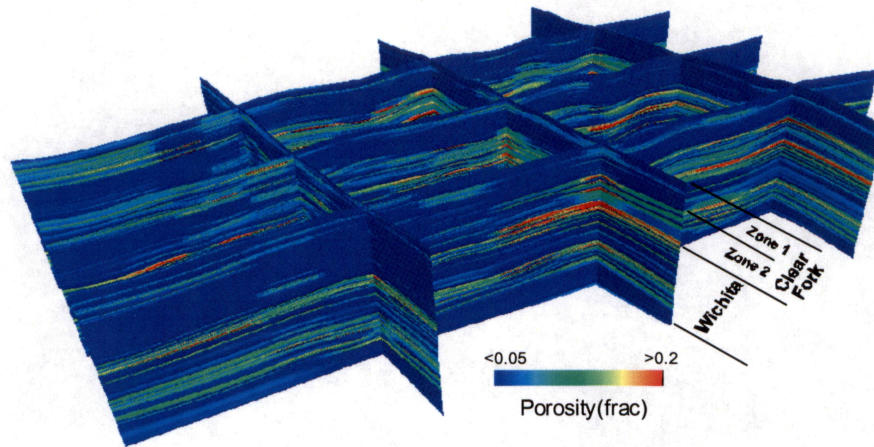


Figure 43. Porosity distribution in the simulation area.

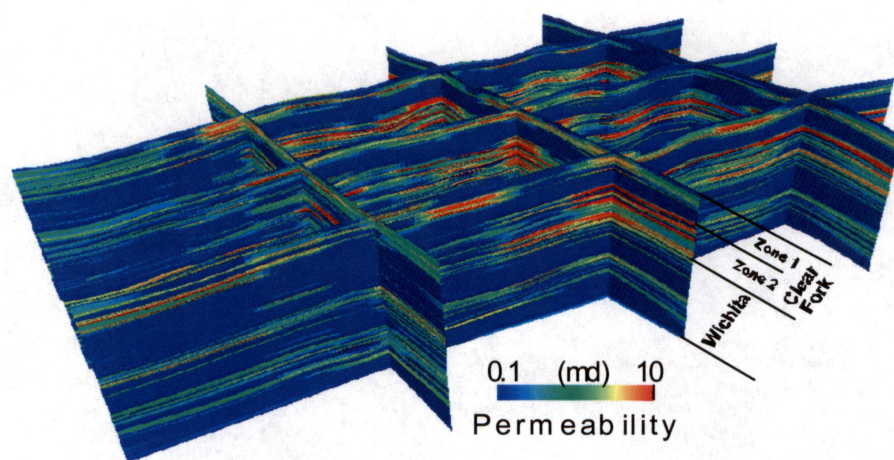


Figure 44. Permeability distribution in the simulation area.

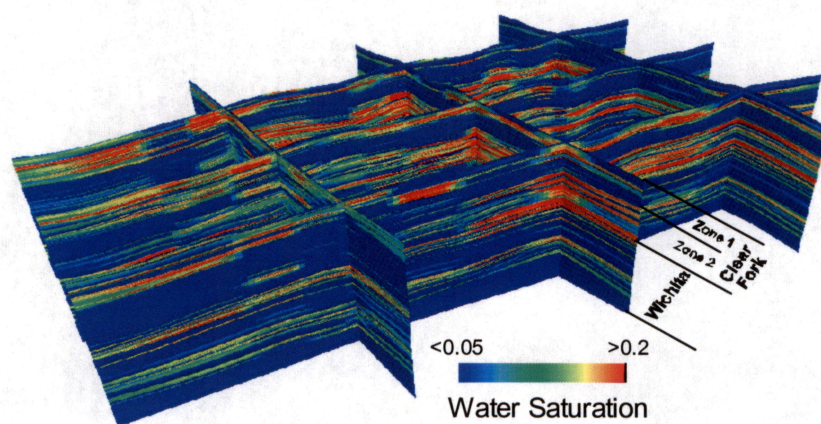


Figure 45. Water saturation distribution in the simulation area.

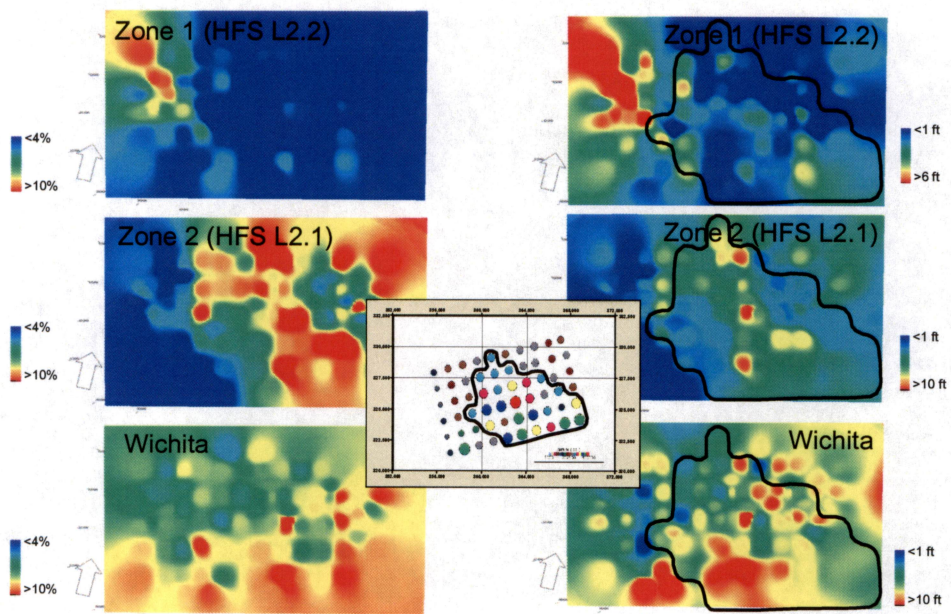


Figure 46. Porosity and $S_o\phi h$ trends in the simulation area.

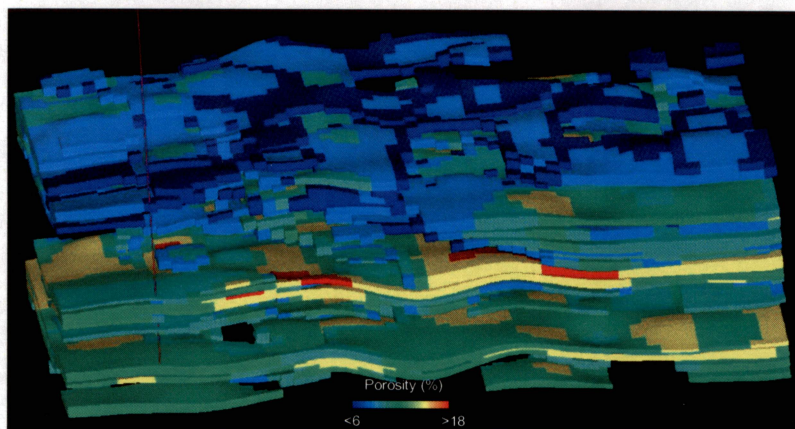


Figure 47. Porosity distribution in simulation model.

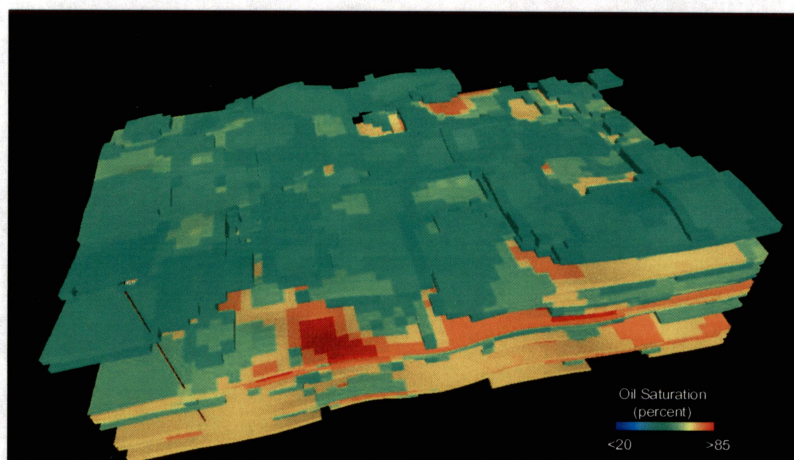


Figure 48. Initial oil saturation in simulation model.

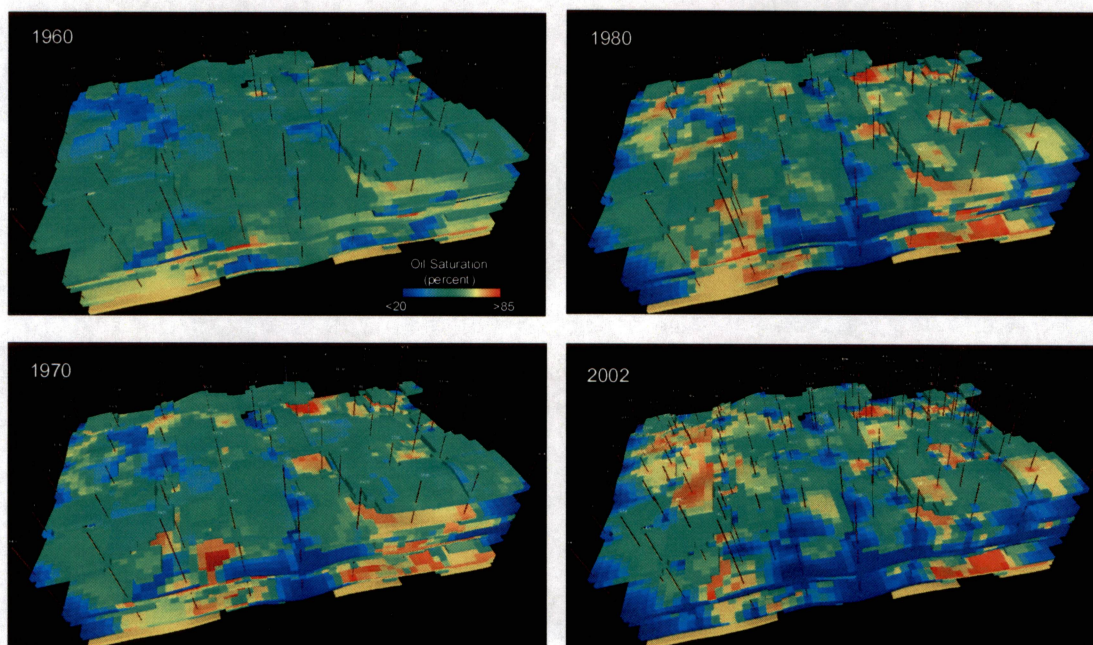


Figure 49. Simulated oil saturation in 1960, 1970, 1980, and 2002, simulation area.

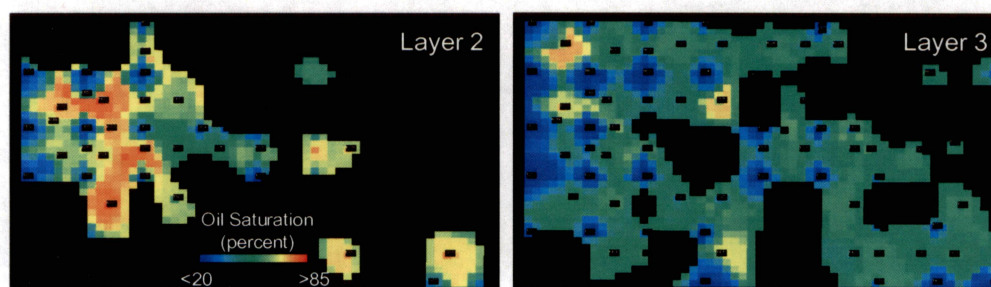


Figure 50. Simulated oil saturation in 2002, in Zone 1.

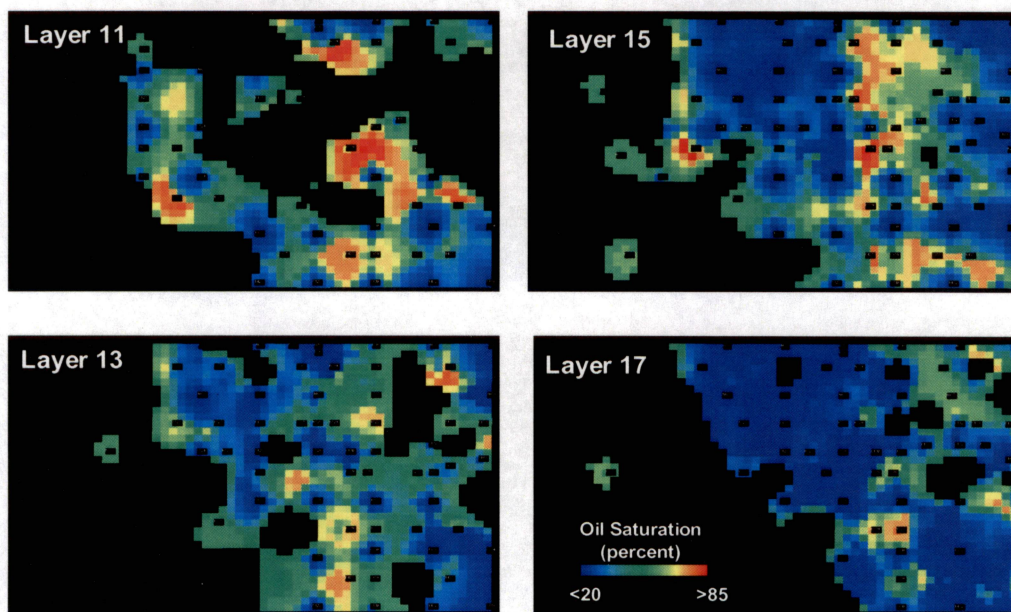


Figure 51. Simulated oil saturation in 2002, in selected model layer slices of the Lower Clear Fork HFS L2.1 (reservoir Zone 2).

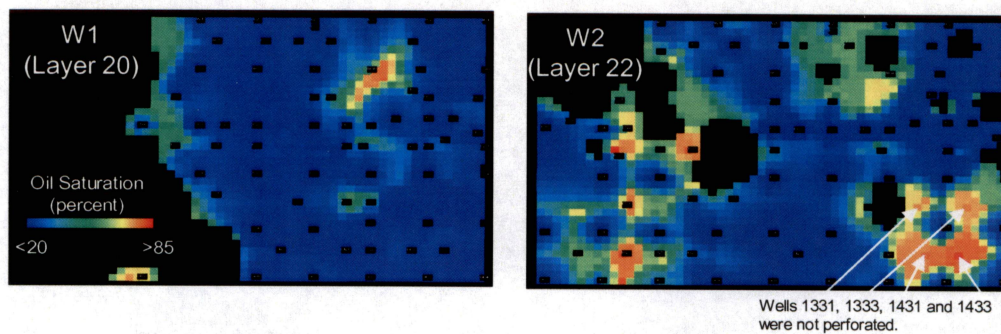


Figure 52. Simulated oil saturation in 2002, in upper model layers of the Wichita.

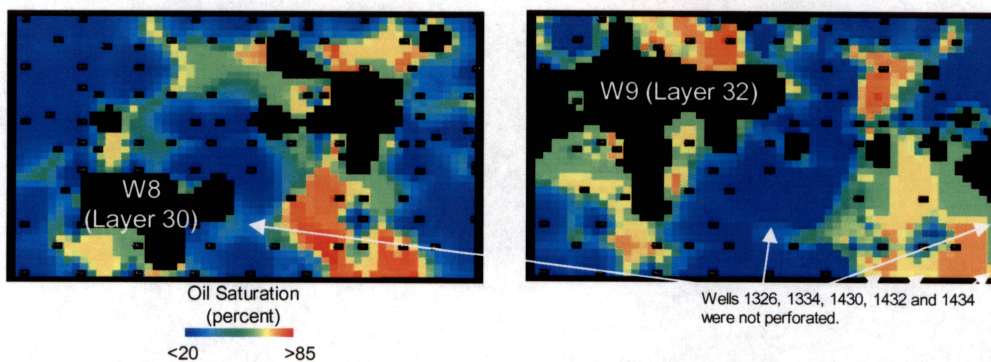


Figure 53. Simulated oil saturation in 2002, in model layers of Wichita reservoir Zone 3B. Note that the oil has not been produced or swept from the southeasternmost part of the model area.

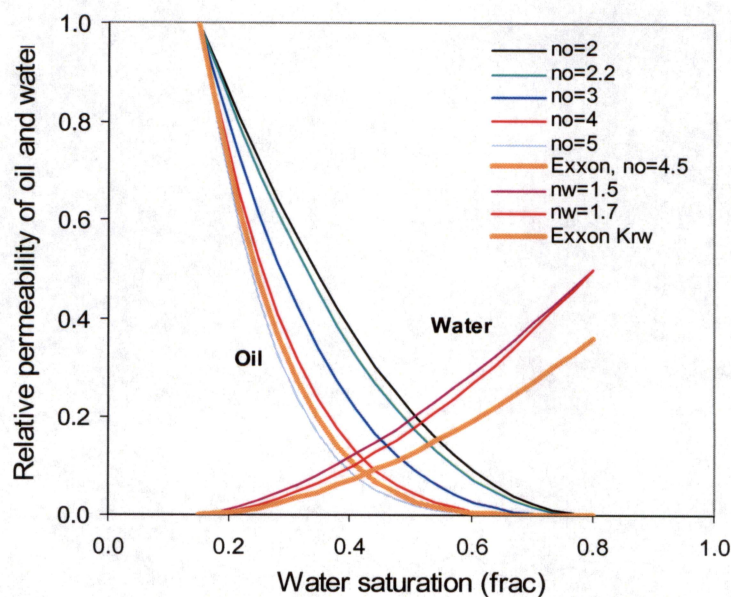


Figure 54. Corey correlations for relative permeability.

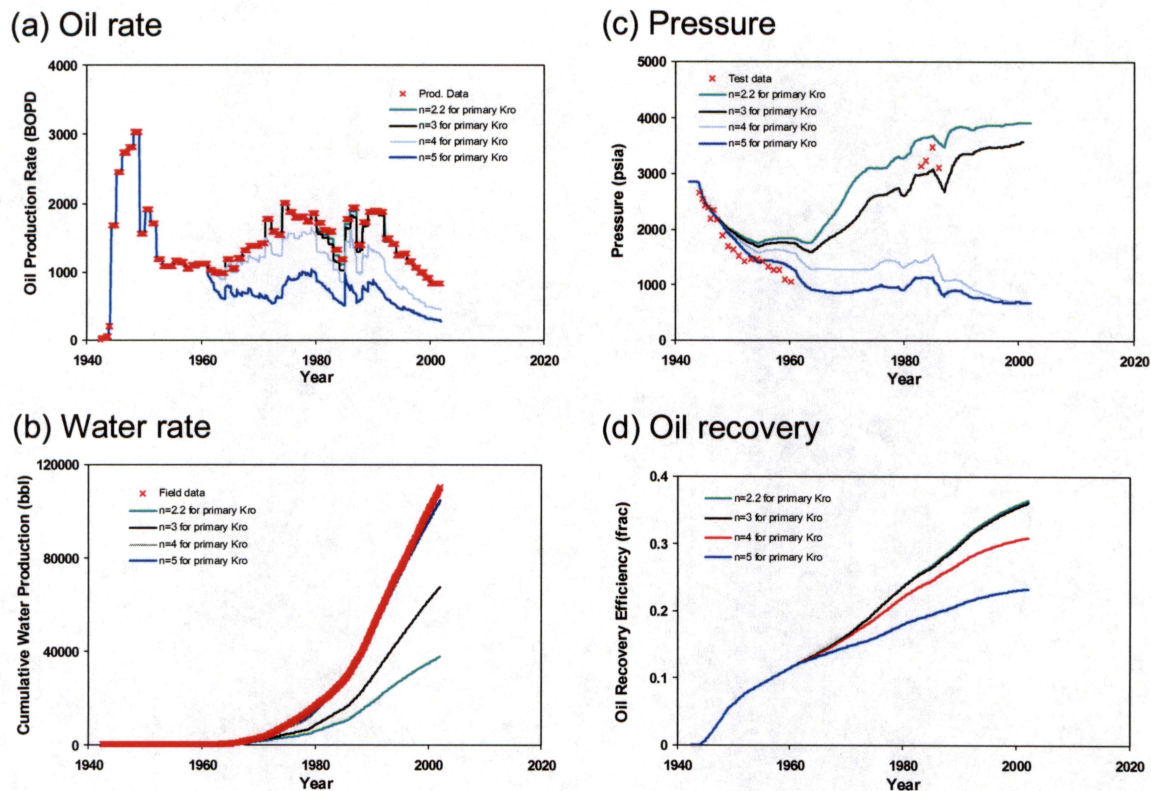


Figure 55. Effect of relative permeability on simulated (a) oil rate, (b) water rate, (c) pressure and (d) oil recovery.

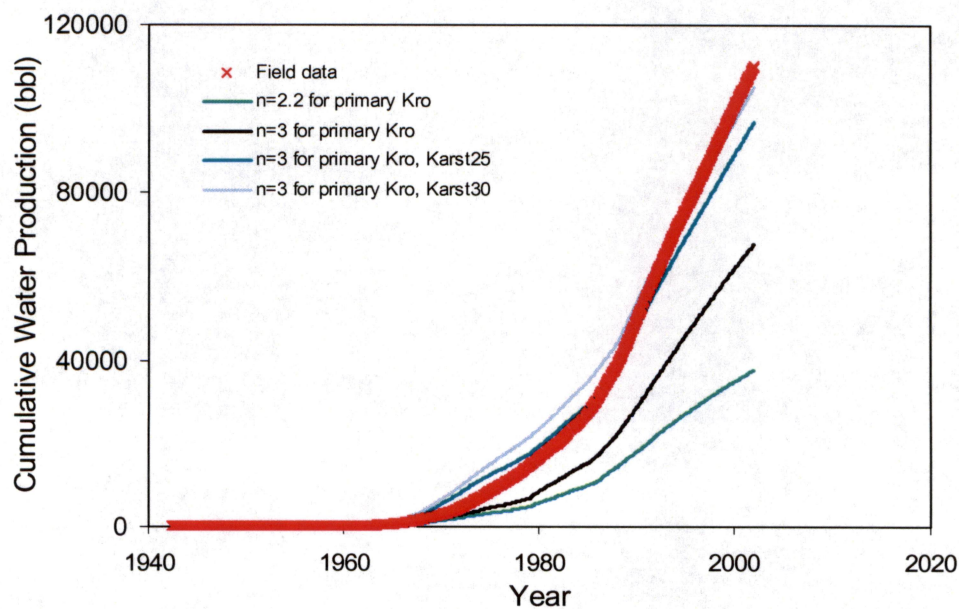


Figure 56. Effect of permeability multiplication on simulated water production.

APPENDIX A: UPSCALING

Permeability Upscaling in Vertical Direction

Because the vertical resolution of 3D static models is commonly much coarser than that of wireline logs, upscaling is an issue encountered in several stages in 3D modeling. The arithmetic mean is normally used in porosity and water saturation upscaling. Permeability upscaling in vertical direction, the frequently debated issue between geologists and engineers, should be resolved in the early stage of 3D modeling. The argument for geologists is that because permeability data are commonly log-normally distributed, geometric mean should be used according to the statistical theorem; the argument for engineer is that upscaling is a process of averaging based on the theory of fluid flow through porous media rather than the geometric mean based on the statistical theory.

The differences in permeability among arithmetic, geometric means and a k - ϕ correlation (Lucia, 1999) can be demonstrated by simple two-layer models shown in table A.1 and fig. A.1. Permeabilities for class 2 rock-fabric carbonates is given by Lucia (1999)

$$k_{rf2} = 10^{6.1736 \log(\phi/100) + 6.1606} \quad (A.1)$$

Where

k_{rf2} : permeability (mD) for class 2 rock-fabric carbonate

ϕ : porosity (percent)

Layer 1 is a 2-ft thick layer with a porosity of 20 percent and a permeability of 70.06 mD. Layer 2 is 5-ft thick layer with porosity values varying from 19 to 7.5%, and permeability values of 11.86 and 0.164 mD in case 1 to 14. The two different thicknesses for layer 1

and 2 are to show the effect of thickness-weighting on averages and the fourteen cases in layer 2 are to show the effect of permeability contrast on different averages. Unweighted and thickness weighted average porosities are calculated by

$$\varphi_{unw} = \frac{\sum_{i=1}^n \varphi_i}{n} \quad (A.2)$$

$$\varphi_w = \frac{\sum_{i=1}^n \varphi_i h_i}{\sum_{i=1}^n h_i} \quad (A.3)$$

unweighted and weighted arithmetic-mean permeabilities are calculated by

$$k_{AM_unw} = \frac{\sum_{i=1}^n k_i}{n} \quad (A.4)$$

$$k_{AM_w} = \frac{\sum_{i=1}^n k_i h_i}{\sum_{i=1}^n h_i} \quad (A.5)$$

unweighted and weighted geometric-mean permeabilities are calculated by

$$k_{GM_unw} = \sqrt[n]{k_1 \dots k_n} = 10^{\frac{\sum_{i=1}^n \log k_i}{n}} \quad (A.6)$$

$$k_{GM_w} = 10^{\frac{\sum_{i=1}^n h_i \log k_i}{\sum_{i=1}^n h_i}} \quad (A.7)$$

where

φ_{unw} : unweighted average porosity (percent)

φ_w : thickness weighted average porosity (percent)

φ_i :	porosity (percent) of layer i
h_i :	thickness (ft) of layer i
k_{AM_unw} :	unweighted arithmetic-mean permeability (mD)
k_{GM_unw} :	unweighted geometric-mean permeability (mD)
k_{AM_w} :	thickness weighted arithmetic-mean permeability (mD)
k_{GM_w} :	thickness weighted geometric-mean permeability (mD)
k_i :	permeability of layer i (mD)

In table A.2, arithmetic and geometric means in permeability were compared to the permeabilities derived from the permeability-porosity correlation (eq. A.7). Because the porosity in the thicker 2nd layer is lower than the 1st layer, thickness-weighted porosities and permeabilities are lower than the unweighted. According to the theory of single-phase fluid flow through porous media, permeabilities of the two-layer systems are the thickness-weighted arithmetic means (highlighted in table A.2). Three averaged permeabilities are plotted with respect to the permeability contrast between two layers in figure A.2.a. This figure shows that permeabilities derived from the permeability-porosity correlation are closer to those from geometric mean than arithmetic mean, and permeabilities from geometric mean and from k - ϕ correlation tend to underestimate the average permeability. Differences in permeability between arithmetic mean and geometric mean or derived from the permeability-porosity correlation (figure A.2.a and b) increase with permeability contrasts between two layers. This difference can be in an order of magnitude or higher in highly heterogeneous, stratified systems.

In figure A.2.c, thickness-weighted arithmetic and geometric means were plotted with respect to thickness-weighted average porosity. Note that in stratified systems permeability values from arithmetic mean do not follow permeability and porosity correlations derived from core data (the curve in figure A.2.c). Arithmetic means (crosses in figure A.2.c) shift from the k - ϕ correlation (curve in figure A.2.c) to the vertical line for fractured systems with the permeability contrast between two layers. The effect of high-permeability layer on permeability in stratified system, similar to the effect of fracture on fractured systems, is to increase permeability sharply compared to the increase in porosity.

To determine general porosity and permeability trends, additional four two-layer models with porosity in layer 1 of 14, 16, 18 and 22 percent were studied. Each model includes seven to ten cases with different porosities in layer 2. Figures A.3.a and b show average permeability from arithmetic mean and ratio of arithmetic mean to geometric mean as functions of permeability contrast between layer 1 and 2. Arithmetic-mean permeabilities of two-layer models decline exponentially from permeability ratio between layers 1 and 2 from 1 to about 50, and then gradually leveled off to asymptotic values (fig. A.3.a). It is interesting to note in fig. A.3.b that ratios of arithmetic to geometric means of five models fall into a single curve as a function of permeability contrast between layers 1 and 2. In reality, the geometric mean will overly underestimate the permeability of the lumped model (which is the arithmetic mean) when the permeability contrast between two layers is great than 10. Figure A.3.c compares average porosity and permeability trends in five two-layer models to the trend from core data (curve in figure A.3.c). Permeabilities in layered systems (figure A.3.c) are dominated by the high-

permeability layers and shift towards fractured systems when the permeability contrast increases. Permeabilities in most 3D models with vertical scales greater than scales of log and core data are commonly controlled by large-scale features such as stratifications, stacking patterns, permeability contrasts among strata, fractures, *etc.*, and are much higher than those calculated from geometric mean and k - ϕ correlations. This explains one of the reasons why permeability values in upscaled simulation models based on geometric average or k - ϕ correlations often need to be increased by an order of magnitude or more during history matching.

Volumetrics

The compound effects of grid vertical resolution and cutoffs on OOIP are complicated and unpredictable. This can be demonstrated using a ten-layer model shown in fig. A.4. This model is to simulate a typical cycle in carbonate which can be divided into two flow unit with a high-porosity unit at the top and low-porosity unit at the base. The 10-layer model is first upscaled to a two-layer flow unit model, and then to a single-layer cycle model. Porosity and permeability values are upscaled using the arithmetic averaging method.

When porosity cutoff of 0.05 is used (fig. A.5.a), two layers with porosity of 0.04 are excluded from the 10-layer model and 80 percent of bulk volume used in volumetrics; the lower flow unit is excluded from flow unit model and only 50 percent of bulk volume is used in volumetrics; and 100 percent of bulk volume is used in volumetrics in the single-layer cycle model. That is to say, among three models the single-layer cycle model calculates the higher volumetrics than the high-resolution ten-layer, and the two-layer flow unit model calculates the least volumetrics. Although OOIP from the high-

resolution is the most realistic but OOIP from the single-layer cycle model can be slightly higher than that from the 10-layer high-resolution model and the two-layer flow-unit model calculates lowest OOIP.

When porosity cutoff of 0.1 is used (fig. A.5.b), five low-porosity layers in the ten-layer model, the lower flow unit in the two-layer model and the entire cycle model are excluded from volumetric calculation.

OOIP is a complex function of grid vertical resolution, petrophysical properties and cutoff values, and how the grid vertical resolution and cutoffs affecting OOIP cannot be predicted. OOIP from high-resolution models are more realistic but not always higher than that from the coarse models.

Table A.1. Parameters used in a two-layer model for the case study.

Case No.	Layer No.	Thickness (ft)	Porosity (%)	Permeability (mD)	Permeability ratio
	1	2	20	70.055	
1	2	5	19	51.040	1
2	2	5	18	36.555	2
3	2	5	17	25.686	3
4	2	5	16	17.667	4
5	2	5	15	11.861	6
6	2	5	14	7.747	9
7	2	5	13	4.903	14
8	2	5	12	2.991	23
9	2	5	11	1.748	40
10	2	5	10	0.971	72
11	2	5	9	0.506	138
12	2	5	8.5	0.356	197
13	2	5	8	0.245	286
14	2	5	7.5	0.164	426

Table A.2. Results of average porosities and permeabilities of fourteen cases of a two-layer model.

Case No.	Permeability ratio	Porosity (frac)	Permeability (mD)			Permeability ratio	
			AM	GM	k-poro	AM/GM	AM/(k-poro)
unweighted	1	19.50	60.55	59.80	59.92	1.01	1.01
	2	19.0	53.31	50.61	51.04	1.05	1.04
	3	18.5	47.87	42.42	43.29	1.13	1.11
	4	18.0	43.86	35.18	36.56	1.25	1.20
	5	17.5	40.96	28.83	30.72	1.42	1.33
	6	17.0	38.90	23.30	25.69	1.67	1.51
	7	16.5	37.48	18.53	21.36	2.02	1.75
	8	16.0	36.52	14.48	17.67	2.52	2.07
	9	15.5	35.90	11.07	14.52	3.24	2.47
	10	15.0	35.51	8.25	11.86	4.31	2.99
	11	14.5	35.28	5.96	9.62	5.92	3.67
	12	14.3	35.21	4.99	8.64	7.05	4.07
	13	14.0	35.15	4.14	7.75	8.49	4.54
	14	13.8	35.11	3.39	6.93	10.35	5.07
h-weighted	1	19.3	56.47	55.87	55.97	1.01	1.01
	2	18.6	46.13	44.02	44.33	1.05	1.04
	3	17.9	38.36	34.21	34.80	1.12	1.10
	4	17.1	32.63	26.19	27.05	1.25	1.21
	5	16.4	28.49	19.70	20.80	1.45	1.37
	6	15.7	25.55	14.53	15.81	1.76	1.62
	7	15.0	23.52	10.48	11.86	2.24	1.98
	8	14.3	22.15	7.36	8.78	3.01	2.52
	9	13.6	21.26	5.02	6.39	4.24	3.33
	10	12.9	20.71	3.30	4.58	6.28	4.52
	11	12.1	20.38	2.07	3.22	9.84	6.33
	12	11.8	20.27	1.61	2.68	12.59	7.57
	13	11.4	20.19	1.23	2.21	16.39	9.12
	14	11.1	20.13	0.93	1.82	21.72	11.07

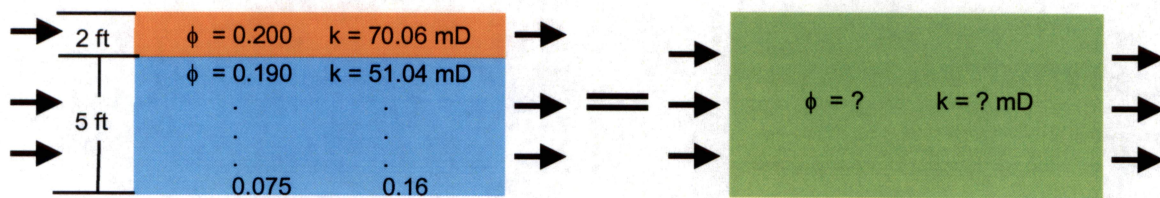


Figure A.1. Schematic diagram showing upscaling of two-layer models and associated layer properties.

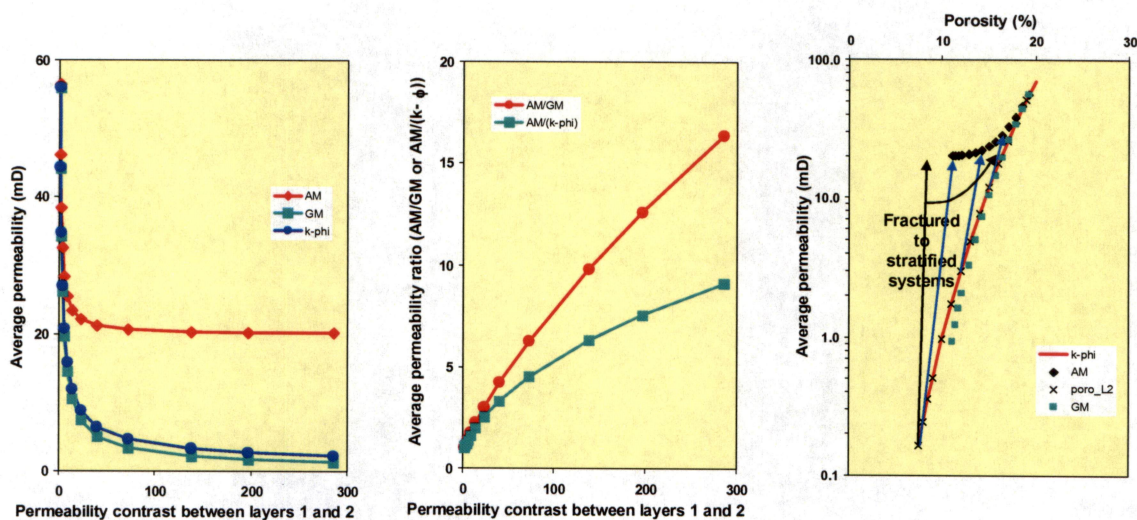


Figure A.2. Relationships among average permeability values of a two-layer system: (a) average permeabilities calculated by arithmetic mean, geometric mean and k-porosity correlation vs. permeability contrast between layer 1 and 2, (b) average permeability ratio between arithmetic and geometric means (red curve) and between arithmetic mean and permeability derived from k-porosity correlation as a function of permeability contrast between two layers, and (c) average permeability vs. average porosity.

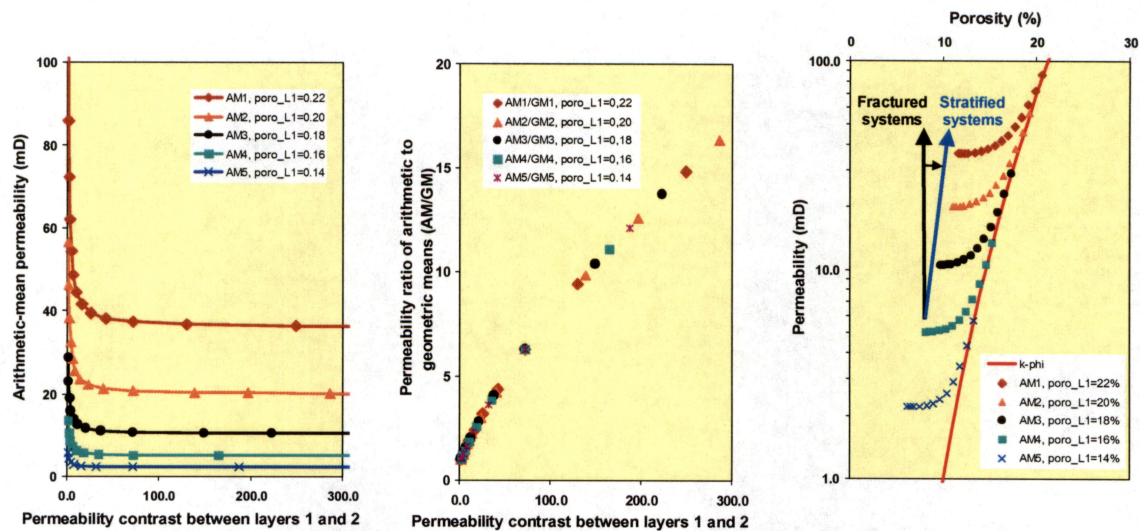


Figure A.3. Average permeabilities in two-layer systems: (a) average permeability vs. permeability contrast between layer 1 and 2, (b) average permeability ratio between arithmetic and geometric means (red curve) and between arithmetic mean and permeability derived from k-porosity correlation as a function of permeability contrast between two layers, and (c) average permeability vs. average porosity.

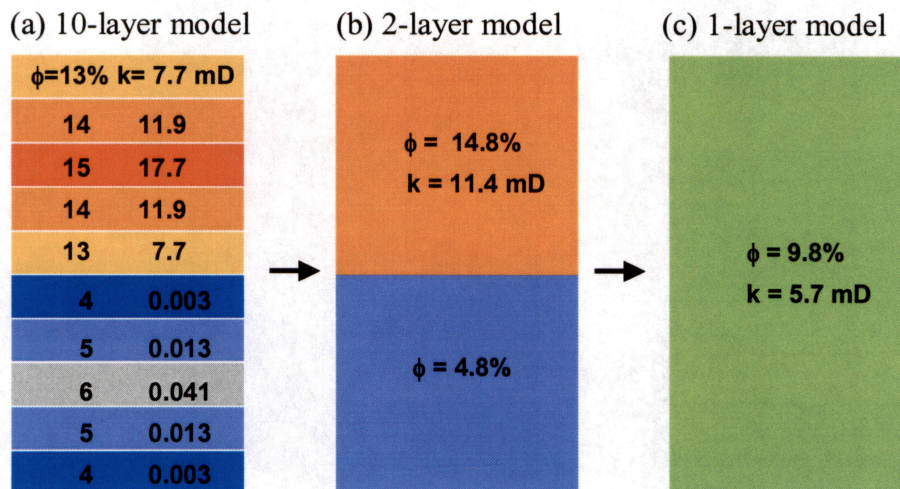
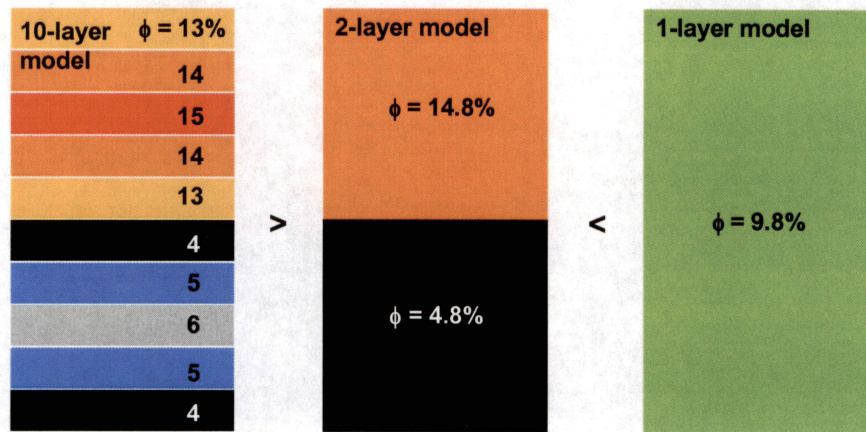


Figure A.4. Schematic diagram showing upscaling associated layer properties of ten-layer model to a two-layer flow unit model, and to a single-layer cycle model.

(a) Porosity cutoff = 5%



(b) Porosity cutoff = 10%

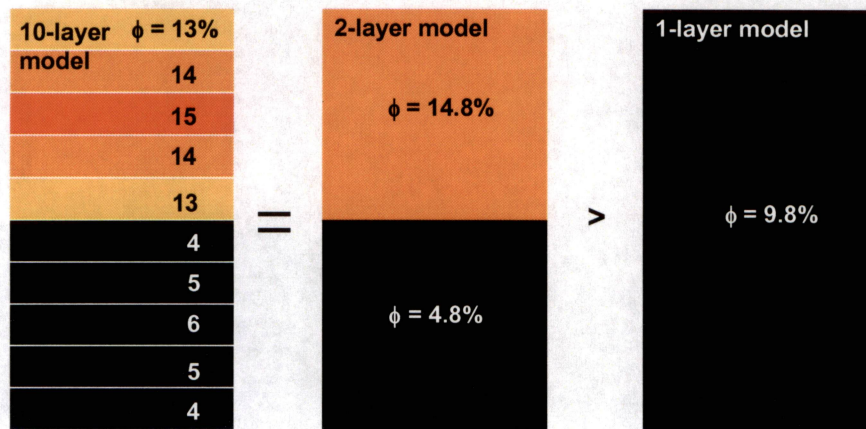


Figure A.5. Schematic diagram showing effect of porosity cutoffs of (a) 0.05 and (b) 0.10 on upscaling associated layer properties of ten-layer model to a two-layer flow unit model, and to a single-layer cycle model.

**CONSTRUCTION AND ANALYSIS OF 3-D SEISMIC
POROSITY INVERSION MODELS**

Hongliu Zeng

**Bureau of Economic Geology
Scott W. Tinker, Director
John A. and Katherine G. Jackson School of Geosciences
The University of Texas at Austin
Austin, Texas 78713-8924**

ABSTRACT.....	309
INTRODUCTION	309
METHODOLOGY	311
DATA AND TIE.....	313
IMPROVEMENT OF SEISMIC DATA INTERPRETABILITY.....	314
90°-phasing	314
High-frequency Signal Enhancement	315
WELL-BASED AI MODEL.....	316
MODEL-BASED SEISMIC INVERSION.....	317
Why Model-based?	317
How Well and Seismic Data Are Integrated	319
PROGRESSIVE INVERSION	320
Problems in Model-based Inversion	320
Solution.....	322
Blind Test.....	324
CONCLUSIONS.....	325
REFERENCES	326

Figures

1. Location of well and seismic data in Fullerton field, Andrews County, Texas, and 3-D seismic inversion area around Phase 2 area.....	327
2. Synthetic seismogram of lower Clear Fork and Wichita and surrounding formation in well Cal/Mon 1 across 2-D seismic line 0123	328
3. Linear relationship between AI and log porosity of carbonate rocks in the lower Clear Fork and Wichita, Fullerton field, Andrews County, Texas.....	328
4. A 0°-phase seismic section (trace 2382) in the 3-D survey area showing poor tie between high-porosity/low-AI units and amplitude/polarity and difficulty in picking high-frequency sequence boundaries.....	329

5. A 90°-phase seismic section (trace 2382) in the 3-D survey area showing improved tie between high-porosity/low-AI units and amplitude/polarity	330
6. A high-frequency-enhanced (spectral-balanced) version of Figure 5 showing improvement in seismic resolution	331
7. Wireline log-based AI models for reservoir characterization and seismic inversion.....	332
8. Procedure of a model-based inversion.....	333
9. Model based inversion from background model, blocky model, smoothed log model, and log model.....	334
10. Differences of AI inversion corresponding to different initial model inputs	335
11. Initial models for progressive inversion	336
12. Progressive inversion.....	337
13. Differences of stratigraphic framework used in initial model construction	338
14. Difference in AI estimation through progressive inversion.....	339
15. Blind test showing value and limit of progressive inversion (example 1)	340
16. Blind test showing value and limit of progressive inversion (example 2)	341
17. Blind test showing value and limit of progressive inversion (example 3).....	342

Construction and Analysis of 3-D Seismic Porosity Inversion Models

Hongliu Zeng

ABSTRACT

Geology-guided reconditioning of seismic data is the key to improve extraction of relevant geologic information. At Fullerton field, the most convenient and useful tools for data reconditioning are phase shifting and high-frequency enhancement. A simple seismic phase rotation (to 90°) reconditions seismic data for impedance representation, roughly linking seismic amplitude directly to log lithology and porosity and making stratigraphic correlation more accurate. High-frequency enhancement raises the dominant frequency of 3-D seismic data from 30 to 50 Hz, significantly improving seismic resolution. More accurate and finer scale seismic mapping of reservoir parameters is achieved from model-based, progressive inversion that seamlessly integrates the geologic interpretation of well-seismic data and model-based seismic inversion for high-resolution (2 ft) impedance models.

INTRODUCTION

Post-stack seismic data contain rich information about reservoir stratigraphy, sedimentology, and physical properties. The value of seismic interpretation and well-seismic integration has long been recognized. Higher purposes of interpretation include (1) to establish a direct link between subsurface geology and seismic signal by making seismic expression resemble to geologic section (structure, stratigraphy, lithology, rock properties, etc.), and (2) to extract the highest possible resolution information from seismic processing and from integration of well data. However, our current seismic interpretation strategies fall short for these higher

purposes by emphasizing more on structural mapping and less on stratigraphic evaluation. Stratigraphic information in seismic data is far from being fully utilized because of the lack of thorough understanding of the relationship between stratigraphy and its seismic responses, regularly poorly conditioned seismic data that fail to express the stratigraphy in a way geologists can understand, and the gap in well and seismic resolution and difficulties in data integration. Better methods of stratigraphy-oriented data reconditioning and integration are the goal of this study.

In this report we describe a systematic approach to the better seismic stratigraphic interpretation. The first step in this approach is basic data reconditioning within seismic frequency range (5-70 Hz in this study) to improve seismic data interpretability. Two key techniques were applied: phase rotation and high-frequency enhancement. A simple seismic phase rotation (to 90°) reconditions seismic data for impedance representation, roughly linking seismic amplitude directly to log lithology and porosity. High-frequency enhancement raises the dominant frequency of 3-D seismic data from 30 to 50 Hz, significantly improving seismic resolution.

However, there is a limit to the improvements that can be achieved in seismic data interpretability possible from basic data reconditioning. For example, the 90°-phasing does not eliminate the wavelet effect. To remove wavelet sidelobes for truer representation of geology it is also necessary to perform a seismic inversion. Furthermore, there are limits to the resolution obtainable from the high-frequency enhancement. A high-frequency enhancement processing does not result in the resolution high enough for reservoir flow model construction. To reach the levels of high resolution needed for flow modeling, it is necessary to employ well data. Inversion without use of constraining well data will not provide reservoir details beyond seismic

resolution. To solve this problem, we developed a more advanced data reconditioning method called progressive inversion. With this approach which is described in this report, more accurate and log-resolution (2 ft) seismic mapping of reservoir parameters can be achieved.

METHODOLOGY

We emphasize on stratigraphy-oriented 3-D seismic data interpretation by addressing the use of following three techniques:

1. Seismic phase adjustment to layer-based event expression. Standard seismic processing usually produces (or at least attempts to produce) 0°-phase seismic data as the final product. Interpretive advantages of 0°-phase data include wavelet symmetry, center lobe (maximum amplitude) coincidence with reflection interface, and higher resolution (Brown, 1991). However, those advantages of 0°-phase data are realized only if the seismic reflection comes from a single reflection interface. More often we have to deal with seismically thin beds where reflection amplitudes are composite seismic responses from the top and the base. In this situation, the observed waveform is a peak-trough couplet. Because seismic events do not necessarily coincide with bed geometry, it can be difficult tying lithology/porosity logs in wells to seismic data, especially when multiple thin beds co-exist in a stratigraphic interval. Ninety-degree-phase data are more suitable for geologic interpretation of seismically thin beds (Zeng et al., 1996, 2003, 2004; Zeng, 2003). The use of a 90°-phase wavelet overcomes the shortcomings of the 0°-phase wavelet by shifting the main lobe (maximum amplitude) of the seismic response to the center of the thin bed. The seismic response is symmetrical to the thin bed, instead of to the top and base of the bed, which makes the main seismic event (a trough, in this case) coincide with the geologically defined high-frequency sequences and flow units. As a

result, seismic polarity/amplitude is uniquely tied to stratigraphy. These improvements, when applied to real data, can make seismic interpretation easier.

2. High-frequency enhancement. By relatively suppressing low-frequency components and enhancing high-frequency components in the data, seismic resolution can be further improved. However, the processing will inevitably reduce the signal-to-noise ratio of the data. As a result, there are still arguments on whether and how useful the technique is. Our experience indicates that the technique is valuable in enhancing the thin-bed imagery if without over-boosting high-frequency noise beyond effective signal bandwidth. There are several methods to achieve high-frequency signal enhancement, such as frequency filtering and deconvolution (Yilmaz, 1987), and spectral balancing (Tufekcic et al., 1981). For this study, spectral balancing was used to relatively enhance the high-frequency energy in the data without over-whitening the spectrum.
3. Combine well and seismic data for full spectrum reservoir modeling. Well data integration is necessary to build a high-resolution reservoir simulation model from seismic data. The difficulty is how to calibrate data of different scale and different resolution in both geologically and computationally reasonable and seamless way. Departing from current trend of concentrating on geophysical algorithms, we emphasize the role of geologists in interpretation-oriented processing such as seismic inversion. With a close involvement of geologists, integration (in the form of inversion) is typical not one-time process. Zeng et al. (2003) demonstrated that a progressive (or repeated) inversion can considerably improve the quality of reservoir modeling. By upgrading initial model from previous inversion and geologic knowledge for subsequent inversion,

the progressive inversion can combine and calibrate well and seismic data more efficiently and accurately.

DATA AND TIE

Data for this study come from the Fullerton Clear Fork field in Andrews County, Texas (Figure 1). The Fullerton Clear Fork reservoir comprises shallow water carbonates of Lower Permian (Leonadian) age at a depth of about 6,600 to 7,500 ft. Available data for the field study include wireline logs ($\pm 1,400$ wells), cores (approximately 15,000 ft), 3-D seismic (26 mi^2) and 2-D seismic data (30 lines). This study focused on the central part of the field and utilized approximately 5 mi^2 3-D seismic and 66 well log suites.

Well to seismic ties using synthetics is straightforward at Fullerton field. For example, in well Cal/Mon 1, a seismogram was generated with a sonic log (Figure 2). The seismogram ties very well to a 2-D seismic line across the well (line 0123). From well-log interpretation, we can easily pick Tubb and Abo reflectors from the seismic data, which form the top and base of the lower Clear Fork and Wichita reservoir section, respectively. Synthetics in other wells in the field (both in 2-D and 3-D seismic area) exhibit similar results.

Petrophysical analysis of wireline logs shows a linear relationship between acoustic impedance (AI) and calculated porosity. Although a spectrum of limestones and dolostones—from grain-dominated to mud-dominated dolostones—and anhydrite have been observed in conventional cores, the log AI steadily decreases with log porosity at fairly high correlation ($\rho=0.88$) in a depth range of 6,600 to 7,300 ft (Figure 3). This close relationship between AI and porosity implies that seismic amplitude should be a good indicator of porosity, provided that amplitude tuning effects can be reasonably estimated with well control.

However, the observed excellent well log-to-seismic tie and the simple acoustic relationship do not automatically lead to an easy interpretation of seismic data, especially in terms of stratigraphy and porosity. Figure 4 shows a standard, 0°-phase seismic section tied to well logs. Note that only major stratigraphic boundaries (Tubb, Wichita, and Abo, solid lines, Figure 4) are linked to prominent seismic events. High-frequency sequence boundaries (HFS2.1-HFS2.3, Wichita 8, Figure 4) are not resolved by seismic and cannot be correlated based on seismic phase. Low-AI or high-porosity zones in high-frequency sequences (dashed lines, Figure 4) recognized in sonic/density and porosity logs tie neither to polarity nor to amplitude. A similar situation is seen in other seismic data volumes (2-D and 3-D) in the project area. This observation suggests that the seismic data are not in the best form for stratigraphic interpretation and must be reconditioned and reprocessed before being put into use.

IMPROVEMENT OF SEISMIC DATA INTERPRETABILITY

Simple post-stack processing tools are available in various seismic interpretation packages (e.g., Poststack in Landmark). A quick improvement of data interpretability can be achieved by applying appropriate data processing techniques for better stratigraphically-oriented seismic interpretation. Our tests show that seismic phase adjustment and high-frequency enhancement are two of the most useful tools.

90°-phasing

As seen in Figure 4, standard 0°-phase seismic data is not optimal for stratigraphically oriented, thin-bed interpretation. To improve the data interpretability, the 0°-phase seismic data in Figures 4 were reprocessed by applying a 90° phase shift (Figure 5). In this reprocessed seismic section, the important stratigraphic boundaries (Tubb, Wichita, and Abo) are tied to

seismic events with a 90° phase shift (zero crossings, Figure 5). Although the high-frequency sequence boundaries still fail to correlate to specific seismic phase characters, high-porosity zones (low AI) associated with some of them (dashed lines, Figure 5) tend to tie to seismic trough events (negative amplitude). The resolution, though, is dominated by the low dominant frequency of the data (around 30 Hz), which causes some thinner porosity zones to be imaged as merged seismic events without clear separation.

Apparently, the 90° phasing of seismic data reconditions seismic traces to better resemble an impedance profile so that the interpretability of the data is improved. The procedure is simple, reliable, and not data damaging.

High-frequency Signal Enhancement

Although 90° phasing significantly improves the visual correlation between seismic events and stratigraphic units (Figure 5), the resolution of seismic data is still not satisfactory. It is still difficult to map individual thin porosity zones in high-frequency sequences because of the frequent merging of seismic events following these closely spaced units. To improve the seismic resolution, a spectrum balancing processing was applied to the data (Figure 6). After the processing, the dominant frequency of 3-D seismic data was raised from about 30 to 50 Hz. As a result, seismic events are shorter in time and are better separated on seismic sections. Eventually, seismic separation between thin porosity zones becomes more clear (compare Figure 5 and Figure 6).

Even though a high-frequency enhancement processing raises the noise level in the data to a certain degree so that the signal-to-noise ratio of the data is somewhat reduced, the new seismic data set provides better definition of major reservoir units in the field. With this increased resolution, structural mapping for major stratigraphic boundaries (Tubb, Wichita, and

Abo) and attribute extraction for thin porosity zones in high-frequency sequences can be performed in the entire study area. However, seismic resolution is still not enough for seismic correlation of high-frequency sequence boundaries and flow-unit level reservoir units because of the lack of seismic information beyond 70 Hz.

WELL-BASED AI MODEL

To further improve reservoir interpretation and modeling, well data must be integrated. Cores and wireline logs provide not only measurements of lithology, facies, and rock properties, but also high-resolution (down to 0.5 ft) correlation of geologic and flow units that is beyond seismic control. It is important to use well information to the fullest extent possible. At current stage of seismic reservoir characterization, this means to construct the best possible high-frequency sequence stratigraphic and high-resolution AI models from well data to guide data integration (inversion).

Based on construction methods and output model resolution, there are four basic model types (Figure 7),

1. Background model (Figure 7a). Only a low-frequency AI trend is calculated from well AI logs. High-frequency sequence boundaries and all details in well AI logs are omitted.
2. Blocky model (Figure 7b). AI values are averaged for each layer defined by horizons (high-frequency sequence boundaries) picked from well and seismic data. In this model, horizons are usually seen as sharp AI boundaries because of the blocky effect. Unpicked, internal geologic surfaces are omitted in AI mapping. Resolution depends on horizon density and is typically lower than seismic resolution.

3. Smoothed log model (Figure 7c). AI values between wells follow filtered well log trends within the interpreted stratigraphic framework. Resolution is variable. In this case, the model resolution is adjusted to seismic resolution (<70 Hz).
4. Log model (Figure 7d). AI values are modeled in log resolution (down to 1.25 ft). Thin beds between wells are linearly interpolated between successive pairs of horizons. As a result, modeled reservoir geometry and architecture are very sensitive to the stratigraphic framework provided.

These models (Figure 7a to 7d) utilize increasingly detailed well data information. The degree of geologist's involvement, through interpretation of stratigraphic framework and reservoir architecture used in the models, also increases. For best possible integration, it is important to construct and use well-based AI models at log-resolution level.

MODEL-BASED SEISMIC INVERSION

To achieve the integration of well and seismic data in reservoir modeling is equivalent in geophysical terms to completing three tasks: (1) remove wavelet effect, (2) restore low-frequency AI trend, and (3) combine high-frequency (high-resolution) well AI information. An appropriate seismic inversion can accomplish all three in a seamless and efficient manner.

Why Model-based?

From the geophysical literature, there are four main types of inversion:

1. Recursive inversion. Assuming a seismic trace as a reflection coefficient series, AI can be calculated by recursively solving the reflection coefficient equation. In this process, the wavelet effect is not removed and well data are not involved except to provide a low frequency trend. The results are commonly poor.

2. Sparse spike inversion. This method finds major reflection interfaces (spikes) that have a significant contribution to a seismic trace by inserting reflection interfaces at proper positions for the best fit of synthetics and real seismic traces. Minor reflection interfaces are ignored. As a result, inversion is low frequency in nature. Wavelet effect is reduced. The detailed well data, however, cannot be combined into output in this process.
3. Neural network inversion. An artificial neural network can be trained to find nonlinear correlations between seismic attributes and AI (or an appropriate rock property of interest). With this process, wavelet effect can be reduced by forced calibration of seismic traces to wireline logs. The resolution, though, is still limited to the seismic frequency range.
4. Model-based inversion. Also called Generalized Linear Inversion (GLI), this approach requires input of an initial (or guess) AI model. The initial model is typically constructed from available well and seismic data. If the initial model is built such that the full spectrum (low frequency, seismic frequency, and high frequency) of information is included, the inversion process will modify the model at the seismic frequency range by minimizing error functions between synthetics and seismic traces and let the low frequency trend and the high frequency details from well interpretation carry through to the final model. Model-based inversion is the most popular inversion package in the industry (e.g., Hampson-Russell, Jason, and CGG).

Only the model-based inversion offers us a platform to build a full-spectrum reservoir model in a single process that combines all available information. The model-based inversion method is the approach used at Fullerton field study.

How Well and Seismic Data Are Integrated

A model-based inversion (e.g., in Hampson-Russell Strata) is typically an iterative process (Figure 8):

1. Construct an initial AI model trace;
2. Create synthetics using the estimated AI trace and extracted wavelet;
3. Calculate the difference between the synthetics and real seismic trace. If the error is within the tolerance level, output the AI trace as inversion model; otherwise compute objective function and model perturbation, update the AI trace, and go back to step 1.

Because the initial model is seldom perfect, the process must commonly be repeated multiple times.

The optimization aims at fitting a model-generated synthetic seismogram to its real seismic counterpart. The process is restricted to the seismic frequency range in the real data. Any frequency components beyond seismic in the initial model (both low and high frequencies) are filtered out in the synthetics by the extracted wavelet, and cannot influence the optimization. If the restraints to output AI are set loosely enough, those model components beyond seismic frequency range tend to carry through to updated AI models and the final inversion.

As an example, Figure 9 shows four versions of inversion results from the four different initial models in Figure 7. Although the same seismic line and well data were used to build the initial models, the inversion can be quite different. A background model (Figure 7a) brings the least geologic information (low-frequency trend only) and inversion is mainly controlled by seismic frequency (Figure 9a). A blocky model (Figure 7b) introduces major geologic layering controlled by high-frequency sequence-scale horizons. The inversion (Figure 9b) emphasizes horizontal continuity at and near the sharp impedance boundaries at these geologic boundaries

and can be biased. A smoothed log model (Figure 7c) better follows AI trend defined by well logs and therefore better honors geologic knowledge (both stratigraphic framework and AI distribution). The inversion, however, still lacks details beyond seismic frequency range. Differences in inverted AI for the first three inversions are shown in Figure 10. In some intervals (e.g., intervals between HFS2.2 and HFS2.3 and between Wichita and Wichita 8) 25% variation in inverted AI is observed among the three inversions, although all the inversions fit seismic data equally well. Finally, an introduction of high-frequency log data to the initial model (Figure 7d) leads to a high-resolution inversion (Figure 9d). The similarity of the model and the inversion is a result of carry-through of high-frequency AI components from the model to the inversion. The inversion, however, still incorporates a seismic signal at the seismic frequency range, which modifies size, continuity, and AI value for many of the thin reservoir units in the initial model.

PROGRESSIVE INVERSION

Problems in Model-based Inversion

Assuming good-quality well and seismic data and a correct implementation of inversion software, many factors can still influence the quality of inversion because of the nonuniqueness of inverse problems. Geophysicists tend to concentrate more on improving optimization algorithms. Vigorous model testing indicates that when a good, geologically-constrained model is used, a regular optimization algorithm (e.g., conjugate-gradient algorithm in Hampson-Russell) should yield satisfactory results. On the other hand, model quality is equally important. A bad model will lead to a bad inversion, even if a most sophisticated optimization algorithm is applied. In this study, model quality is our major concern.

From the geologist's point of view, a high-quality initial model is created by deriving the most detailed and the most accurate stratigraphic framework possible from available well and

seismic interpretation, and then spatially populating AI within the framework in a geologically and statistically reasonable way. In this study, the accuracy of the stratigraphic framework was the key issue. Although varying approaches to interwell mapping can play an important role in model construction, a discussion of attribute mapping is beyond the scope of this study. All well data were mapped between and beyond wells following inverse square distance rule, a popular choice in the industry.

In the final analysis, the task of performing a good model-based inversion is reduced to a surface picking issue. The biggest challenge is that it is very difficult, if not impossible, to build an accurate high-resolution initial model by interpreting closely spaced stratigraphic surfaces between and beyond the wells from low-resolution seismic data (Figure 4-6). In this seismic data volume, good horizons that can be at least approximately tied to geologic surfaces are limited (e.g., Top Tubb, Tubb, and Wichita, Figure 11). However, these surfaces alone are typically not enough to accurately define the stratigraphic model. Picked geologic surfaces (e.g., Wichita, Figure 6) may offset seismic events (in this case, a peak-to-trough zero crossing) because of seismic interferences or misperception in interpretation. High-frequency and cycle boundaries commonly are not resolved and cannot be picked directly from low frequency seismic section (e.g., HFS2.1, 2.2, and 2.3, and Wichita 8, Figure 6). Without sufficient good-quality surfaces mapped, the initial model is almost always oversmoothed and poor in quality. To make things worse, most people use this poor initial model once and only once in the inversion process and never revisit. As a result, significant error/uncertainty in model building tends to carry through to the final inversion product.

Solution

Progressive inversion improves model-based inversion by progressively building multiple initial models and performing multiple inversions (Figure 8). The first initial model should be a low-resolution model based on a small number of prominent and reliable geologic boundaries and seismic horizons. The first inversion is performed on the basis of this initial model, which reduces wavelet effect and usually reveals more geologic detail than the original seismic data. Horizons are then reinterpreted by comparing seismic data and the first inversion. Additional horizons are then added from interpretation of the seismic data and the first inversion to create a new and more accurate initial model that fits geologic expectations. A new inversion based on this improved initial model will provide yet more accurate geologic details. This process may be repeated until inversion is satisfactory for reservoir model building applications.

For this study, a progressive inversion was performed with Hampson-Russell inversion software (Figures 11-13). The first inversion was done using an initial impedance model (Figure 11a) made from a single seismic horizon, Top Tubb, one of the most prominent geologic boundaries in the wells that show the best tie to the seismic data (Figure 6). By using only one horizon, we assume a sheet-like formation without lateral thickness variation. The result (Figure 12a), as expected, is less than desired because of the poor geologic control on the initial model. However, compared to seismic data (Figure 6) the inversion does a better job of resolving other geologic boundaries. A second horizon, Wichita, was added to build a new initial model (Figure 11b). Improving stratigraphic control, this two-horizon-based model was used to perform a second-round inversion (Figure 12b). Following the same procedure, another two rounds of inversion were completed. The fourth-round inversion (Figure 12c) was performed by using a seven-horizon-based initial model (Figure 11c), which utilized all high-frequency sequence

boundaries recognizable from interpretation of well data, seismic amplitude data, and intermediate inversion results as far.

A key improvement achieved from progressive inversion is the introduction of increasingly more accurate stratigraphic framework by using more and more horizons. As shown in Figure 13, the seven horizons used in the final-round inversion provide the most detailed stratigraphic correlation based on wireline log, core, and seismic analysis. As a result, thickness variations in each of the high-frequency sequences are easily modeled, which potentially has significant influence on definition of reservoir architecture and flow units in the model. In this study, the use of fewer control horizons in the first- and second-round inversions (Figure 13 a, b) introduced a correlation error ranged at 0-50 ft that is more than enough to produce the mis-correlation of flow units between wells. Some of the mis-correlation can be identified by comparing the early-generation model to a later-generation model (Figure 11, AA', BB', CC' and DD'). These mis-correlations, unfortunately, carried through to inversions (Figure 12, AA', BB', CC' and DD'). The mis-correlation can also be illustrated by the AI differences in successive rounds of inversion (Figure 14). At or near the wells, the models generated similar results (white, vertical strips in Figure 14a, b). Away from the wells, however, improvements in thin-bed definition from fine-tuning geologic surface picking and adding more geologic surfaces lead to significant changes of AI distribution (high-frequency bands in Figure 14a, b), although all three inversions fit seismic data equally well. The final (fourth round) inversion provides the best fit between geologic interpretation and seismic signal.

Progressive inversion is a seamless way to integrate geologic knowledge and seismic processing for reservoir characterization purpose. It requires an intimate involvement of geologists in seismic inversion. A sequence stratigraphic model provides guidance on how

seismic correlations should be carried out between and beyond wells for initial guess model construction using well impedance logs. In the study area, the geologic model indicates that all HFS-level seismic picks in the lower Clear Fork and Wichita should be relatively flat because the succession was deposited on a flat shallow-water platform (Ruppel, 2003). A comprehensive study of core, logs, and seismic data further established a high-frequency sequence stratigraphic framework at all well locations (Ruppel and Jones, this report). Initial and intermediate inversion results allow correlation of high-frequency sequence boundaries between and beyond well locations that honor both well picks and seismic trends. Multiple seismic/geologic picks in a short time window (in this case seven horizons in 100 ms) transfer detailed *a priori* stratigraphic information to seismic inversion, achieving impedance models that exceed expectations if using well or seismic data alone.

Blind Test

To demonstrate the value and limit of seismic signal and progressive inversion, nine wells were withheld from the 66-well data base to recreate the seven-horizon initial AI model. A new inversion was then done following the same procedure and parameter setup. Results of these tests are displayed in Figures 16-18. In each case, the original inversion is compared with inversions made after wells have been removed. There are two major observations,

1. Seismic can supply important missing geologic information between and beyond well control. Figure 15a and 15b show the effect of removing a well from model. Note that a high-porosity zone (A) and a low porosity zone (B) (Figure 15a) are not imaged by the model when the well is removed (Figure 15b). By contrast, the inversion does an excellent job of imaging the high-porosity zone (A) and the low porosity zone (B) despite the missing well. Figure 15d (the inversion with a missing well) compares quite well with

both the original log model (Figure 15a) and the inversion based on the original log model (Figure 15c). In other words, the inversion can provide a good image of reservoir character where well control is missing. Figures 16 and 17 show two more examples of the ability of inversion to define porosity in areas of less well control.

2. High-resolution details in the inversion are imperfect. Seismic signal is low frequency in nature, with a resolution no better than a quarter wavelength (approximately 20 m in this case). The high-resolution layering (1 ft in the initial model and 2 ft in the inversion) is defined by well AI logs within stratigraphic framework between and beyond wells. Seismic inversion adjusts AI distribution without changing the thickness architecture. Unfortunately, in this study, only the simplest attribute mapping was conducted between and beyond wells: thin-bed thickness is proportional to interval thickness between horizons; AI distribution in each bed is predicted by inverse square distance rule. As the result, the error in thin-bed thickness and AI mapping is not trivial, leading to an imperfect AI estimation. As a result, inversions with or without missing wells show somewhat different details near the well location (Figures 15-17). Some isolated thin beds are totally unrepresented without using of the missing wells. To further improve the inversion, an effort has to be made to develop more advanced mapping algorithms beyond the proportional layering and inverse square distance rule.

CONCLUSIONS

1. Post-stack seismic data are commonly not in optimal form and require reconditioning before they can be used for stratigraphic analysis and reservoir characterization.
2. Basic data conditioning applies do-it-yourself poststack processing tools to improve data interpretability and resolution. A 90°-phasing adjusts seismic traces to resemble

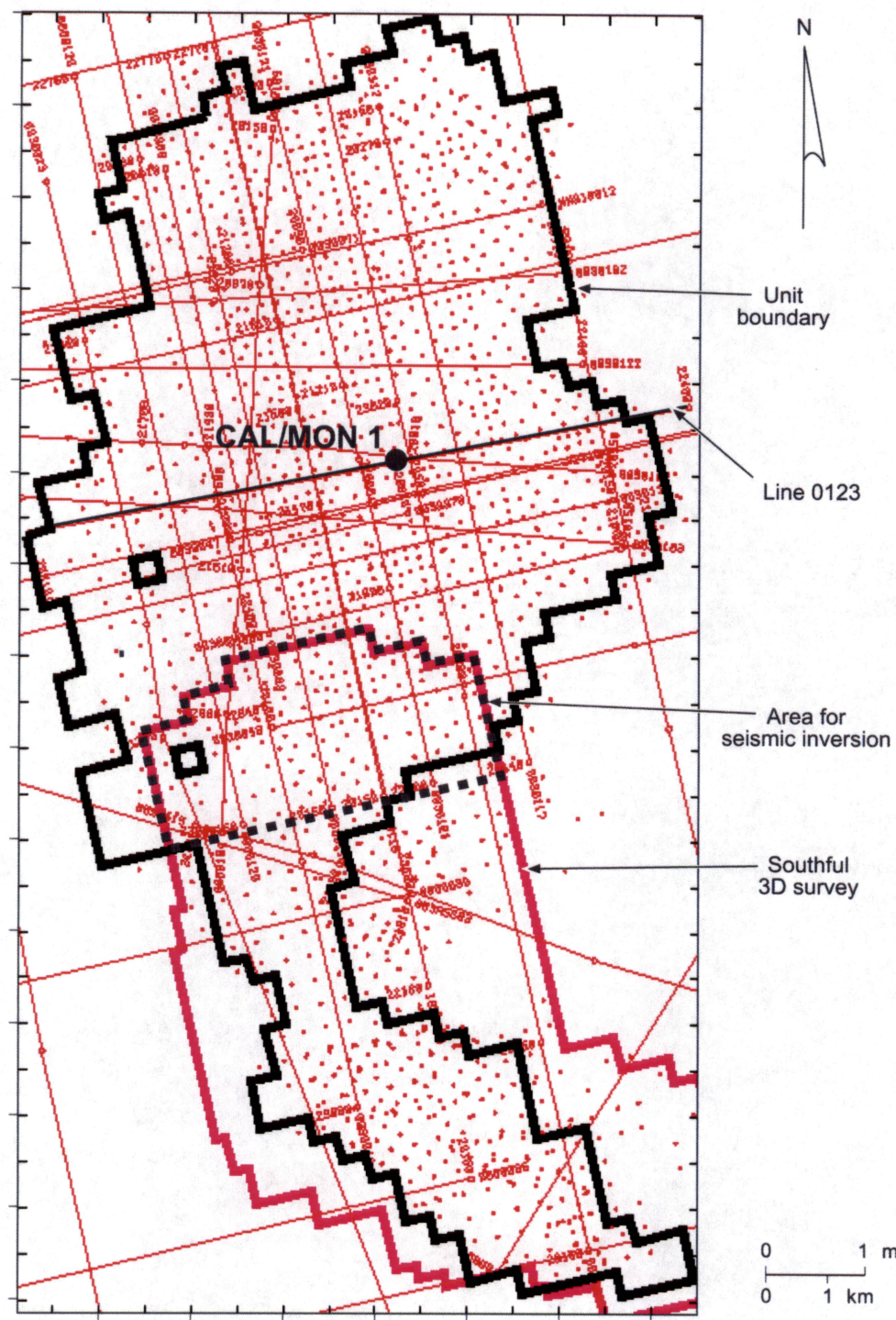
impedance logs; a high-frequency enhancement enables interpreters to identify more and thinner geologic units (at 100-ft resolution level).

3. Progressive seismic inversion can provide a good representation of reservoir porosity in areas of missing or poor quality log data.
4. Progressive seismic inversion requires involvement of geologists by providing a geologic model and quality-checking seismic picking of high-resolution geologic boundaries.

Progressive inversion promises to seamlessly integrate geologic knowledge and seismic data for detailed impedance modeling down to wireline log resolution.

REFERENCES

- Brown, A. R., 1991, Interpretation of three-dimensional seismic data: Tulsa, Oklahoma, AAPG Memoir 42, 3rd edition.
- Ruppel, S. C., 2003, Lower Leonardian (Clear Fork – Abo) Reservoir Architecture: Insights From Outcrops And Fullerton Clear Fork Field, West Texas: WTGS Fall Symposium, Back to Basics: : West Texas Geological Society Fall Symposium: West Texas Geological Society Publication #03-112, p.45-46.
- Tufekcic, D., J. F. Claerbout, and Z. Rasperic, 1981, Spectral balancing in the time domain: Geophysics, v. 46, no. 8, p. 1182–1188.
- Yilmaz, O., 1987, Seismic data processing: Society of Exploration Geophysicists. 526 p.
- Zeng, Hongliu, 2003, Significance of seismic phase in interpretation of stratigraphy and sedimentology (abs.), *in* Partners in a new environment: CSPG/CSEG Convention, June 2–6, Calgary, Alberta, Canada, unpaginated, CD-ROM.
- Zeng, Hongliu, Backus, M. M., Barrow, K. T., and Tyler, N., 1996, Facies mapping from three-dimensional seismic data: potential and guidelines from a Tertiary sandstone-shale sequence model, Powderhorn field, Calhoun County, Texas: AAPG Bulletin, 80, no.1, 16-46.
- Zeng, Hongliu and Hentz, T. F., 2004, High-frequency sequence stratigraphy from seismic sedimentology: applied to Miocene, Vermilion Block 50-Tiger Shoal Area, offshore Louisiana: AAPG Bulletin, 88, no. 2, 153-174.
- Zeng, Hongliu, Ruppel, S. C., and Jones, R., 2003, Reconditioning seismic data for improved reservoir characterization, lower Clear Fork and Wichita, Fullerton field, West Texas, *in* T. J. Hunt and P. H. Lufholm, eds., The Permian Basin: back to basics: West Texas Geological Society Fall Symposium: West Texas Geological Society Publication #03-112, 67-78.



QAd4045x

Figure 1. Location of well and seismic data in Fullerton field, Andrews County, Texas, and 3-D seismic inversion area around Phase 2 area.

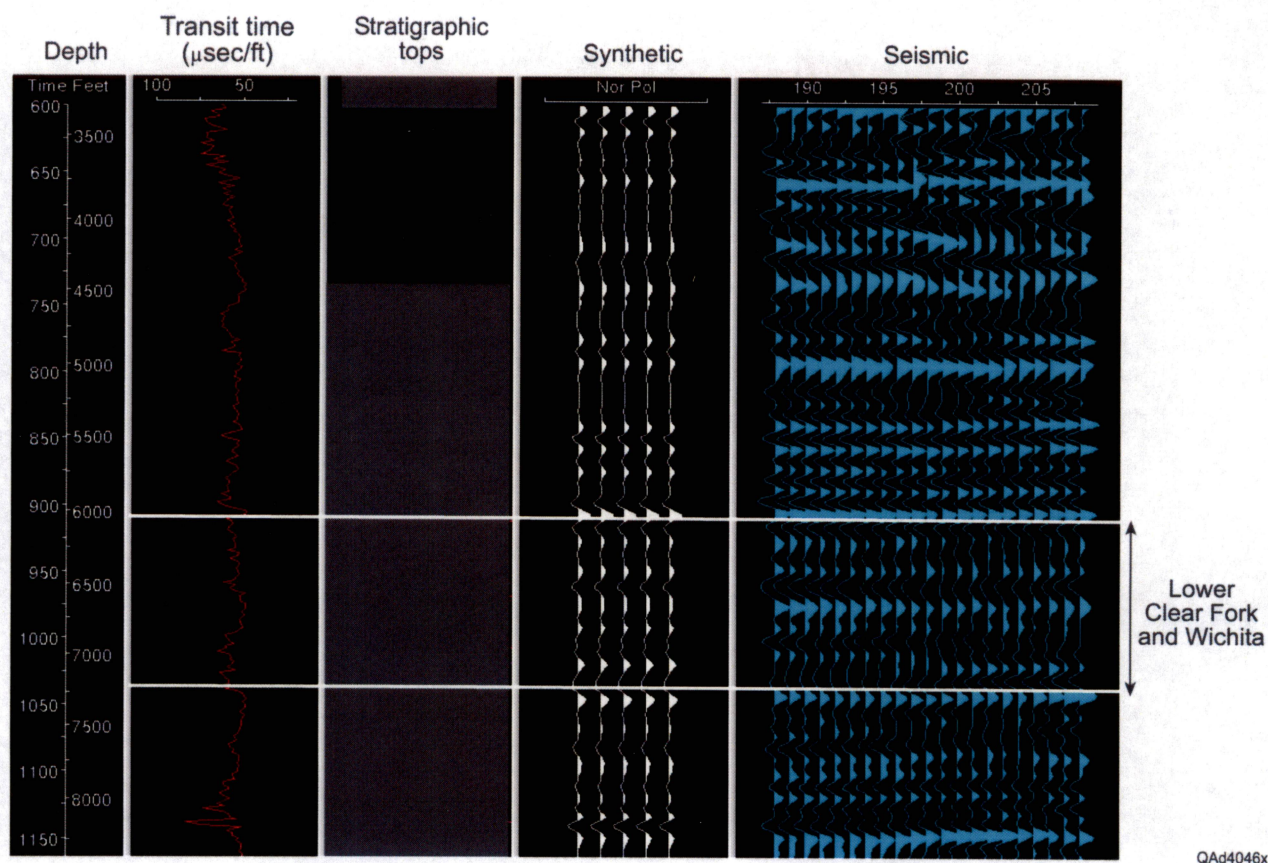


Figure 2. Synthetic seismogram of lower Clear Fork and Wichita and surrounding formation in well Cal/Mon 1 across 2-D seismic line 0123.

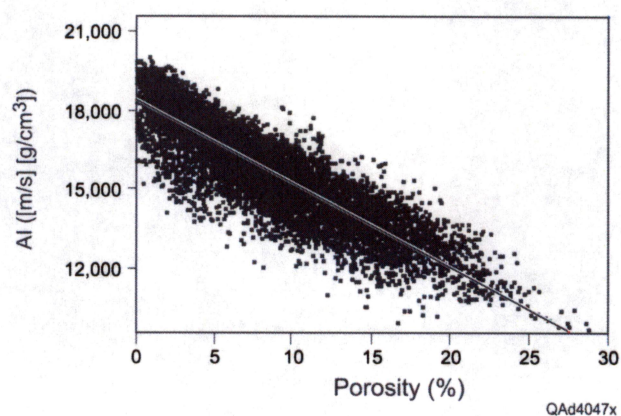


Figure 3. Linear relationship between AI and log porosity of carbonate rocks in the lower Clear Fork and Wichita, Fullerton field, Andrews County, Texas. AI was computed from transit time and bulk density logs in eight wells, whereas porosity was calculated by neutron-density cross-plotting, with a sample rate of 0.5 ft. Correlation coefficient between AI and porosity=0.88.

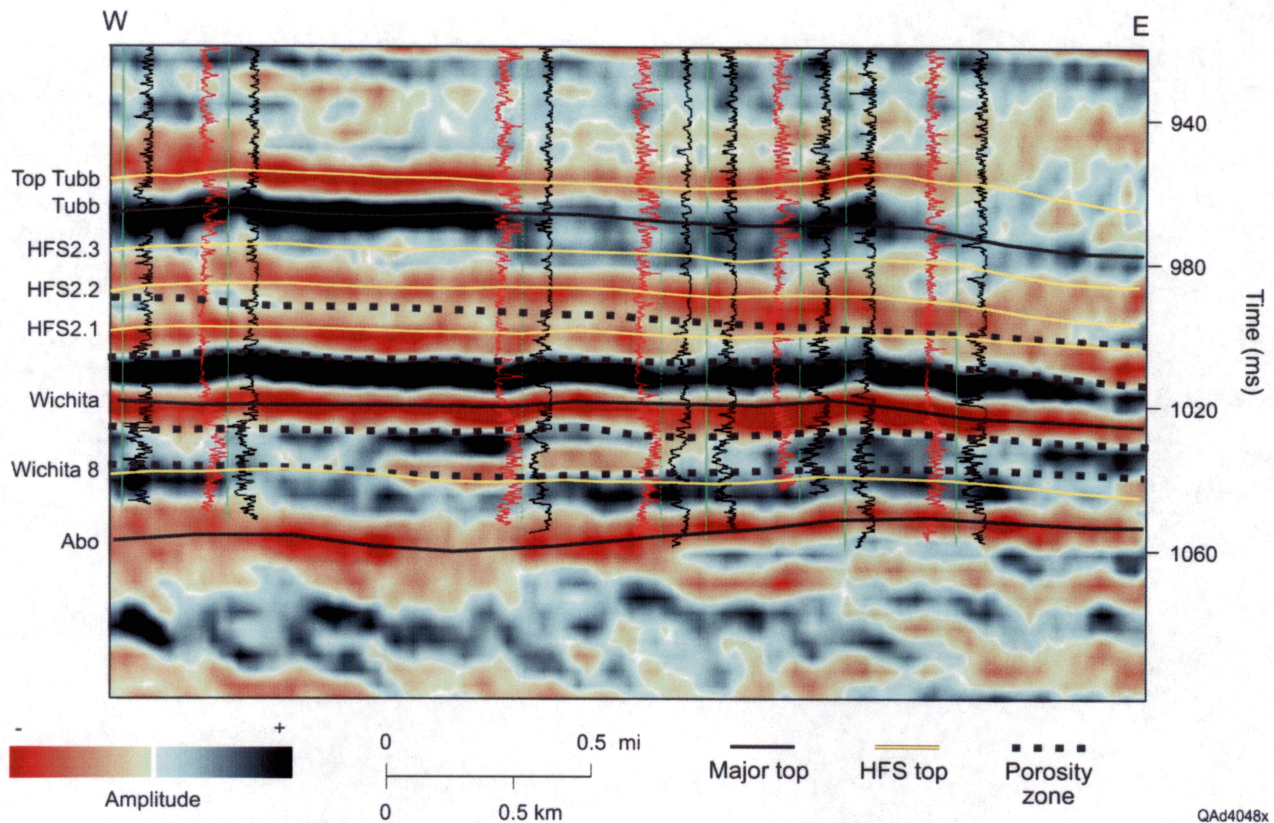


Figure 4. A 0°-phase seismic section (trace 2382) in the 3-D survey area showing poor tie between high-porosity/low-AI units and amplitude/polarity and difficulty in picking high-frequency sequence boundaries. Dashed lines highlight porosity zones in high-frequency sequences and flow units.

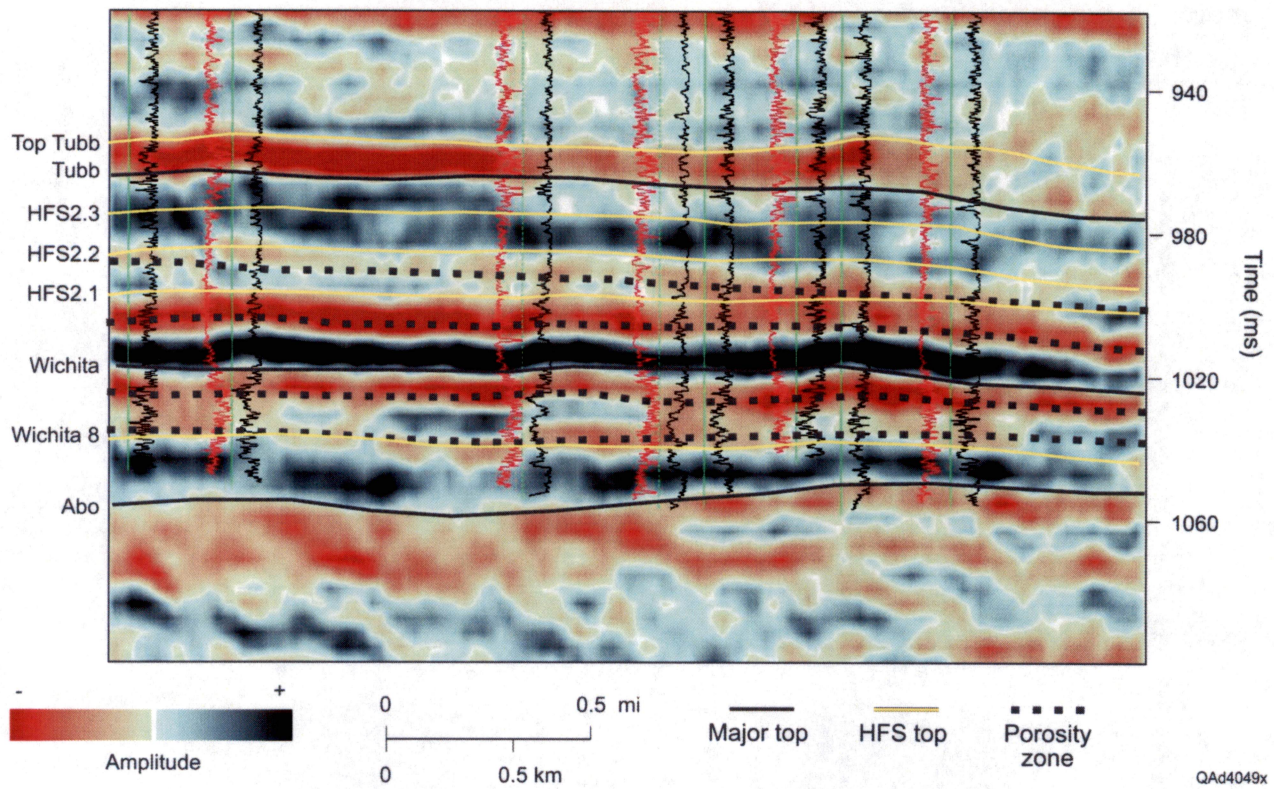


Figure 5. A 90°-phase seismic section (trace 2382) in the 3-D survey area showing improved tie between high-porosity/low-AI units and amplitude/polarity. The picking of high-frequency sequence boundaries, however, is still difficult.

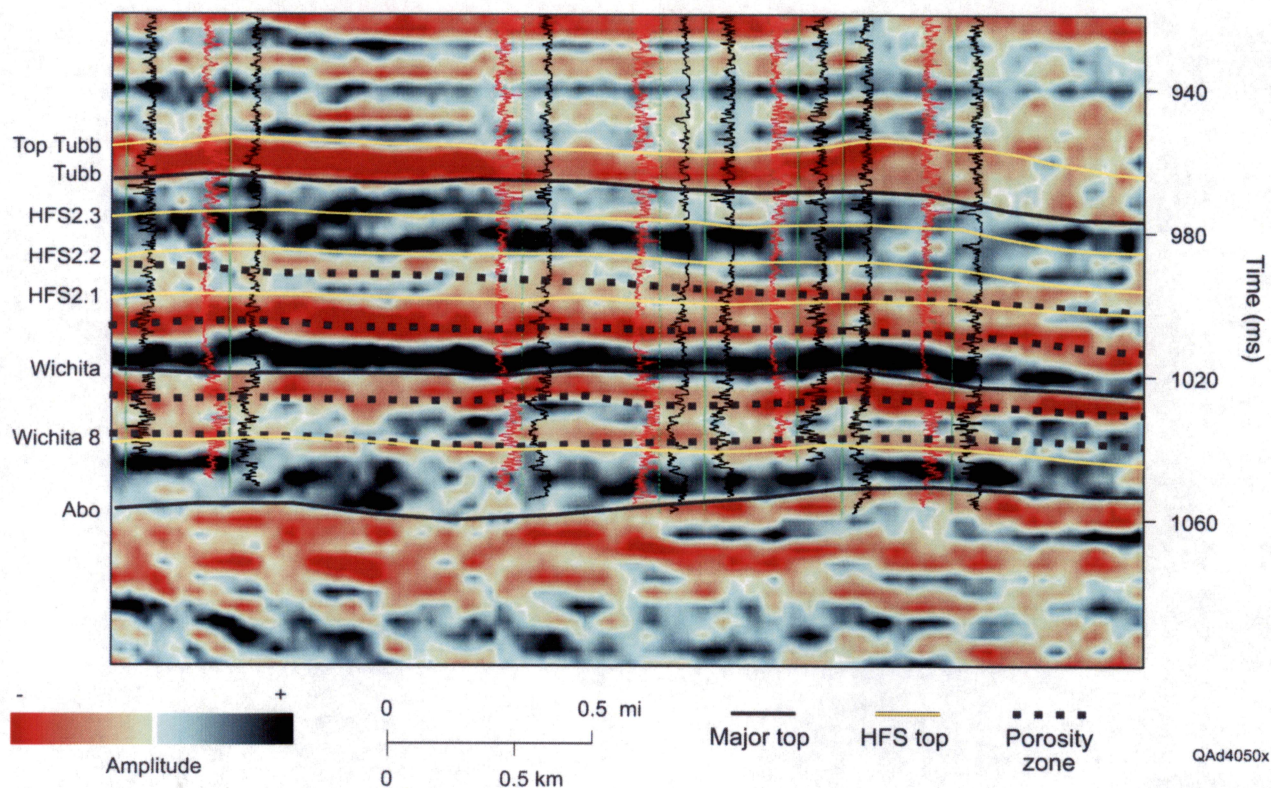


Figure 6. A high-frequency-enhanced (spectral-balanced) version of Figure 5 showing improvement in seismic resolution. Though not accurate, the high-frequency sequence boundaries can be partially interpreted by following top and bottom of the porosity zones.

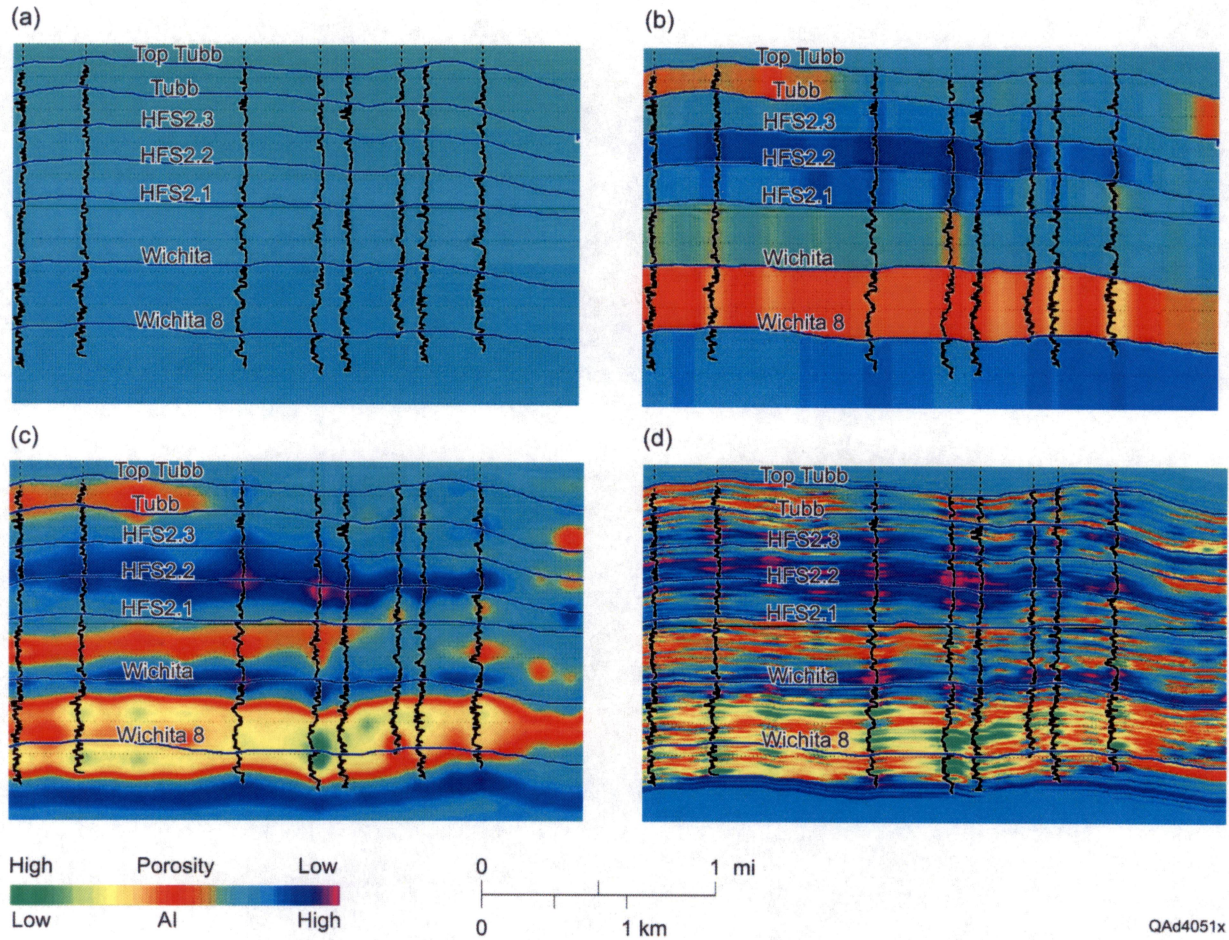


Figure 7. Wireline log-based AI models for reservoir characterization and seismic inversion. A total of seven high-frequency sequence boundaries were used for stratigraphic control of the modeling. (a) Background model. (b) Blocky model. (c) Smoothed log model up to seismic frequency (0-70 Hz). (d) Log model sampled to 0.125 ms (1-1.2 m). Logs are pseudo-AI calculated from porosity. From (a) to (d) the use of geologic information is increased.

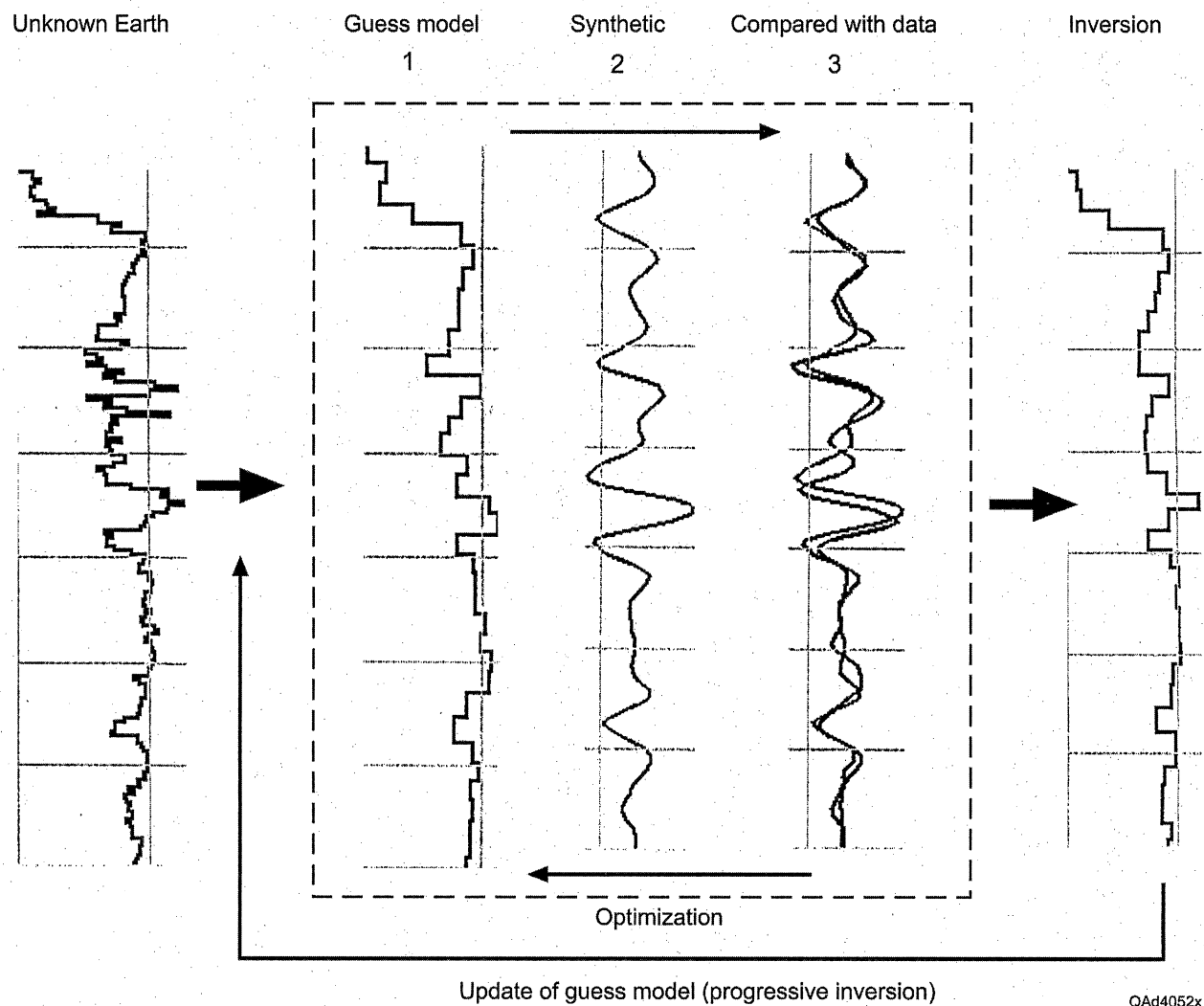


Figure 8. Procedure of a model-based inversion.

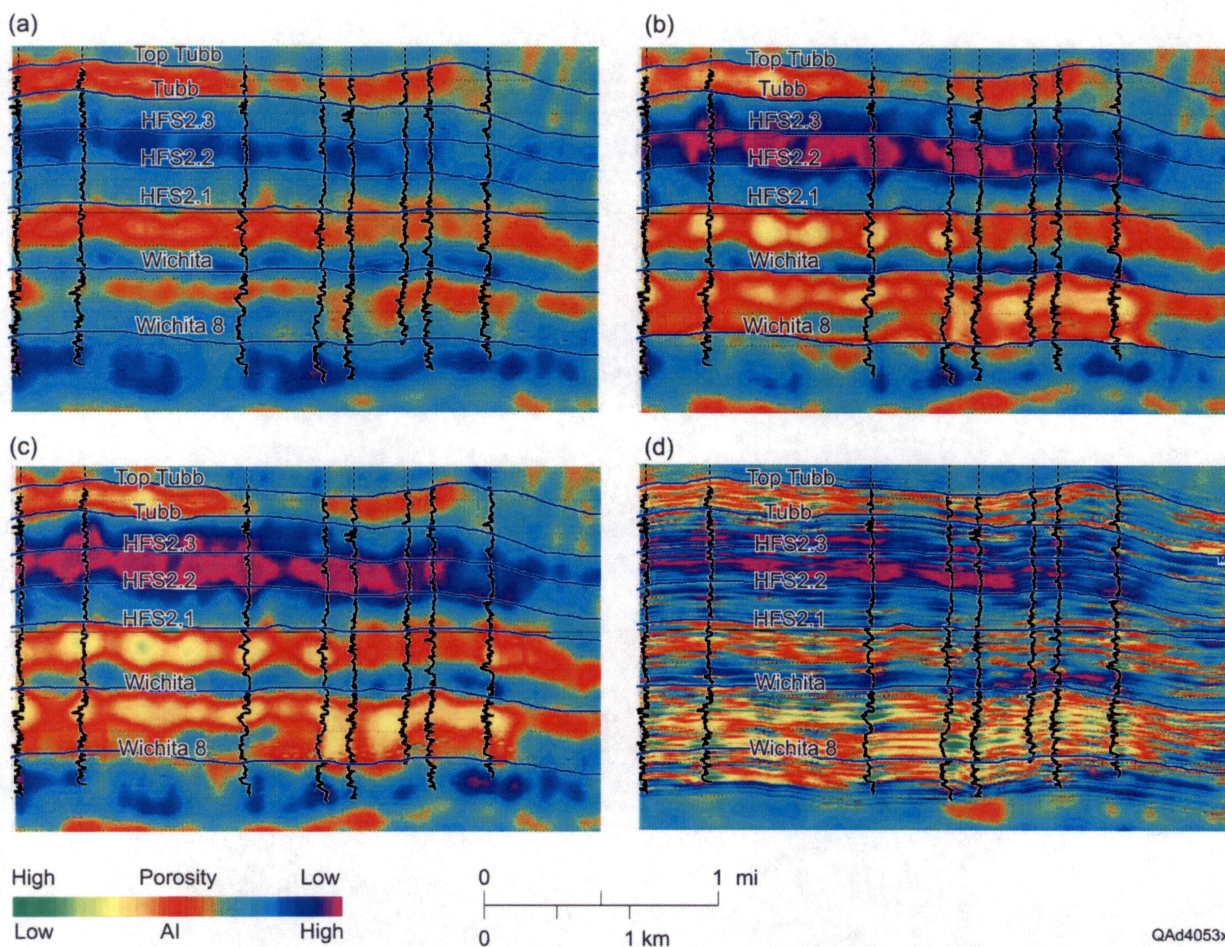


Figure 9. Model based inversion from (a) Background model, (b) Blocky model, (c) Smoothed log model, and (d) Log model in Figure 7. Section follows same seismic line (trace 2382).

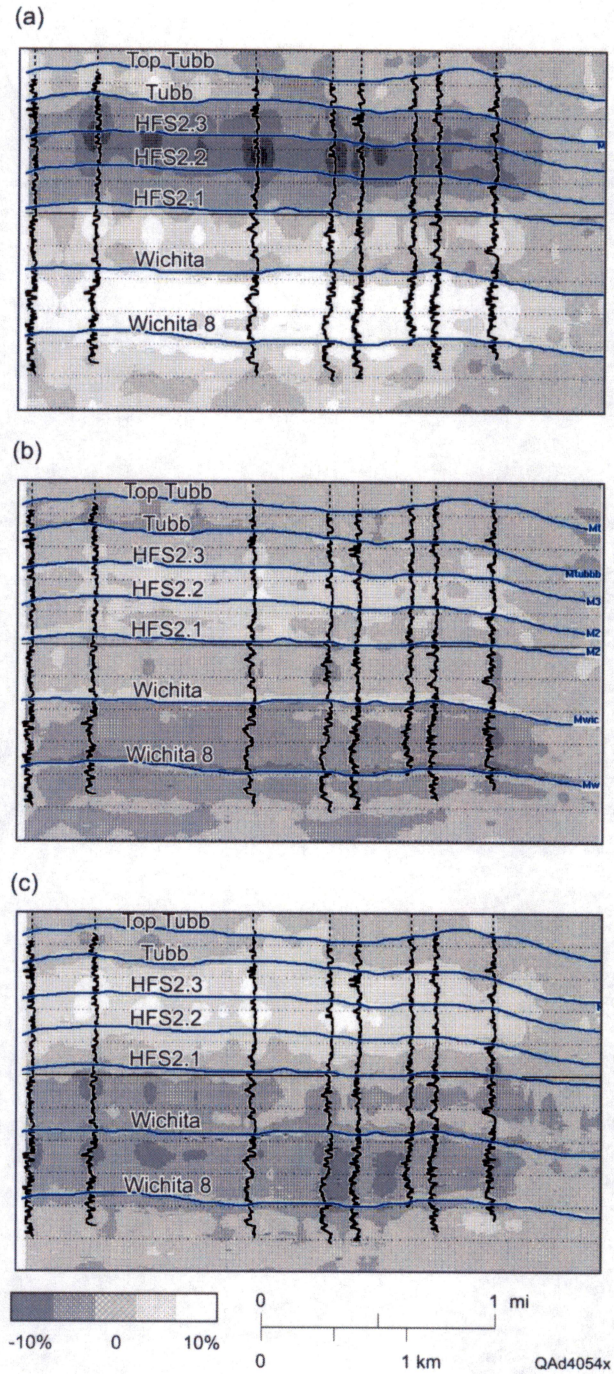


Figure 10. Differences of AI inversion corresponding to different initial model inputs. (a) Difference between the background model inversion (Figure 9a) and the average value of models a, b, and c in Figure 9. (b) Difference between the blocky model inversion (Figure 9b) and the average value of models a, b, and c in Figure 9. (c) Difference between the smoothed model inversion (Figure 9c) and the average value of models a, b, and c in Figure 9.

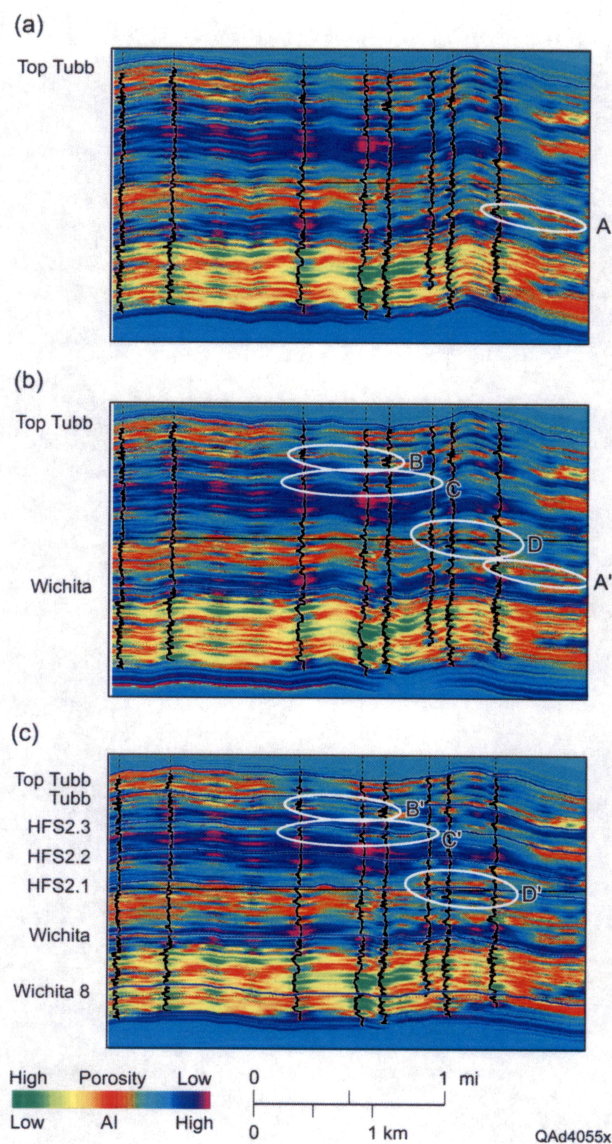


Figure 11. Initial models for progressive inversion. (a) Model based on one horizon. (b) Model from two horizons. (c) Model based on seven horizons. Logs are pseudo-AI calculated from porosity.

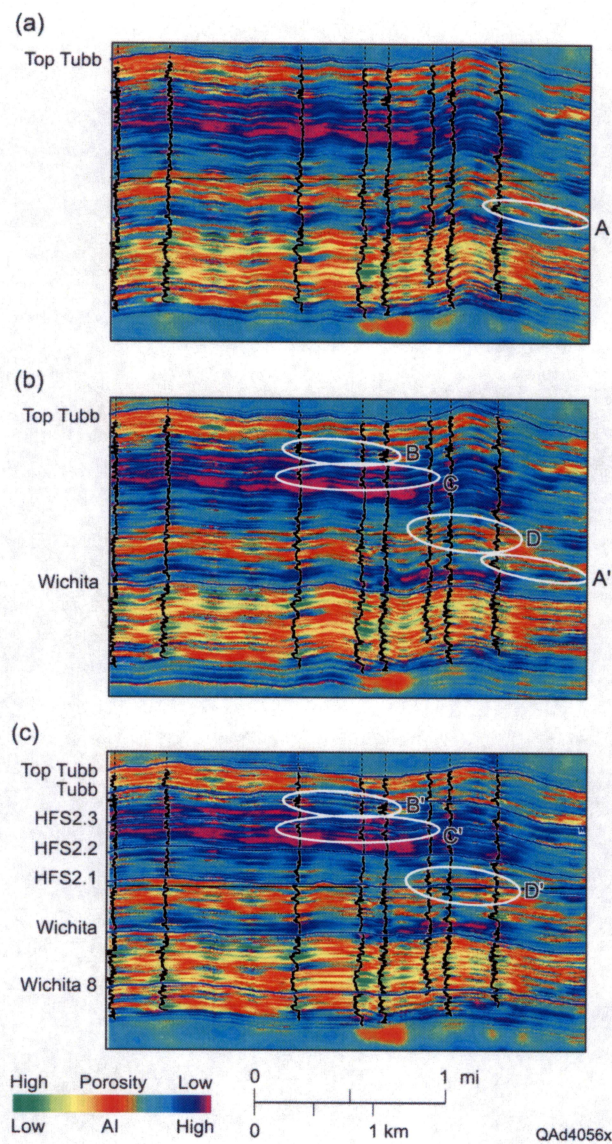


Figure 12. Progressive inversion. (a) Inverted AI based on one-horizon model (Figure 11a). (b) Inverted AI based on two-horizon model (Figure 11b). (c) Inverted AI based on seven-horizon model (Figure 11c).

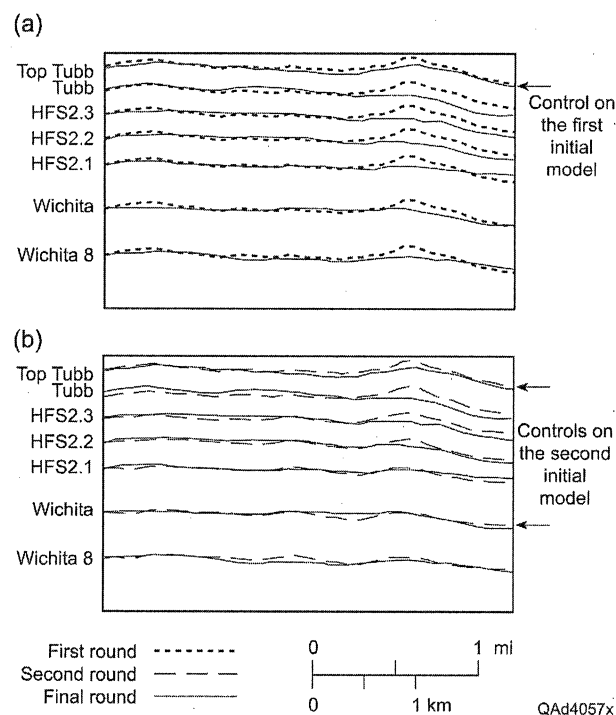


Figure 13. Differences of stratigraphic framework used in initial model construction. (a) One-horizon model (the first round) versus seven-horizon model (the final round). In the one-horizon model, high-frequency sequence boundaries were extrapolated parallel from the single control surface (top Tubb). (b) Two-horizon model (the second round) versus seven-horizon model (the final round). In the two-horizon model, high-frequency sequence boundaries Tubb and HFS2.1-2.3 were linearly interpolated between control surface top Tubb and Wichita. High-frequency sequence boundary Wichita 8 was extrapolated parallel from control surface Wichita.

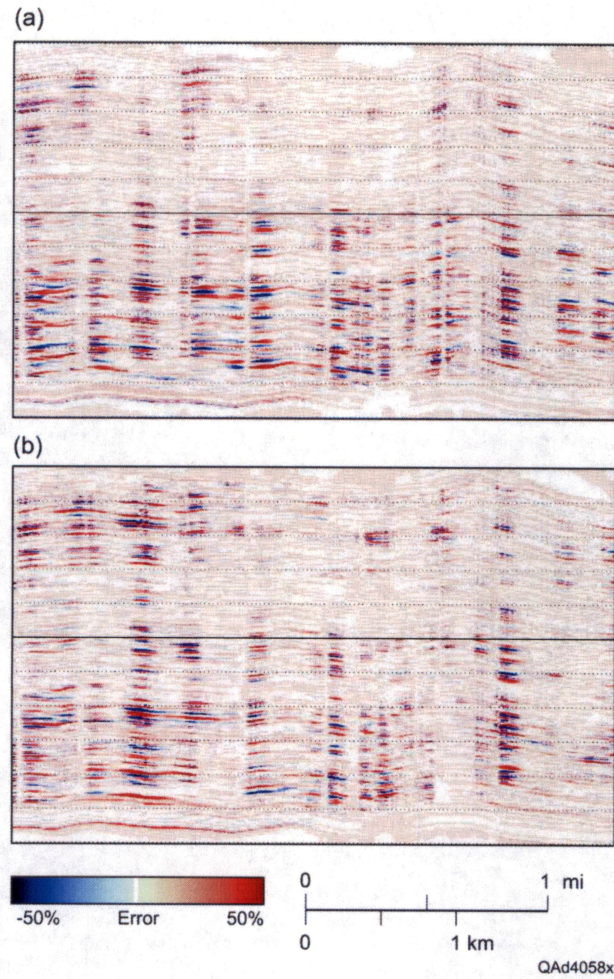


Figure 14. Difference in AI estimation through progressive inversion. (a) Difference between the second-round inversion (Figure 12b) and the first-round inversion (Figure 12a). (b) Difference between the final-round inversion (Figure 12c) and the second-round inversion (Figure 12b).

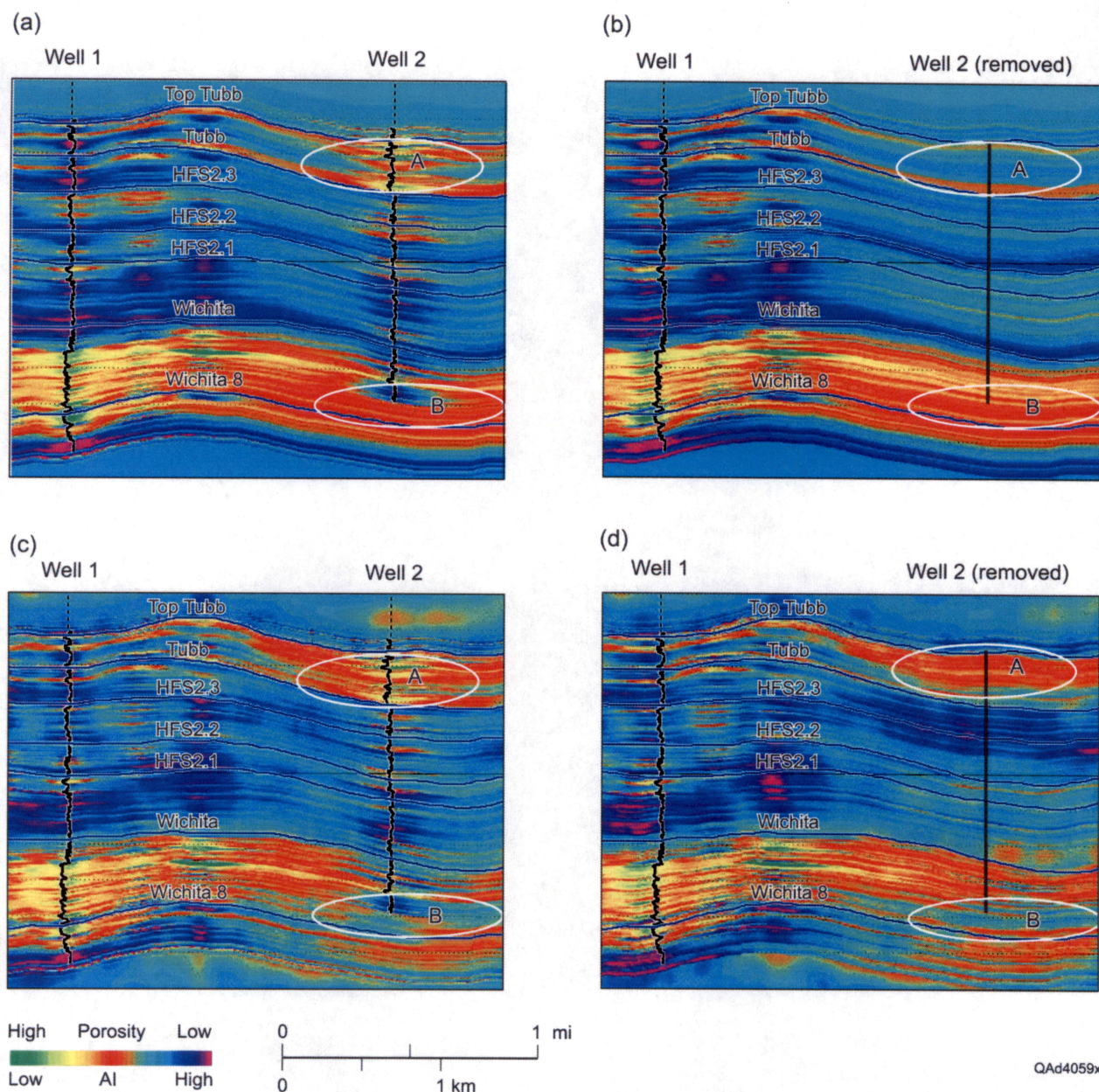


Figure 15. Blind test showing value and limit of progressive inversion (example 1). (a) Initial model. (b) Initial model made after removing a well. A high-porosity zone (A) and a low-porosity zone (B) in the model are misrepresented as a low-porosity zone (A) and a high-porosity zone (B). (c) Inversion from model (a) revealing recovered zone A and zone B. (d) Inversion from model (b) managed to recover zone A and zone B with subtly different details compared to (c).

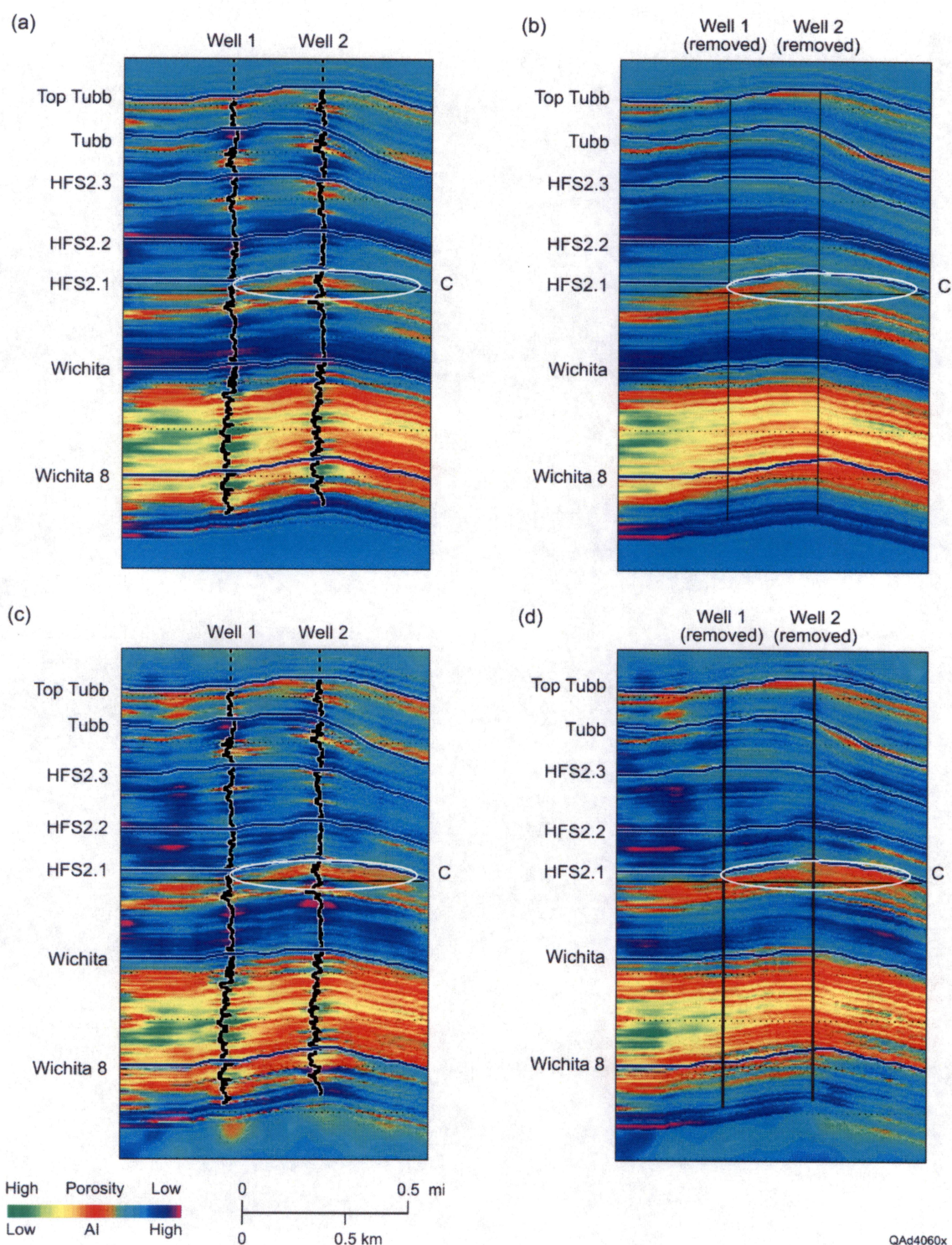


Figure 16. Blind test showing value and limit of progressive inversion (example 2). (a) Initial model. (b) Initial model made after removing two wells. A high-porosity zone C is misrepresented. (c) Inversion from model (a) revealing recovered zone C. (d) Inversion from model (b) attempted to recover zone C with subtly different details compared to (c).

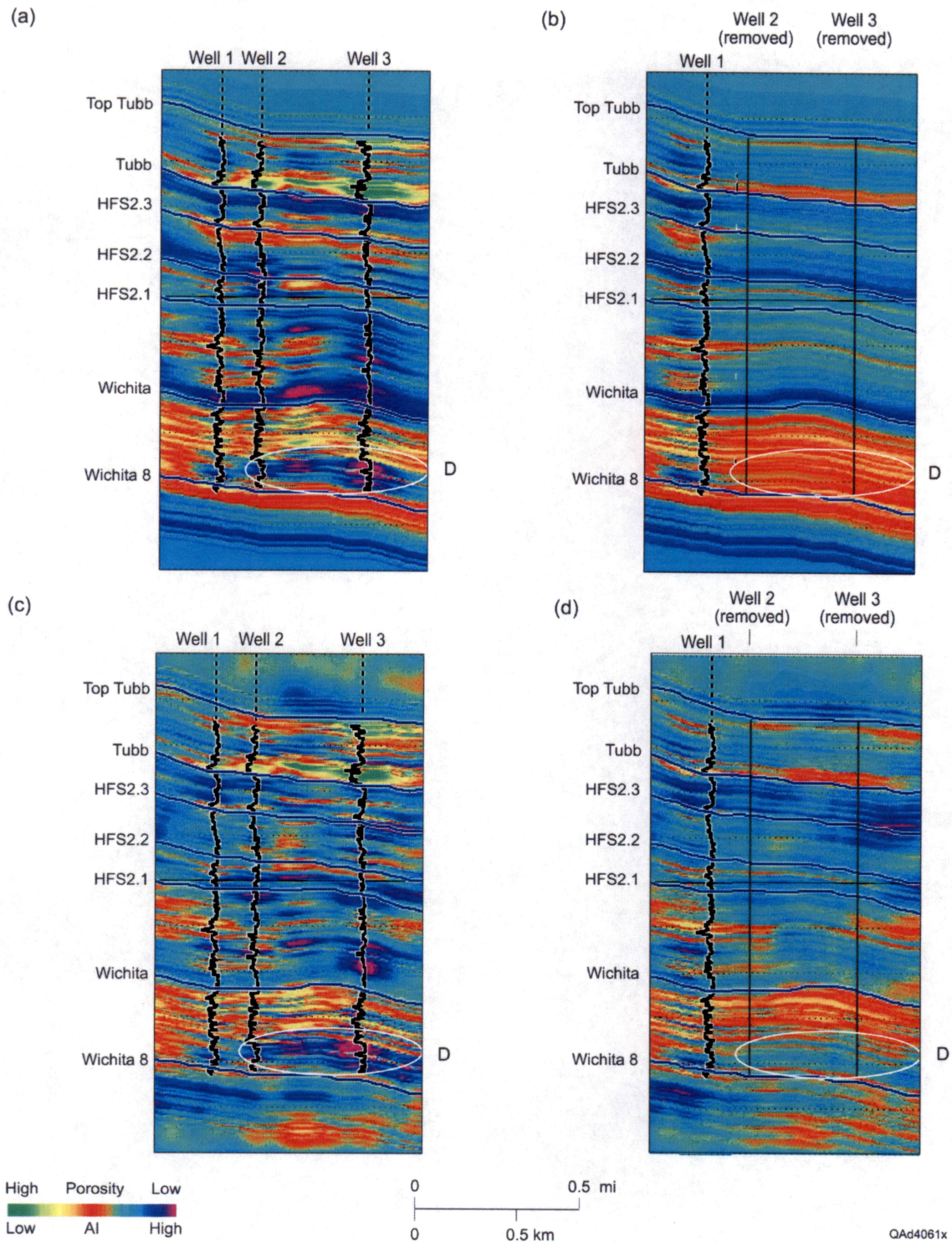


Figure 17. Blind test showing value and limit of progressive inversion (example 3). (a) Initial model. (b) Initial model made after removing two wells. A low porosity zone D is misrepresented. (c) Inversion from model (a) revealing recovered zone D. (d) Inversion from model (b) that recovers zone D with subtly different details compared to (c).